Stability Robustness and Rendering Fidelity Trade-offs of Haptic Interfaces under Admittance Control

by

Ömer Burak Aladağ

Submitted to
the Graduate School of Engineering and Natural Sciences
in partial fulfillment of
the requirements for the degree of
Master of Science

SABANCI UNIVERSITY

December, 2023

Stability Robustness and Rendering Fidelity Trade-offs of
Haptic Interfaces under Admittance Control

Ömer Burak Aladağ

Mechatronics Engineering, M.Sc. Thesis, 2023

Thesis Supervisor: Prof. Volkan Patoglu

Keywords: Physical human-robot interaction, haptic rendering, admittance control, series elastic actuation, coupled stability, passivity, inertia compensation, rendering fidelity, passive physical equivalents, effective impedance

Abstract

Physical human-robot interaction (pHRI) is an emerging field that includes applications in manufacturing, rehabilitation, and AR/VR technologies. The goal of pHRI is to design interfaces with a focus on safety, minimizing the risks of injuries during human-robot interactions, without compromising system performance. However, there is an inherent trade-off between the safety and performance of robots in these applications.

This study explores stability robustness and rendering fidelity trade-offs of haptic interfaces under admittance control. Our analysis is based on series elastic actuation (SEA) under the basic admittance control (BAC) and covers other admittance-controlled kinesthetic haptic interfaces as a special case when the sensor stiffness is set high.

To analyze stability robustness, we derive necessary and sufficient conditions for the passivity of the admittance-controlled SEA while rendering various fundamental components, such as masses, springs, dampers, and their combinations. The performance of these renderings is analyzed by deriving passive physical equivalents of the corresponding closed-loop systems. Passive physical equivalents allow us to examine how different controller structures and plant/controller parameters affect the performance of a closed-loop system. We can also identify parasitic effects, study low/high frequency behaviors, and compare the rendering performance of different closed-loop systems with each other, through passive physical equivalents.

Our results indicate that the stability robustness is increased as the force sensor becomes more compliant. Moreover, utilization of a softer force sensor enables better inertia compensation while rendering a virtual mass, at the expense of a more limited performance bandwidth. Furthermore, a softer force sensor also enables parasitic damping effects to be kept lower while rendering a virtual stiffness, at the expense of lower upper bounds on passively renderable stiffness levels. SEA is better suited for improved inertia compensation and high fidelity rendering of low impedances are required.

We provide a comprehensive set of guidelines for rendering virtual environments with admittance controlled kinesthetic haptic interfaces. First, when a virtual mass is rendered, adding an appropriate amount of virtual damping to the model is recommended, as such damping enlarges passivity bounds. On the other hand, the addition of such damping adversely affects the rendering fidelity. Second, to achieve renderings with low parasitic damping, it is recommended to select a compliant force sensor. However, a compliant force sensor will introduce a limit to the maximum passively achievable stiffness. Thirdly, the admittance controller is suggested for high-impedance virtual environments, such as mass-damping renderings since passivity does not impose an upper bound on these environments, while velocity-sourced impedance control (VSIC) is recommended for low-impedance virtual environments, such as spring or free space renderings. Finally, we show that passive inertia compensation via feedforward controller terms is not possible under realistic bandwidth limitations, while feedforward terms can improve rendering performance at low frequencies.

Our theoretical findings are also experimentally verified; passivity bounds are confirmed through coupled stability experiments with relevant most destabilizing environments while rendering performance is characterized by exciting the closed loop systems with an ideal motion source.

Overall, this study provides a rigorous analysis of stability robustness and rendering fidelity trade-offs involved in kinesthetic haptic interfaces operating under admittance control, including SEA. Moreover, our results have direct consequences for more complex control approaches, such as VSIC, as admittance control constitutes a fundamental component within such architectures. Our guidelines can help the researchers implement passive virtual environment renderings with high fidelity, design more capable haptic interfaces for admittance control, and better understand the limitations of their interaction controllers.

Admitans Kontrolü Altındaki Dokunsal Arayüzlerinin
Kararlılık Gürbüzlüğü ve Görüntüleme Doğruluğu Arasındaki Ödünleşimler

Ömer Burak Aladağ

Mekatronik Mühendisliği, Yüksek Lisans Tezi, 2023

Tez Danışmanı: Prof. Dr. Volkan Patoğlu

Anahtar kelimeler: Fiziksel insan-robot etkileşimi (fİRE), dokunsal algı yaratma, admitans kontrolü, seri elastik eyleme, bağlaşık kararlılık, pasiflik, atalet telafisi, dokunsal algı yaratma performansı, pasif fiziksel gerçekleştirmeler

Özet

Fiziksel insan-robot etkileşimi (fİRE), üretim, robot destekli rehabilitasyon ve artırılmış/sanal gerçeklik uygulamalarında yoğun kullanılan bir teknolojidir. fİRE'nin amacı, sistem performansından taviz vermeden, insan-robot etkileşimleri sırasında güvenli arayüzler tasarlamaktır. Ancak, bu tür uygulamaların güvenliği ile performansı arasında kaçınılmaz bir ödünleşim mevcuttur.

Bu çalışma, admitans kontrolü altındaki dokunsal arayüzlerin kararlılık gürbüzlüğü ve dokunsal algı performansı arasındaki ödünleşmeleri keşfetmeyi amaçlamaktadır. Temel admitans kontrolü (TAC) altında seri elastik eyleme (SEE) temelli analizimiz, admitans kontrolü altındaki diğer kinestetik dokunsal arayüzleri, sensör sertliğinin yüksek olduğu özel bir durum olarak kapsar.

Kararlılık gürbüzlüğünü analiz etmek için, admitans kontrolü altındaki SEE'nin pasif olabilmesi için gerekli ve yeterli koşullar türetilmiştir. Bu sistemlerin performansını analiz etmek içinse, kapalı döngü sistemlere karşılık gelen, kütleler, yaylar, sönümleyiciler ve bunların kombinasyonlarından oluşturan, pasif fiziksel gerçekleşimler türetilmiştir. Pasif fiziksel gerçekleşimler aracılığıyla, farklı kontrolcü yapılarının ve sistem/kontrolcü parametrelerinin kapalı döngü sistemlerin performansına etkileri incelenmiştir. Ayrıca pasif fiziksel gerçekleşimler aracılığıyla, parazitik etkiler tanımlanmış, farklı kapalı döngü sistemlerinin dokunsal algı performansı karşılaştırılmış ve düşük/yüksek frekans davranışları incelenmiştir.

Sonuçlarımız, kuvvet sensörünün esnekliği arttıkça kararlılık gürbüzlüğünün arttığını göstermektedir. Ayrıca, daha yumuşak bir kuvvet sensörünün kullanılması,

sanal bir kütle oluşturulurken daha etkin atalet telafisine imkan vermektedir; ancak bu sonuçlar daha sınırlı bir performans bant genişliğinde geçerlidir. Ayrıca, daha esnek bir kuvvet sensörü, sanal yay oluşturulurken parazitik sönümleme etkilerinin daha düşük tutulmasını sağlar; ancak pasif olarak geri-beslenebilen yay sertliği seviyelerindeki üst sınırı azaltır. Bu nedenle, tasarımı gereği esnek bir kuvvet sensörüne sahip olan SEE, etkin atalet telafisi ve düşük empedansların yüksek kaliteli geri-beslemesi için önerilmektedir.

Admitans kontrollü kinestetik dokunsal arayüzlerle sanal ortamların oluşturulmasına yönelik kapsamlı öneriler sunuyoruz. İlk olarak, sanal kütle oluşturulurken, modelde uygun miktarda sanal sönümlemenin eklenmesini öneriyor ve bu tür bir sönümlemenin modele eklenmesinin pasiflik sınırlarını genişletirken dokunsal algı yaratma performansını olumsuz yönde etkilediğini gösteriyoruz. İkinci olarak, düşük parazitik sönümleme ile gerçekleştirilmiş dokunsal algılar elde etmek için yumuşak bir kuvvet sensörü seçilmesini öneriyoruz. Ancak, yumuşak bir kuvvet sensörünün, maksimum pasif olarak gerçekleştirilebilir sertliğe bir sınırlama getireceğini de not ediyoruz. Üçüncü olarak, pasiflik şartlarını sağlama konusunda daha avantajlı oldukları için kütleme ve sönümleme gibi yüksek empedansa sahip sanal ortamlar için admitans kontrolcüsünün, boşluk ve yay gibi düşük empedanslı sanal ortamlar içinse hız kaynaklı empedans kontrolcüsünün (HKEK) kullanılmasını öneriyoruz. Son olarak, gerçekçi bant genişliği sınırlamaları altında, ileri beslemeli denetleyici terimleri aracılığıyla pasif atalet telafisinin mümkün olmadığını, ancak ileri besleme sayesinde düşük frekanslarda görüntüleme performansının arttırılabileceğini gösteriyoruz.

Teorik bulgularımızı deneysel olarak da test ediyor ve pasiflik sınırlarını en kararsızlaştırıcı ortamlarla bağlaşık kararlılık deneyleri aracılığıyla, dokunsal algı yaratma performansını ise kapalı döngü sistemi karakterize ederek doğruluyoruz.

Bu çalışma kapsamında, admitans kontrolü altında çalışan kinestetik dokunsal arayüzlerde kararlılık gürbüzlüğü ve görüntüleme doğruluğu arasındaki ödünleşimler kapsamlı bir şekilde incelenmiş ve sanal ortamların oluşturulmasına yönelik öneriler sunulmuştur. Admitans kontrolü, HKEK gibi daha karmaşık kontrol mimarilerinin temel bir bileşenini oluşturduğu için, sonuçlarımız bu tür kontrolcüler için de genellenebilir niteliktedir. Bu çalışma kapsamında sunulan öneriler, araştırmacıların, admitans kontrolü altında çalışan daha etkin dokunsal arayüzler tasarlamalarına, pasif sanal ortam görüntülerini yüksek doğrulukla elde etmelerine ve etkileşim kontrolcülerinin kısıtlamalarını daha iyi anlamalarına yardımcı olabilecek niteliktedir.

Acknowledgements

First and foremost, I would like to express my gratitude to my thesis advisor, Prof. Volkan Patoğlu, for his unwavering guidance and support during both my bachelor's and graduate studies. His expertise in the field has not only enriched my academic journey but has also significantly contributed to the completion of this thesis.

Additionally, I am deeply thankful to the members of my thesis jury, Dr. Melih Türkseven and Prof. Çağatay Başdoğan, for generously dedicating their time to serve on my thesis committee and for their invaluable advice and feedback.

I extend my heartfelt appreciation to my beloved family for their endless support throughout my studies, without which I could not have become the person and researcher I am today. I also want to express my profound love for my newborn nephew, Milan.

I am grateful to my colleagues from both the Human-Machine Interaction Laboratory (HMI) and the Mechatronics Laboratory, namely Bilal Çatkın, Celal Umut Kenanoğlu, Çağatay Irmak, Ali Yaşar, Uğur Mengilli, Alperen Kenan, Özgür Taylan Kenanoğlu, Harun Tolasa, İlhami Osman Karakurt, Görkem Gemalmaz, Sıla Akpınar, Cihan Arlı, Mehmet Emin Mumcuoğlu, and Hasan Atacan Tosun for the enjoyable moments shared and the countless coffees together.

I wish to express my gratitude to my high-school friends, Berkant Keser, Berkay Titrek, Emre Yeşilkütük, Hilmi Şamil Özdil, Mert Kozpınar, Ömer Safa Çavuş, Beyza Atasayar, Sara Nil Acarsoy, Ilgın Çetin, Seda Çiçek, and Zeynep Bener, who have been by my side for over a decade.

Furthermore, I am thankful to my close-knit group, Hasan Alp Boz, Emir Alaattin Yılmaz, Muratcan Serdar Canlı, Hamza Kandiş, Berkant Deniz Aktaş, Ahmet Ege Güldalı, Tahsin Alper Özkan, Yağız Varol and Orhun Barış for their unwavering support and guidance whenever needed.

Special thanks go to my friends Ali Enver Bilecen, Yağmur Damla Şentürk, Emre Yavaş, Umut Barut, and Alperen Doğan for the enjoyable gym sessions and for making my university experience truly memorable during my master's degree.

Finally, I extend my appreciation to my travel buddies, Efraim Ölçer, Mustafa Berk Turgut, and Berk Sürücü, even though circumstances prevented us from traveling together for the past three years.

This study was partially supported by TÜBİTAK Grant 22AG003.

Finally, I would like to thank the Scientific and Technological Research Council of Turkey (TÜBITAK) BIDEB 2210-A program for supporting me with the scholarship throughout my studies.

Contents

List of Figures

List of Tables

Chapter 1

Introduction

Physical Human-Robot Interaction (pHRI) stands at the forefront of technological advancement, finding applications in diverse fields such as manufacturing, rehabilitation, and augmented/virtual reality (AR/VR) technologies. The primary objective of pHRI is to develop interfaces that prioritize safety, aiming to minimize the potential risks of injuries during human-robot interactions while maintaining optimal system performance. Yet, a fundamental challenge arises as there exists an inherent trade-off between ensuring the safety of these interactions and optimizing the performance of robots across various applications. Ensuring precise control of impedance at the interaction port is essential for safely engaging with arbitrary environments [1]. Moreover, achieving optimal performance in interaction controllers is constrained by the challenge of achieving coupled stability, as discussed by Newman [2].

Various robotic applications utilize open-loop force control methods. In open-loop force control, the relation between end-effector torques and motor torques is straightforward. The mapping requires that system dynamics are well-designed and known. There are optimization methods to achieve optimal designs with high transparency [3]. Moreover, good mechanical design requires high stiffness, low inertia, and passive back driviability to achieve ultimate performance which brings design challenges to the system.

In contrast, closed-loop force control methods are employed as an alternative to compensate for parasitic effects arising from the system's dynamics. Yet, the inclusion of a force sensor for closed-loop force control introduces stability and performance limitations. To measure interaction forces, the sensor must be placed at the interaction port, resulting in compliance in the link between the end-effector and actuator, leading to non-collocation issues. The non-collocation of the sensor and actuator imposes upper bounds on a closed-loop system's performance, necessitating careful tuning of controllers to have a balance between stability robustness and system performance [2, 4].

Stiff force sensors impose strict upper bounds on controller gains due to non-collocation, limiting the system's ability to respond rapidly and accurately while maintaining robustness. To address this trade-off, an intentional introduction of a compliant element to the end-effector is proposed [5, 6]. Howard initially suggests a method that involves drive compliance, decoupling actuators from the joint and controlling each with separate loops [5]. This concept is later extended and termed Series Elastic Actuation (SEA) by Williamson and Pratt [6].

SEA has been demonstrated to enhance motor performance by safeguarding the motor from parasitic effects, courtesy of the spring's filter-like behavior. Additionally, the compliance of the force sensor relaxes stability bounds, contributing to increased robustness and rendering performance. SEA is a cost-effective alternative to traditional force sensors, requiring the end-effector to be equipped with position encoders to measure deflections. However, it is essential to consider that the spring, acting as a low-pass filter, reduces force control bandwidth. Furthermore, the introduction of SEA adds complexity to the physical system and presents mechanical design challenges.

Various control structures are employed to address the robots engaging in physical interactions with their environments. The concept of impedance control, initially introduced by Hogan [7], emphasizes that controlling force or position alone is insufficient and proposes the control of the relationship between the conjugate variables. The dual of impedance control, commonly known as admittance control,

finds application in manipulators [2, 8]. While impedance control generates forces based on velocity input and desired environmental conditions, admittance control produces desired motion based on measured interaction forces.

Notably, impedance-controlled haptic interfaces excel in rendering low inertia but face challenges when dealing with stiff environments. In contrast, admittance control enables the rendering of high inertia but encounters difficulties in rendering low impedances [9]. This trade-off between impedance and admittance control characteristics is crucial in choosing the appropriate control paradigm for specific applications. Moreover, there exist high-performance haptic devices that leverage the admittance control paradigm, such as the Haptic Master and Cobotic Hand Controller [10, 11].

This study explores stability robustness and rendering fidelity trade-offs of haptic interfaces under admittance control. Our analysis is based on series elastic actuation (SEA) under the basic admittance control (BAC) and covers other admittance-controlled kinesthetic haptic interfaces as a special case when the sensor stiffness is set high.

To assess stability robustness, our analysis focuses on deriving necessary and sufficient conditions for the passivity of the admittance-controlled Series Elastic Actuation (SEA) while rendering of fundamental components—such as masses, springs, dampers, and their combinations—based on [12, 13, 14]. The performance evaluation of these renderings involves creating passive physical equivalents of the corresponding closed-loop systems, as outlined in [15]. These equivalents serve as valuable tools for us to understand the impact of different controller structures and plant/controller parameters on closed-loop system performance.

Through the passive physical equivalents, we gain insights into how various factors influence system behavior. This approach allows us to uncover parasitic effects, explore low-high frequency behaviors, and conduct a comparison of the rendering performance across different closed-loop systems. The performance comparison is further strengthened by employing effective impedance analysis techniques, where

the system dynamics are decomposed into mechanical primitives [16]. This examination provides a comprehensive understanding of between the controller design, system parameters, and the resulting stability and performance characteristics in admittance-controlled SEAs.

We present a comprehensive set of guidelines for effectively rendering virtual environments using kinesthetic haptic interfaces with admittance control. Firstly, we examine different pure virtual environment and compare them with the combinations. Secondly, we analyze how force sensor stiffness affects rendering performance and coupled stability of the system. Thirdly, we discuss advantages of admittance controller over VSIC.

Lastly, we demonstrate that passive inertia compensation through feedforward controller terms is not feasible under realistic bandwidth limitations. However, it is highlighted that feedforward terms can enhance rendering performance, particularly at low frequencies. These guidelines provide a nuanced approach to optimizing the performance of admittance-controlled kinesthetic haptic interfaces in rendering diverse virtual environments.

1.1 Contributions

This thesis systematically analyzes the trade-off between stability robustness and rendering fidelity in haptic interfaces operating under admittance control, with a particular focus on Series Elastic Actuation (SEAs). Additionally, it covers other admittance-controlled devices as a special case, particularly when the sensor stiffness is set to high values.

The analysis of stability robustness involves passivity analysis, establishing the effects of various system and controller parameters on coupled stability. To comprehend the impact of these parameters on performance, we derive passive physical equivalents of closed-loop systems, providing valuable insights into the intricate trade-offs involved. Furthermore, effective impedance analysis is done in order to better understand these insights.

The theoretical findings presented in this study are validated through experimental verification. Passivity bounds are confirmed via coupled stability experiments, exposing the haptic interfaces to the most destabilizing environments. Simultaneously, rendering performance is characterized by subjecting the closed-loop systems to ideal motion sources.

Our contributions can be listed as follows:

- We rigorously study the necessary and sufficient conditions for SEA under basic admittance controller (BAC) during haptic rendering of linear virtual environments, including mass, mass-damping, damping, spring, and Voigt-model rendering.
- We derive passive physical equivalents of closed-loop systems during haptic rendering linear virtual environments and conduct a comprehensive discussion on the performance of each controller. Through the passive physical equivalents, we establish the effects of system and controller parameters on rendering performance.

- We further elaborate on rendering performance through passive physical equivalents by determining the effective impedance of the closed-loop system at low, intermediate, and high frequencies.
- We show that force sensor compliance increases stability robustness while passivity is not affected.
- We prove that a softer force sensor enables a better compensation of the inertia, while virtual mass can rendered at the expense of a limited bandwidth.
- We highlight the inherent challenges in achieving pure spring rendering due to parasitic damping introduced by causality and advocate for the use of the Voigt-model, since it offers a more accurate representation.
- We show that force sensor stiffness adds parasitic damping to pure spring and Voigt-model renderings, while its effects can be compensated by reducing the sensor stiffness at the cost of passively rendering softer environments.
- We reveal that the addition of an appropriate amount of virtual damping to virtual mass rendering enlarges the passivity bounds while simultaneously constraining mass rendering bandwidth.
- We investigate the effects of feedforward controllers on inertia compensation when rendering pure mass with SEA under the BAC. We show that when bandwidth limitations are introduced, inertia compensation is not feasible, while the feedforward control terms may improve rendering performance at low frequencies.
- Compared to VSIC, we recommend the admittance controller for high impedance virtual environments, such as mass-damping renderings, since passivity does not impose upper bounds on passively renderable environments.
- We verify our theoretical findings on passivity bounds and characterize haptic rendering performance through systematic simulations and physical experiments on a single-axis haptic interface driven by SEA.

Our analysis contributes to a thorough understanding of stability robustness-rendering fidelity trade-offs inherent in kinesthetic haptic interfaces operating under admittance control, including SEA. Furthermore, the implications of our results extend to more complex control approaches, such as velocity-sourced impedance control (VSIC), as admittance control constitutes a fundamental component of such controller architectures. The guidelines derived from our study are aimed at assisting researchers in implementing passive virtual environment renderings with high fidelity, designing more capable haptic interfaces for admittance control, and gaining deeper insights into the limitations of their interaction controllers.

1.2 Outline

Chapter 2 provides a comprehensive overview of prior studies in admittance control. It details effective impedance analysis and passive physical equivalents, exploring their impact on system passivity and haptic rendering performance.

Chapter 3 lays down the theoretical foundation crucial to this study, covering passivity theorems and themodel of SEA under BAC. A detailed derivation of the passive physical equivalent of a closed-loop system is demonstrated, along with discussions on effective impedance formulation.

Chapter 4 establishes necessary and sufficient conditions for ensuring passivity in admittance-controlled SEAs when rendering fundamental mechanical components, such as masses, springs, dampers, and their combinations. Derivations of their passive physical equivalents are presented, along with discussions on passivity conditions, feasibility of realizations, and analyses of the effects of system parameters on haptic rendering fidelity.

Chapter 5 expands the discussion on haptic rendering performance by presenting the effective impedance analysis for various controller structures.

Chapter 6 presents experimental validation of the theoretical findings for haptic rendering of SEAs under BAC, specifically when rendering mechanical primitives like masses, springs, dampers, and their combinations.

Chapter 7 explores the effects of feedforward controllers on mass rendering passivity limits of SEAs under BAC.

Chapter 8 summarizes the results and establishes design guidelines in three categories, covering the combination of virtual elements, the compliance of the force sensor, and providing a comparison between impedance and admittance control for haptic rendering.

Chapter 9 concludes the study with a comprehensive summary and discusses future research directions.

Chapter 2

Related Work

2.1 Haptic Rendering with Admittance Control

Newman's discussion of mechanical admittance, focusing on fast motion responses to interaction forces [2], investigates the impact of unmodeled dynamics on passivity. The study introduces the Natural Admittance Control (NAC) design method to address model uncertainty and enhance stability robustness. This innovative approach permits higher controller gains to offset parasitic dynamics, thereby improving overall performance. The approach suggests underestimating the damping and overestimating the inertia to ensure passivity. In addition to this, the paper proposes an innovative approach to instrument the system with a mechanical filter in the form of a parallel spring-damper. As with any causal controller, the effectiveness at low frequencies remains constrained by the physical system's limitations at high frequencies [2, 17].

Addressing performance challenges in industrial applications, Schimmels, and Peshkin discuss issues related to admittance control [18]. They show that contact friction degrades positional accuracy of the manipulator, leading to misalignment in assembly tasks. The examination of NAC passivity is extended in [19], emphasizing the impact of sensor-induced filtering on both passivity. It has been shown that

the mismatch between the dynamics between force and velocity sensor may cause non-passive behavior.

It is asserted that force feedback significantly enhances the force bandwidth of haptic devices [20]. Moreover, closed-loop control on force, as employed in impedance controllers, is found to outperform position-based loops in admittance controllers. As discussed in [9], admittance/impedance controllers outperform each other in various haptic rendering applications in terms of stability robustness. Impedance or admittance type haptic interfaces are known to perform better while rendering virtual environments (VEs) that are close to their plant dynamics. For instance, impedance type devices are generally better at rendering VEs with low impedance levels, while admittance type devices are generally better at rendering VEs with high impedance levels. Admittance-controlled devices are prone to problems where they interact with stiff real surfaces or render VEs with low inertia. Moreover, it is important to note the sensitivity of admittance control to drive-train backlash and internal flexibility in the device. Despite its limitations, various haptic applications continue to leverage the simplicity of the admittance control structure [21, 22, 23].

Recent studies have focused on passivity analysis on the admittance control for physical human-robot interaction (pHRI) [24, 25, 26]. Keemink et al. present a comprehensive analysis of admittance control in interactions with humans, offering guidelines to enhance system performance while maintaining coupled stability [24]. They provide general design guidelines on the effects of feed-forward control, force signal filtering, post-sensor inertia compensation, motion loop bandwidth, and internal robot flexibility. Additionally, Horibe et al. merge the admittance control structure with Series Elastic Actuation (SEA), exploring trade-offs between the controller and compliance while accounting for excess passivity arising from human biomechanics [26]. They show that SEA allows for much “free-er” space than typical admittance-type devices, but this behavior comes at the expense of less stiff VEs.

Mechanical primitives such as mass, spring, and dampers are fundamental components to construct virtual environments under haptic rendering. Mass and dampings are considered to be high-impedance environments while springs and free spaces are referred as low-impedance environments. Admittance control is preferred for rendering high impedances while impedance control is preferred when low impedances are desired [27] [28]. Low impedance requires high admittance gains in the controller which can lead to instability in admittance control. Similarly, high impedance rendering is achieved through higher impedance gain in the implementation where a similar stability problem arises. Moreover, control strategy is also determined to ensure the causality of implementations. Casual mass rendering requires filters to be introduced to ensure causality under impedance control, while spring rendering necessitates such filters under admittance control.

Keemink et al. studied the rendering of all the pure element renderings and their combinations in [24]. They concluded that the addition of virtual damping improves mass rendering which allows for integral motion gain to be employed and enables rendering lower inertias. However, in this work, spring rendering is implemented in a non-causal fashion, making the validity of the results questionable. Moreover, while they analyze the effects of feedforward terms on inertia compensation under admittance control, their analysis does not include the compliance of the force sensor and their results cannot be generalized to devices with compliant force sensors. Another study [25], presents spring rendering under admittance control with SEA and compares it with other existing force controller structures in terms of passivity. They conclude that acceleration feedback in such structures improves both stability and accuracy. One issue is that their controllers are not causal and which are not feasible in real-time applications. While their main focus is impedance control, in this thesis we extend their analysis on admittance control to different virtual environments.

Rendering masses lower than end-effector mass is not possible passively and causes stability issues under admittance control as discussed in [2]. This issue was further studied and limitations on inertia compensation of end-effector established as [1, 2, 17]. The challenge is inherited due to non-collocation as presented in [29].

However, SEA allows one to model the system without the end-effector inertia. Hence, within the limitations as given these studies, it can increase the passively renderable region of pure mass rendering.

On the other hand, free space and spring rendering under impedance control structure (VSIC) with both SEA and SDEA are extensively studied [30, 31, 32]. Necessary and sufficient conditions for pure spring rendering and free space rendering are established in [30]. This study is further extended by addition for physical damping to SEA and converting it to SDEA for same virtual environments [32]. Moreover, it includes combination of virtual damping and virtual stiffness namely Voigt-model. The effects of low-pass filtering on rendering performance and passivity of pure springs and free-space is presented in [31] as an extension to these studies. The influence of filters is intrinsic in implementations due to their presence in sensors and actuators, despite not being explicitly modeled in the environment. In [31], Kenanoglu et. al systematically addresses the effects of filters on these aspects.

Admittance control implementation is a special case of VSIC when the desired virtual environment is set to be the free space. Hence, results in the literature for free space renderings with VSIC under SEA apply to admittance-controlled devices with SEA.

2.2 Performance of Haptic Rendering

To evaluate the performance of closed-loop systems, we use two different methods: passive physical equivalents and effective impedances.

2.2.1 Passive Physical Equivalents

Colgate and Hogan highlight the importance of passive physical equivalents analysis in clarifying the instabilities and limitations inherent in force-controlled robots during interactions with the environment [15]. They present the fundamental

constraints faced by robots employing force feedback controllers, particularly in scenarios involving non-colocated sensors and actuators. Various studies have employed passive physical equivalents within diverse haptic rendering structures to examine the system's behavior under distinct controller configurations [31, 32].

In the mechanical domain, each component finds a counterpart in the electrical domain, facilitating analysis through a force-current analogy wherein force corresponds to current, and velocities correspond to voltages. Similar to the approach in [32], this thesis emphasizes fundamental passive mechanical elements like springs, dampers, and inerters [33] for constructing realizations. The incorporation of the inerter term in the mechanical domain addresses the absence of a storage element in the force-current analogy [34]. This methodology not only allows for the representation of controlled systems through a simplified depiction of inerters, springs, and dampers but also facilitates the derivation of minimal realizations of transfer functions for mechanical systems using network synthesis methods [35, 36].

2.2.2 Effective Impedances

Coupled stability is crucial for ensuring safe interactions with humans, but it also imposes limitations on system performance. Nevertheless, achieving optimal performance in physical human-robot interaction (pHRI) applications is essential to provide a natural user experience. In the study by [16], they distinguish the rendered dynamics as a force-velocity relationship, referred to as mechanical impedance. Furthermore, their characterization decomposes the system into mechanical primitives such as inertia, damping, and springs, named as characterized dynamics. The perceived dynamics are ultimately determined through psychophysical experiments involving humans, considering not only interaction forces but also visual cues and physical experiences with the haptic display.

Similar to Bode and Nyquist analysis, we employ the effective impedance method presented in [16] to break down system dynamics into mechanical primitives across

different frequencies. Therefore, it is crucial to illustrate what is happening at the end-effector, in addition to understanding the rendered dynamics.

It is noteworthy that effective impedances enhance our analysis through passive physical equivalents by providing numerical results, wherein each system/-controller parameter influences the characterized dynamics across the frequency spectrum.

Chapter 3

Preliminaries

This section concentrates on the theoretical background necessary for comprehending the analysis presented in this thesis.

3.1 Passivity of an LTI System

Colgate claims an LTI n-port system is stable when it is coupled to any arbitrary passive environment if the system's driving point impedance of a passive system [12]. In this study, we are interested in 1-port systems and according to Colgate and Hogan, the passivity of a 1-port LTI system is defined as in Theorem 3.1.

Theorem 3.1 ([12, 13, 14]). *A one-port LTI system, which has a rational impedance transfer function $Z(s)$ with real coefficients, is passive if and only if the following conditions are satisfied,*

1. *Z(s) has no poles in the right half plane, and*
2. *$Re\{Z(jw)\} \geq 0$ for all $w \in (-\infty, \infty)$, and*
3. *Any poles of Z(s) on the imaginary axis are simple with positive and real residues.*

Moreover, we present the following Lemmas 3.2-3.5 to utilize them to derive necessary and sufficient conditions from the impedance transfer functions.

Lemma 3.2. *A fourth-degree characteristic polynomial of a system is defined as* $p(s) = \sum_{n=0}^{4} a_n s^n$. *Then, the system is stable if* $\xi := a_1 a_2 a_3 - a_0 a_3^2 - a_4 a_1^2 > 0$ *[30].*

Lemma 3.3. *A third-degree characteristic polynomial of a system is defined as* $p(s) = \sum_{n=0}^{3} a_n s^n$. *Then,* $p(s)$ *has no roots in the close right half plane iff* $a_3 \geq 0, a_2 \geq 0, a_0 \geq 0$ *and* $a_1 a_2 - a_0 a_3 \geq 0$. *If these inequalities are strictly greater than zero, the system will not have any imaginary poles.*

Lemma 3.4. *A transfer function* $H(s) = \frac{num(s)}{den(s)}$ *has positive real parts for all* $\omega \in (-\infty, \infty)$, *where* $s = j\omega$, *if and only if test polynomial* $R(jw) = Re\{num(j\omega) * den(-j\omega)\} \geq 0$

Lemma 3.5. *A quadratic polynomial defined as* $p(x) = \sum_{n=0}^{2} a_n x^n$, $p(x) \geq 0$ *for all* $x \geq 0$ *if and only if* $a_2 \geq 0$, $a_0 \geq 0$, $a_1 \geq -2\sqrt{a_0 a_2}$.

3.2 Description of an LTI Model of SEA

Fig. 3.1 shows an uncontrolled SEA plant model. The system's reflected inertia and damping are denoted as J_m and B_m, respectively. The end-effector and actuator side are decoupled with a compliant element, SEA, where the stiffness of the element is denoted by K_f. We assume that Hooke's Law applies to the compliant element and enables us to measure interaction torques at the end-effector simply by measuring the deflection between the actuator and the end-effector. In addition to these, Z_{end} models the impedance at the end-effector when it is coupled to any environment. As a final note, torques of the actuator and applied torques to the system by a human user are denoted as τ_m and τ_{end}, respectively. We assume humans do not deliberately try to destabilize or harm the system during physical interactions.

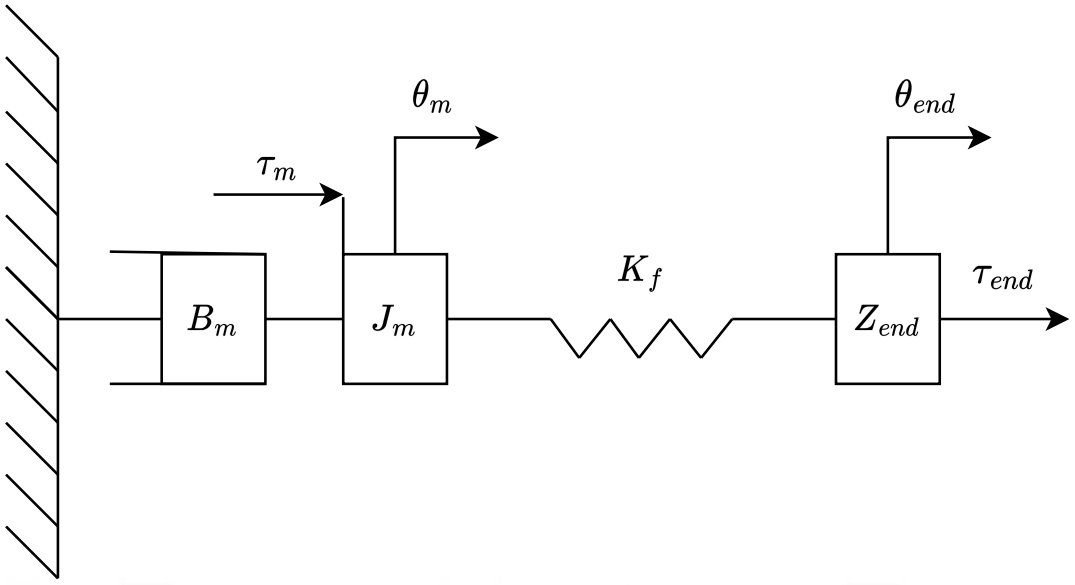

FIGURE 3.1: SEA Plant Model

The block diagram of a close-loop controlled plant is given in Fig. 3.2 where thick lines in the diagram denote physical signals. A_d and C_m are desired admittance of the virtual environment and inner motion controller, respectively. ω_r is the reference trajectory given to the system. However, for simplicity, it is taken as $\omega_r = 0$ in our analysis. Similarly, ω_m and ω_{end} represent motor and end-effector velocities, respectively. Since, Hooke's Law applicable interaction forces can be calculated as $\tau_{sea} = K_f\,(\theta_m - \theta_{end})$. Moreover, $\tau_{sea} = \tau_{h^*} + \tau_h$ where τ_{h^*} represents active component and τ_h represents the passive component applied by human user. Active components are assumed to be independent of the system states. And, we define the driving point impedance transfer function as $Z_{out} = -\frac{\tau_{sea}}{\omega_{end}}$.

Finally, we list a set of assumptions to simplify our analysis:

- We are interested in the LTI model of the SEA plant under BAC. Hence, we ignore non-linear effects such as stiction, friction, backlash, and motor saturation.
- Position/Velocity measurements of the actuator and the end-effector are available with insignificant time delay.
- Electrical dynamics of the actuator are neglected.

- All plant parameters are taken to be positive.

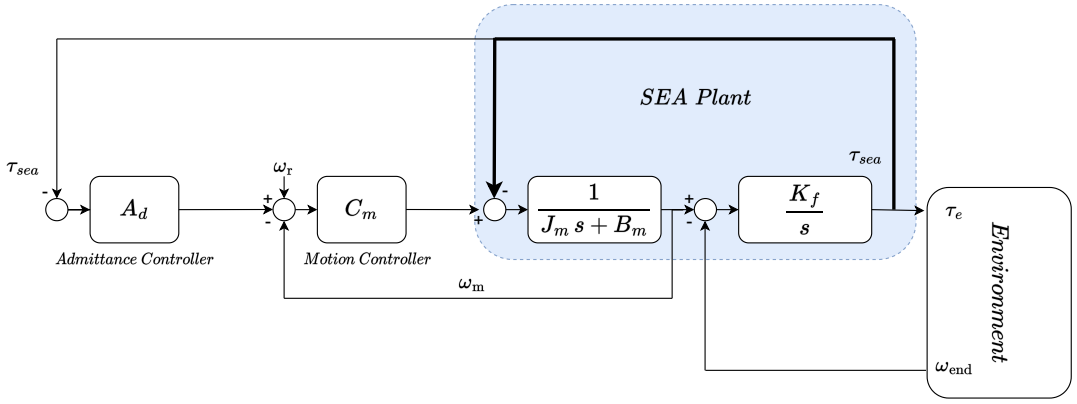

FIGURE 3.2: Block Diagram of SEA under BAC

3.3 Passive Physical Equivalents

3.3.1 Pure Mass Rendering with P Motion Controller with SEA under BAC

In this part, we present necessary and sufficient conditions of Pure Mass Rendering with P Motion controller with SEA under BAC defined in Eqn. (4.2) where motion controller is set to G_m and desired admittance given as $A_d = \frac{1}{M_{ref}\,s}$. We decompose to system into mechanical primitives to establish a example of constructing passive physical equivalents.

$$Z^P_{mass}(s) = \frac{J_m\,K_f\,M_{ref}\,s^2 + \alpha\,K_f\,M_{ref}\,s}{J_m\,M_{ref}\,s^3 + \alpha\,M_{ref}\,s^2 + K_f\,M_{ref}\,s + G_m\,K_f}. \tag{3.1}$$

where $\alpha = B_m + G_m$. According to Theorem 3.1, Eqn. (3.2) constitutes the necessary and sufficient condition for passivity for the system defined in Eqn. (4.2).

$$\frac{G_m\,J_m}{\alpha} \leq M_{ref} \tag{3.2}$$

Similarly, rendered dynamics at the end-effector can be expressed as low-frequency behavior of the system as $M_{vir} \coloneqq \frac{M_{ref}\,\alpha}{G_m}$. Further more, Eqn. (3.2) presents a lower bound on rendered inertia as it is written below:

$$J_m \leq M_{vir} \tag{3.3}$$

3.3.1.1 Derivation of Passive Physical Equivalent of Pure Mass Rendering

In this part, we explicitly show each step to achieve realization of Pure Mass Rendering.

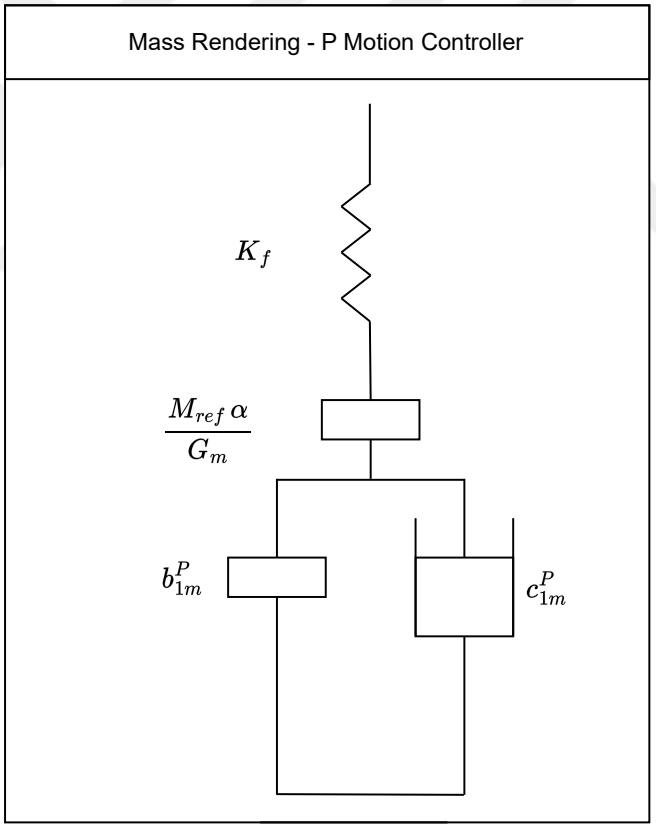

FIGURE 3.3: Passive Physical Equivalent for Mass Rendering with P Motion Controller with SEA under BAC

First, we extract low-frequency and high-frequency behavior of the system as denoted M_{vir} and K_f respectively.

$$Z^P_{mass}(s) = \frac{J_m\, K_f\, M_{ref}\, s^2 + \alpha\, K_f\, M_{ref}\, s}{J_m\, M_{ref}\, s^3 + \alpha\, M_{ref}\, s^2 + K_f\, M_{ref}\, s + G_m\, K_f}. \tag{3.4}$$

$$Z_1 = ((Z^P_{mass})^{-1} - (M_{vir}\, s)^{-1})^{-1} = \frac{J_m\, K_f\, M_{ref}\, \alpha\, s + K_f\, M_{ref}\, \alpha^2}{J_m\, M_{ref}\, \alpha\, s^2 + M_{ref}\, \alpha^2\, s + K_f\, (M_{ref}\, \alpha - G_m\, J_m)} \tag{3.5}$$

Eqn. (3.5) shows the intermediate step when the low-frequency behavior is extracted from the system as their reciprocal are taken, they will appear as series in the realization with K_f.

$$Z_2 = ((Z_1)^{-1} - (\frac{K_f}{s})^{-1})^{-1} = \frac{J_m\, M_{ref}\, \alpha\, s + M_{ref}\, \alpha^2}{M_{ref}\, \alpha - G_m\, J_m} \tag{3.6}$$

Moreover, Eqn. (3.6) shows the resulting impedance after physical filter is extracted. Notice that, remaining impedance transfer function has the same structure as parallel mass-damping pair as shown in (3.7).

$$Z_2 = \frac{J_m\, M_{ref}\, \alpha}{M_{ref}\, \alpha - G_m\, J_m\, \alpha}\, s + \frac{M_{ref}\, \alpha^2}{M_{ref}\, \alpha - G_m\, J_m} \tag{3.7}$$

Eqn. (3.7) cannot be further decomposed in terms of mechanical primitives. Thus, passive physical equivalent analysis is done at this step and depicted in Fig. 3.3. Final components are given in Eqn (3.8)-(3.9).

$$b^P_{1m}(s) = \frac{J_m\, M_{ref}\, \alpha}{M_{ref}\, \alpha - G_m\, J_m\, \alpha}\, s \tag{3.8}$$

$$c^P_{1m}(s) = \frac{M_{ref}\, \alpha^2}{M_{ref}\, \alpha - G_m\, J_m} \tag{3.9}$$

3.4 Effective Impedance Analysis

Colonnese *et al.* presented the method to analyze the performance of haptic displays by deconstructing the closed-loop impedances into effective impedances [16]. The decomposition enables us to evaluate the performance of our system in the frequency domain similar to Bode and Nyquist plots but in terms of mechanical primitives such as mass, spring, and damper. For derived output impedance function, $Z_{out}(s)$, effective impedances are defined as follows:

$$\text{Eff. Integral FB} : \text{EIF}(\omega) = \omega^2 \text{Re}^-\{Z(j\omega)\} \quad -270^\circ \leq \theta \leq -90^\circ$$

$$\text{Eff. Stiffness} : \text{ES}(\omega) = \omega \text{Im}^-\{Z(j\omega)\} \quad -180^\circ \leq \theta \leq 0^\circ$$

$$\text{Eff. Damping} : \text{ED}(\omega) = \text{Re}^+\{Z(j\omega)\} \quad -90^\circ \leq \theta \leq 90^\circ$$

$$\text{Eff. Mass} : \text{EM}(\omega) = \omega^{-1} \text{Im}^+\{Z(j\omega)\} \quad 0^\circ \leq \theta \leq 180^\circ$$

$$\text{Eff. Jerk FB} : \text{EJF}(\omega) = \omega^{-2} \text{Re}^-\{Z(j\omega)\} \quad 90^\circ \leq \theta \leq 270^\circ$$

In our analysis, we are only interested in effective mass, damping and stiffness. Effective Jerk and Integral FB (feedback) are not considered. Moreover, our findings on the performance of the controller through passive physical equivalents are strengthened by this analysis as presented in Section 5.

3.5 Stability of Inner Motion Control Loop

The stability of inner motion loop is important to have robust experience while rendering virtual environments. Thus, we discuss motion control affects on the stability of inner loop.

Remark 3.6. The closed-loop motion control system, depicted in Figure 3.4, is characterized by the following transfer function:

$$H(s) = \frac{\omega_m}{\omega_r} = \frac{G_m\, s + I_m}{J_m\, s^2 + (B_m + G_m)\; s + I_m} \tag{3.10}$$

From Eqn. (3.10), the stability of the inner motion loop is contingent upon two conditions: $I_m \geq 0$ and $B_m + G_m \geq 0$. However, it does not restrict the value of G_m. Notably, selecting a negative value for G_m places the system's zero in the right-half plane (RHP), thus categorizing the system as a non-minimum phase, as per the established definition. In this scenario, the motor exhibits motion in the opposite direction for a finite duration before eventually tracking the reference input. This behavior is suboptimal from a performance standpoint. As a result, to ensure desirable system performance, we impose the constraint that $G_m \geq 0$.

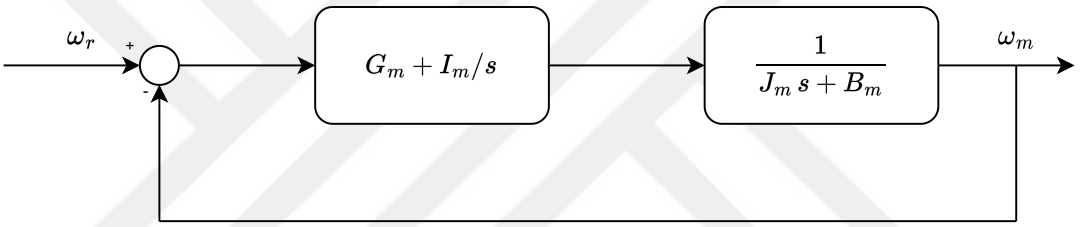

FIGURE 3.4: Closed loop motion (PI) controlled system

Chapter 4

Passivity Analysis and Physical Equivalents of SEA under BAC

In our analysis, output impedance seen from the environment port is defined as $Z_{out}(s) = \frac{-\tau_{sea}}{\omega_{end}} = \frac{-\tau_{sea}}{s\theta_{end}}$. For all of our analysis, all physical system parameters are taken to be positive.

TABLE 4.1: System Parameters for Simulations

Parameters	**Value**	**Unit**
J_m	5.21 x 10^{-4}	kg·m^2
B_m	1.11 x 10^{-2}	N·m·s/rad
K_f	252	N·m/rad
Gear Ratio	1:38	
G_m	0.0576	N·m·s/rad
I_m	1	N·m/rad

4.1 Pure Mass Rendering

The admittance controller allows us to render pure mass without requiring any acceleration signal. Impedance transfer function for mass rendering, $A_d = 1/M_{ref}s$ under PI motion controller given as follows,

$$Z_{mass}^{PI}(s) = \frac{J_m K_f\, M_{ref} s^3 + \alpha M_{ref} K_f s^2 + I_m K_f\, M_{ref} s}{J_m M_{ref} s^4 + \alpha M_{ref} s^3 + \beta\, M_{ref} s^2 + G_m K_f s + I_m K_f} \tag{4.1}$$

where $\beta = I_m + K_f$.

To establish necessary and sufficient conditions for the passivity of the system described in Eqn. (4.1), it is required to show all conditions in Theorem 3.1 are satisfied.

Proof.

1. $Z(s)$ has no poles in the right half plane: when we apply Routh-Hurwitz stability criterion on Eqn. (4.1) and using Lemma 3.2, it is guaranteed that system has no roots on the open right half plane when the conditions below are satisfied.

   (i) $J_m M_{ref} \geq 0$

   (ii) $\alpha \geq 0$

   (iii) $\frac{G_m\, J_m\, K_f}{\alpha\, \beta} \leq M_{ref}$

   (iv) $\frac{{G_m}^2\, J_m\, K_f}{-I_m\, \alpha^2 + G_m\, \alpha\, \beta} \leq M_{ref}$

   (v) $I_m \geq 0$

2. $Re\{Z(jw)\} \geq 0$ for all $\omega \in (-\infty, \infty)$: From Eqn. (4.1), test polynomial is derived as $R(jw) = a_0\omega^2 + a_1\omega^4$. According to Lemma 3.5, the condition is satisfied if and only if $a_0 = -B_m\, I_m\, K_f^2\, M_{ref} \geq 0$ and $a_1 = K_f^2\, M_{ref}\, (B_m\, M_{ref} - G_m\, J_m + G_m\, M_{ref}) \geq 0$. After simplifications, knowing that both M_{ref} and K_f is positive, following conditions are imposed for passivity:

   (vi) $B_m I_m \leq 0$

   (vii) $\frac{G_m\, J_m}{\alpha} \leq M_{ref}$

   Notice that, condition (i) implies $I_m \leq 0$ since $B_m > 0$.

3. Any poles of Z(s) on the imaginary axis are simple with positive and real residues: Setting $I_m = 0$ and selecting $G_m > 0$, Remark 3.6, makes stability conditions strictly greater than zero except condition (iii). When, $M_{ref} = G_m\, J_m/\alpha$, we have imaginary poles on $s_{1,2} = \pm j\,\sqrt{K_f/J_m}$

(viii) $Res\, Z(s) = \lim_{s \to s_1} (s - s_1)\, Z(s) = \dfrac{K_f}{2} > 0$

□

Our results cover the passivity bounds presented in [24]. Passive mass rendering is achievable when all of these conditions are simultaneously satisfied. However, when $I_m < 0$, it violates the uncoupled stability in the inner motion controller loop, although it is necessary to satisfy condition (vi). As a result, this analysis simplifies mass rendering with a P motion controller by setting $I_m = 0$. The system reduces to the following when $I_m = 0$,

$$Z^P_{mass} = \frac{J_m\, K_f\, M_{ref}\, s^2 + \alpha\, K_f\, M_{ref}\, s}{J_m\, M_{ref}\, s^3 + \alpha\, M_{ref}\, s^2 + (K_f\, M_{ref})\, s + G_m\, K_f} \tag{4.2}$$

The set of necessary and sufficient conditions for this system reduces to conditions (i), (ii), (vii) and (viii). The last condition is automatically satisfied since the physical system parameters are positive. The first condition ensures positive mass rendering ($M_{ref} \geq 0$), while the second condition requires $\alpha \geq 0$ and it is automatically satisfied since physical damping is positive and G_m selected positive according to Remark 3.6. Condition (vii) establishes a lower bound on M_{ref}. This lower bound can be rewritten as in Eqn. (4.3) and it imposes a condition on G_m. Since, both M_{ref} and α are non-negative by stability conditions (i) and (ii), Eqn. (4.3) implies G_m to be positive. Furthermore, when $G_m \to \infty$, $J_m \leq M_{ref}$, which implies that it is not possible to render masses lower than the actual mass present in the system using any causal controllers [17].

$$\frac{M_{ref}\, \alpha}{G_m} \geq J_m \tag{4.3}$$

4.1.1 Passive Physical Equivalent

A passive physical equivalent of the system described in Eqn. (4.1) is presented in Table 4.2a. The parameters of this realization are provided below:

$$c_{1m}^{PI} = \frac{M_{ref}(B_m M_{ref} - G_m J_m + G_m M_{ref})}{(J_m - M_{ref})^2} + \frac{I_m M_{ref}}{B_m}$$
$$b_{1m}^{PI} = \frac{{M_{ref}}^2}{J_m - M_{ref}} - \frac{M_{ref}(B_m G_m - I_m(J_m - M_{ref}))}{B_m^2}$$

For a passive realization to be feasible, all components must be non-negative. Table 4.2a clearly indicates that the damping component requires $I_m \leq 0$ to be non-negative. On the other hand, c_{1m}^{PI} requires $I_m \geq 0$. It's important to note that M_{ref} cannot be lower than J_m, even with the best controllers, as discussed earlier. Thus, $J_m - M_{ref} \leq 0$ always holds, making $c_{1m}^{PI} < 0$ given that $I_m \leq 0$ and G_m is non-negative. This result supports our analysis that passive mass rendering is not possible with a PI motion controller.

We simplify the system defined in Eqn. (4.1) by setting $I_m = 0$ to enable mass rendering with a P controller. The passive physical equivalent is provided in Table 4.2b. Similarly, the parameters are given below:

$$c_{1m}^{P} = \frac{M_{ref}\,\alpha^2}{M_{ref}\,\alpha - G_m J_m}$$
$$b_{1m}^{P} = J_m + \frac{G_m\,{J_m}^2}{M_{ref}\,\alpha - G_m\,J_m}$$

This simpler system's realization requires $\frac{M_{ref}\,\alpha}{G_m}$, c_{1m}^{P}, and b_{1m}^{P} to be non-negative. The first component is feasible when $M_{ref}/G_m \geq 0$ since $\alpha \geq 0$ is required for stability as mentioned in Remark 3.6. Therefore, by applying the same remark and selecting a non-negative G_m, it is sufficient to have $M_{ref} \geq 0$. The last two components are always positive if the inequality $M_{ref}\,\alpha - G_m\,J_m > 0$ is satisfied by having M_{ref} positive, which is a strict version of passivity condition (vii).

4.1.2 Passivity vs. Feasibility of Physical Realization

Since the PI motion controller does not allow us to render mass passively, in this part we only discuss mass rendering with the P motion controller. As discussed earlier, Condition (i), (ii) and (vii) establishes necessary and sufficient conditions of passivity of mass rendering with the P motion controller. The first inerter component covers conditions (i) and (ii) while introducing an additional sufficient condition where $G_m > 0$. Moreover, c_{1m}^P imposes the same lower bound as condition (vii). Thus, this realization introduces sufficient conditions for passivity which are strict versions of necessary and sufficient conditions derived in this section.

4.1.3 Haptic Rendering Performance

Table 4.2b presents the passive physical equivalent of mass rendering with P motion controller and the virtual environment appears as series to physical spring, K_f. Lower branches introduce parasitic components to the system. In the parallel mass-damper pair, b_{1m}^P and c_{1m}^P, the damping term will be dominant in the low frequencies. Thus, the overall low-frequency behavior of the system is defined in Eqn. (4.2) can be interpreted as mass-spring-damper connected in series. Rendered mass at the end-effector described in Eqn. (4.4) and it is combined with the passivity condition (vii). This equation clearly shows that any mass lower than the system's mass cannot be passively rendered.

$$M_{vir} \coloneqq \frac{M_{ref}\,\alpha}{G_m} \geq J_m \tag{4.4}$$

Another interpretation of this passivity condition (vii) is that if we re-write the equations in terms of time constants. The left side of the inequality in Eqn. (4.5) is the time constant of the controlled plant where the right side is the time constant of our controllers. Our haptic rendering performance is limited by the dynamics of the plant by imposing a constraint on the controllers to be slower than the physical

system. In other words, if the system is slower than the controller it would not be able to catch up.

$$\frac{J_m}{\alpha} \leq \frac{M_{ref}}{G_m} \tag{4.5}$$

M_{vir} is felt by the user at the end-effector. However, if c_{1m}^P gets larger it limits our mass rendering performance since parasitic damping will be felt at the interaction port. This happens in two cases: first when lower masses rendered, i.e. $M_{vir} \approx J_m$, or motion controller gain increased, $G_m \to \infty$.

The compliant force sensor, SEA, does not have any effect on the passivity bounds of mass rendering. However, its effects appear in performance. Compliance of the sensor limits mass rendering bandwidth significantly as it is seen in Fig. 4.1. One should prefer stiff sensors or traditional force sensors over SEA and avoid compliance at the end-effector to passively render mass for a larger bandwidth.

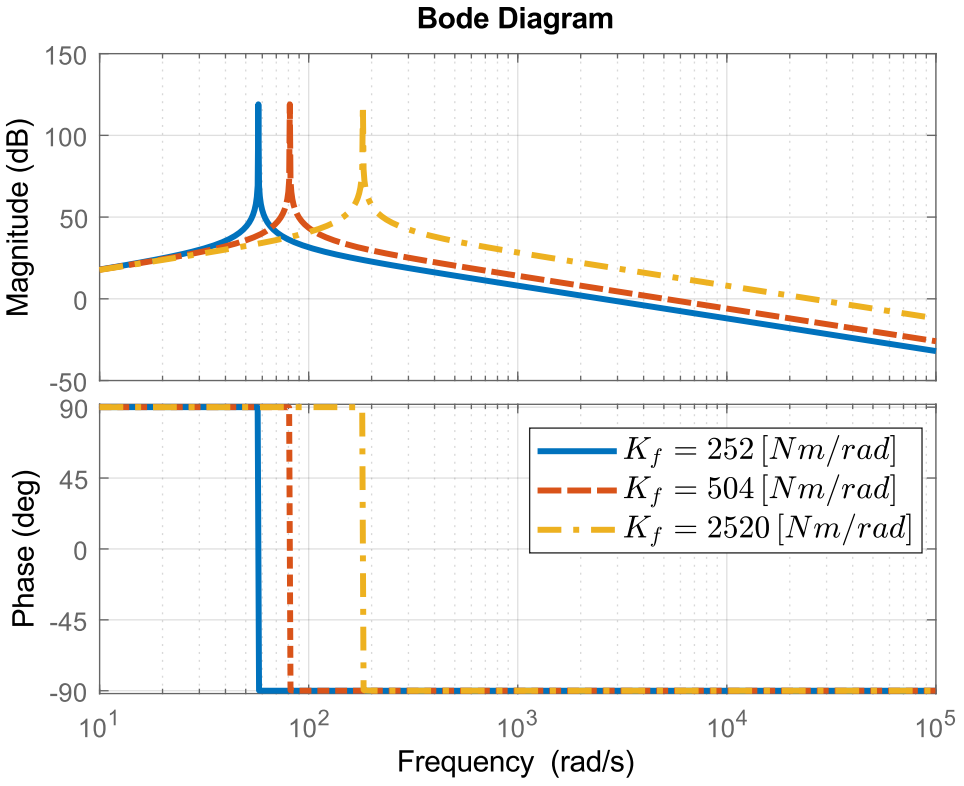

FIGURE 4.1: SEA Stiffness' Effects on Mass Rendering Bandwidth

4.2 Pure Mass Rendering with Lead/Lag Motion Controller

Since PI motion controller does not allow us to render pure mass passively we change inner-motion loop controller represented in Fig. 3.2, $C_m = G_m \frac{s+\eta\,\omega_f}{s+\omega_f}$ where η and $\omega_f \in \mathbb{R}^+$ to show the transition between P to PI controller.

Impedance transfer function in Eqn. (4.1) becomes $Z_{mass}^{lead-lag}(s) =$

$$\frac{J_m\,K_f\,M_{ref}\,s^3 + (\alpha + J_m\,\omega_f)\,K_f\,M_{ref}\,s^2 + (\alpha\,\eta)\,K_f M_{ref}\omega_f\,s}{J_m\,M_{ref}\,s^4 + (\alpha + J_m\,\omega_f)\,M_{ref}\,s^3 + n_0\,s^2 + n_1\,s + G_m K_f\,\eta\,\omega_f} \tag{4.6}$$

where $n_0 = M_{ref}\,(K_f + B_m\,\omega_f + G_m\,\eta\,\omega_f)$ and $n_1 = K_f\,(G_m + M_{ref}\,\omega_f)$.

Proof.

1. $Z(s)$ has no poles in the right half plane: Using Lemma 3.2 gives following stability conditions,

   (i) $J_m M_{ref} \geq 0$

   (ii) $(\alpha + J_m\,\omega_f)\,M_{ref} \geq 0$

   (iii) $G_m K_f\,\eta\,\omega_f \geq 0$

   (iv) $\xi_{mass^{lead-lag}} = c_{m_1}\,K_f^2 + c_{m_2}\,K_f \geq 0$
   where $c_{m_1} = ({M_{ref}}^2\,(G_m + M_{ref}\,\omega_f)\,(\alpha + J_m\,\omega_f) - J_m\,M_{ref}\,(G_m + M_{ref}\,\omega_f)^2)$
   and $c_{m_2} = ({M_{ref}}^2\,(G_m + M_{ref}\,\omega_f)\,(B_m\,\omega_f + G_m\,\eta\,\omega_f)\,(\alpha + J_m\,\omega_f) - G_m\,{M_{ref}}^2\,\eta\,\omega_f\,(\alpha + J_m\,\omega_f)^2)$.

2. $Re\{Z(j\omega)\} \geq 0$ for all $\omega \in (-\infty, \infty)$: According to Eqn. (4.6), the test polynomial can be expressed as $R(j\omega) = a_0\omega^2 + a_1\omega^4$. This function can be further interpreted as $R(j\omega) = (a_0 + a_1\omega^2) \cdot \omega^2$. The condition is satisfied if and only if both $a_0 \geq 0$ and $a_1 \geq 0$, as per Lemma 3.5.

   (v) $\frac{G_m\,J_m\,\eta}{B_m + G_m\,\eta} + \frac{B_m\,G_m\,(\eta-1)}{\omega_f\,(B_m + G_m\,\eta)} \leq M_{ref}$

(vi) $\frac{G_m J_m}{\alpha} \leq M_{ref}$

3. Any poles of Z(s) on the imaginary axis are simple with positive and real residues: our system only has no root on the imaginary axis when the stability conditions given are satisfied.

□

The stability conditions (i) and (iii) necessitate the selection of both M_{ref} and G_m as non-negative. Additionally, by definition, η and ω_f are positive. Therefore, stability conditions (i) to (iii) are automatically satisfied when M_{ref} and G_m are chosen as non-negative.

To simplify $\xi_{\text{mass}^{lead-lag}}(K_f)$ further, one can expand it and eliminate positive common factors, resulting in minimal versions of c_{m_1} and c_{m_2}. Applying Lemma 3.5 reduces these two coefficients to conditions (v) and (vi), thus satisfying the positive realness conditions, which also implies the satisfaction of condition (iv).

Depending on the value of η, conditions (v) and (vi) represent more relaxed or conservative versions of each other. We will examine three specific cases as follows:

Case 1: First, selecting $\eta \in (0, 1)$ results in the second term in condition (v) being negative, as all other parameters are positive either by requirement or physical system parameters. The first term is similar to condition (vi) and presents a smaller lower bound than condition (vi). By multiplying both sides of condition (vi), we obtain $\frac{G_m J_m \eta}{(\alpha)\eta} \geq \frac{G_m J_m \eta}{B_m + G_m \eta}$, which always holds. In addition, we are subtracting a certain amount from the right side of the equation. Thus, in this case, condition (vi) is conservative and valid.

Case 2: Setting $\eta = 1$ encompasses the previous results presented in Section 4.1.

Case 3: The final case is when $\eta \in (1, \infty)$. The analysis from Case 1 can also be applied here. Now, the second term in condition (v) becomes positive, and the effect of η on the first term makes it larger. Thus, condition

(v) provides a larger lower bound compared to condition (vi), and it is more conservative and valid.

4.2.1 Passive Physical Equivalent

System in Eqn. (4.6) can be represented with the realization given in Table 4.2c. Notice that, it has the same structure with mass rendering (PI) realization in Table 4.2a. Physical spring appears as series connected to rendered mass. Knowing that η and ω_f are positive by definition, feasibility of inertia component requires $\frac{M_{ref}(G_m\,\eta+B_m)}{G_m\,\eta} \geq 0$. Other components are described below:

$$
\begin{aligned}
c_{1m}^{lead-lag} &= \frac{M_{ref}\,\omega_f\,(B_m + G_m\,\eta)^2}{\omega_f\,\Lambda - B_m\,G_m\,(\eta-1)} \\
b_{1m}^{lead-lag} &= \frac{J_m\,M_{ref}\,(B_m + G_m\,\eta)}{\Lambda} \\
c_{2m}^{lead-lag} &= \frac{G_m\,M_{ref}\,\psi\,(B_m + G_m\,\eta)^2\,(1-\eta)}{\Lambda\,(\omega_f\,\Lambda - B_m\,G_m\,(\eta-1))^2} \\
b_{2m}^{lead-lag} &= \frac{G_m\,M_{ref}\,\psi\,(B_m + G_m\,\eta)^2\,(1-\eta)}{\Lambda^2\,(\omega_f\,\Lambda - B_m\,G_m\,(\eta-1))}
\end{aligned}
$$

where $\Lambda = B_m\,M_{ref} - G_m\,J_m\,\eta + G_m\,M_{ref}\,\eta$ and $\psi = B_m\,M_{ref}\,(\alpha + M_{ref}\,\omega_f) - B_m\,J_m\,(G_m + M_{ref}\,\omega_f) + G_m\,\eta\,\omega_f\,(J_m - M_{ref})^2$.

Feasibility of realization in Table 4.2c, all components must be non-negative and when non-negativeness of M_{ref} and G_m imposed on these components following conditions must be met:

$$M_{ref} \geq \frac{G_m\,J_m\,\eta}{B_m + G_m\,\eta} + \frac{B_m\,G_m\,(\eta-1)}{\omega_f\,(B_m + G_m\,\eta)} \tag{4.7}$$

$$M_{ref} \geq \frac{G_m\,J_m\,\eta}{B_m + G_m\,\eta} \tag{4.8}$$

The denominator of the first two components imposes Eqn. (4.7)-(4.8), respectively. Controller parameter, η, changes which condition is more conservative. If $\eta \in (0,1)$ Eqn. (4.8) is more conservative and when $\eta \in (1,\infty)$ Eqn. (4.7) is more conservative. Hence, satisfying the conservative one makes other conditions automatically satisfied.

$$\psi\,(1-\eta) \geq 0 \tag{4.9}$$

The last two components require a term in Eqn. (4.9) to be non-negative. Based on the controller we have, lead or lag, sign requirement of ψ changes. First, selecting $\eta \in (0,1)$ yields ψ to be non-negative. Setting $\eta = 1$ automatically satisfies the condition in Eqn. (4.9). The final case is when $\eta \in (1,\infty)$ requires ψ to be non-positive.

$$\begin{aligned}\psi(M_{ref}) = {M_{ref}}^2 + \frac{(B_m\,\alpha - B_m\,J_m\,\omega_f - 2\,G_m\,J_m\,\eta\,\omega_f)}{(B_m\,\omega_f + G_m\,\eta\,\omega_f)}\,M_{ref} \\ + \frac{G_m\,{J_m}^2\,\eta\,\omega_f - B_m\,G_m\,J_m}{(B_m\,\omega_f + G_m\,\eta\,\omega_f)}\end{aligned} \tag{4.10}$$

ψ has form of a quadratic polynomial, $a\,{M_{ref}}^2 + b\,M_{ref} + c$, when it is written in terms of M_{ref}. First, let us examine the polynomial in terms of its roots, $\lambda_{1,2}$, by checking $\Delta_\psi \coloneqq b^2 - 4\,a\,c$

$$\begin{aligned}\Delta_\psi = {B_m}^2\,(\alpha^2 - J_m\,\omega_f\,\,(2\,B_m - J_m\,\omega_f) \\ - 2\,G_m\,J_m\,\omega_f\,\,(2\,\eta - 1)\,)\end{aligned} \tag{4.11}$$

$$\eta - 1 \leq \frac{(B_m + G_m - J_m\,\omega_f)^2}{4\,G_m\,J_m\,\omega_f} \tag{4.12}$$

$\psi(M_{ref})$ is guaranteed to have real roots when Eqn. (4.12) is satisfied. Note that, the right side of the inequality is a positive number when the feasibility requirement of other components is imposed. Thus, it is only possible to exceed the upper bound when $\eta \geq 1$ and violate the inequality. In that case, $\psi(M_{ref})$ will not have any real roots and it will be always positive since it is a positive monic polynomial. This makes the realization unfeasible, since Case 3, where $\eta > 1$, requires non-negative ψ. Hence, for all the cases above we need to have $\Delta_\psi \geq 0$ and satisfy Eqn. (4.12).

Finally, we examine three different cases to define feasible ranges for the realization:

Case a: $\lambda_{1,2} \geq 0$

(a) $M_{ref} \in [0, \lambda_1] \cup [\lambda_2, \infty)$ defines feasible region for lead, $\eta \in (0, 1)$, controller.

(b) $M_{ref} \in [\lambda_1, \lambda_2]$ defines feasible region for lag, $\eta \in (1, \infty)$, controller.

Case b: $\lambda_1 \leq 0$ and $\lambda_2 \geq 0$

(a) $M_{ref} \in [0, \lambda_2]$ defines feasible region for lead, $\eta \in (0, 1)$, controller.

(b) $M_{ref} \in [\lambda_2, \infty)$ defines feasible region for lag, $\eta \in (1, \infty)$, controller.

Case c: $\lambda_{1,2} < 0$

(a) $M_{ref} \in [0, \infty)$ defines feasible region for lead, $\eta \in (0, 1)$, controller.

(b) No feasible region for lag controller, since ψ is always positive for this case when $M_{ref} \geq 0$.

4.2.2 Passivity vs. Feasibility of Physical Realization

Inerter component, $c_{1m}^{lead-lag}$, covers passivity condition (v) as given in Eqn. (4.7). On the other hand, the first damping component gives a relaxed version of condition (vi) which is a sufficient condition for passivity. In addition these, Eqn. (4.9) gives another sufficient condition. Notice that, the sign of $(1 - \eta)$ is a choice based on whether lead or lag controller is implemented. Thus, ψ must be checked as discussed above. Lastly, the non-negativeness of M_{ref} and G_m is a requirement for passivity and these conditions result in necessary and sufficient conditions of passivity in the realization. Moreover, Eqn. (4.11) introduces an additional sufficient condition for passivity. It must be satisfied for feasibility, and it sets an upper bound on how much lag the controller can introduce. There is no such limit on lead due to this condition.

4.2.3 Haptic Rendering Performance

Table 4.2c shows additional components compared to the one in 4.2b due to changing controller to lead/lag. Now, rendered mass at the end-effector has become as defined in Eqn. 4.13 and we have two more parasitic components series mass-damper parallel to previous ones. However, the low-frequency behaviour of the system has not changed since $c_{1m}^{lead-lag}$ will be the dominant term in low frequencies at the lower branch. Similar to the previous case, mass rendering with P motion controller, when minimum mass is tried to be rendered passively this damping term becomes larger. Thus, it limits the fidelity of mass rendering.

$$M_{vir} \coloneqq \left(\frac{B_m}{G_m \, \eta} + 1 \right) M_{ref} \tag{4.13}$$

Now we examine the effects of having lead or lag in the system. First, we add lead to the system by setting $\eta \in (0, 1)$. This results in heavier systems compared to having lag since the term in Eqn. (4.13) $\frac{B_m}{G_m \, \eta}$ becomes larger and larger for same M_{ref}. Moreover, having lead does not change the passivity condition on M_{ref}. Thus, one cannot compensate for this effect by reducing M_{ref}. In addition to these, having lead degrades mass rendering fidelity and the system converges to damping rendering at mid-band as it is shown in Fig. 4.2. On the contrary, the same figure shows having lag increases bandwidth with a cost. The lag controller increases the lower bound on M_{ref} while reducing M_{vir}. For more lag, $M_{vir} \approx M_{ref}$ but for heavier M_{ref}. This increases tracking performance for virtual environment reference by introducing more conservative regions for passivity.

One final thing is that, similar to Eqn. (4.5) passivity condition for the lag controller can be rewritten as Eqn. (4.14). It is clear that the time constant of the controlled plant is now summed with an additional offset and that introduces a lower bound on controller time constant bigger than the system's.

$$\frac{J_m}{B_m + G_m \, \eta} + \frac{B_m}{(B_m + G_m \, \eta)} \, \frac{\eta - 1}{\omega_f \, \eta} \leq \frac{M_{ref}}{G_m \, \eta} \tag{4.14}$$

The analysis indicates that the presence of lead in the system does not contribute to effectively achieving passive rendering of pure mass; instead, it results in a substantial degradation of performance. The introduction of a lag controller presents a trade-off between passivity and performance, as it enhances the fidelity of haptic rendering at the expense of compromising passivity. Fig. 4.2 as η increases mass rendering bandwidth increases. On the contrary, adding lead or lag limits passivity limits compared to Pure Mass Rendering with P motion controller as $M_{vir}^{P} \geq J_m$ shown in Eqn. (4.4). Moreover, Fig. 4.3 shows adding lead or lag to the system cannot render masses lower than system's mass, J_m.

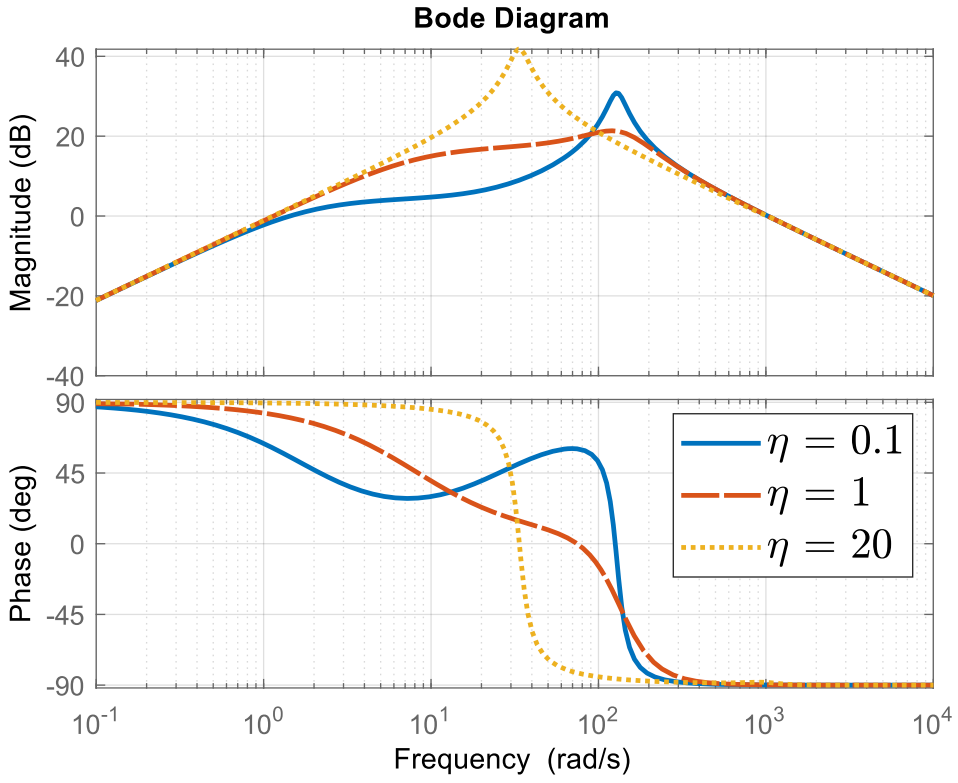

FIGURE 4.2: η effects on Mass Rendering Bandwidth

In addition to parameters in Table 4.1, $M_{ref} = 0.05$ [kg m^2] and $\omega_f = 400$ [rad/s] for the simulation in Fig. 4.2.

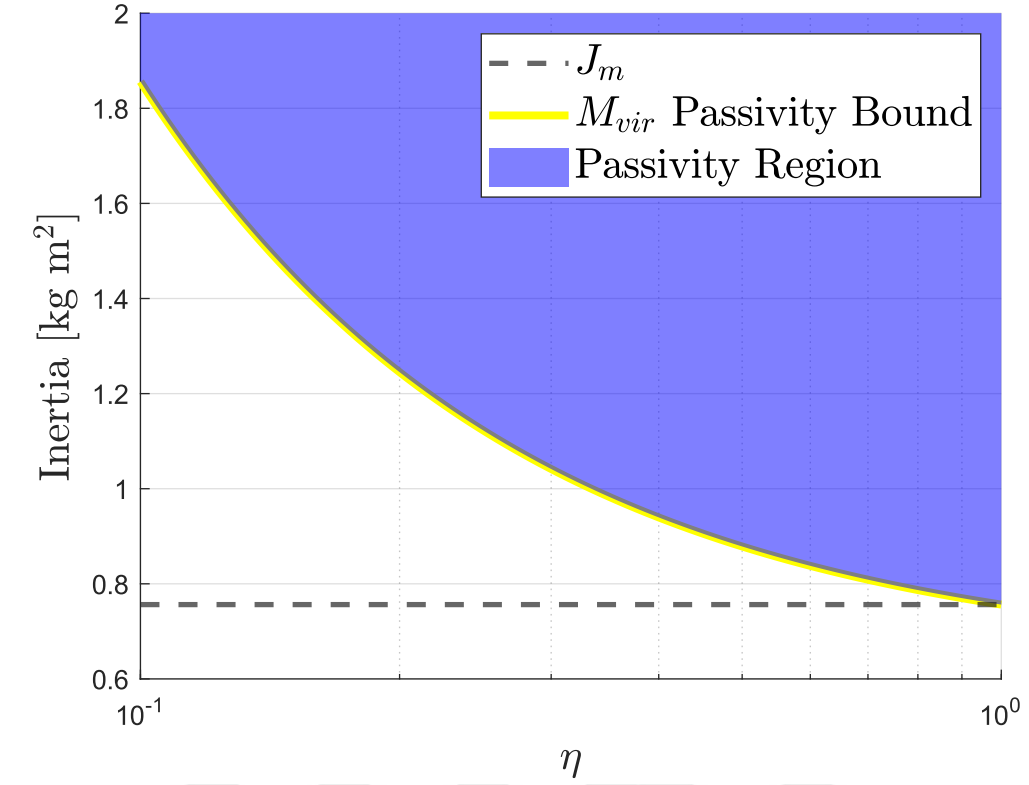

(a) Passively Renderable M_{vir} with Lead Controller

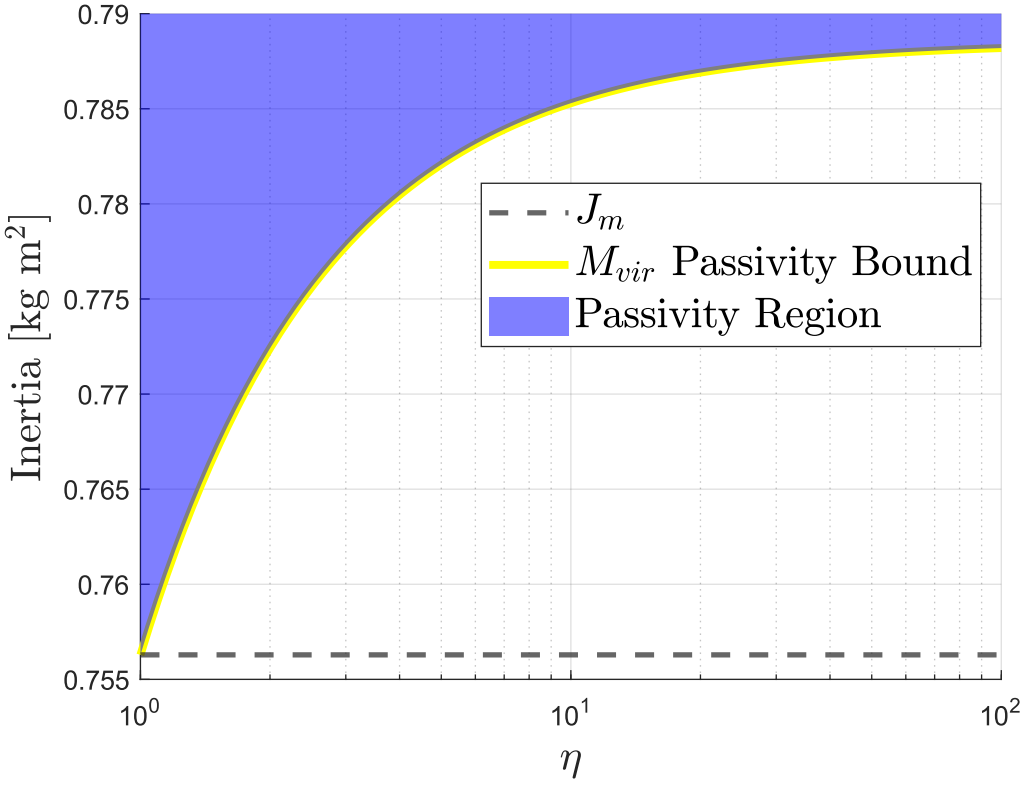

(b) Passively Renderable M_{vir} with Lag Controller

FIGURE 4.3: Passively Renderable M_{vir} Regions for Mass Rendering with Lead-/Lag Controller with SEA under BAC

4.3 Pure Damping Rendering

This section focuses on the investigation of Pure Damping Rendering under BAC with SEA, employing a PI motion controller. We initiate our analysis by defining the desired virtual environment as $A_d = 1/B_{ref}$, characterized by the impedance transfer function $Z^{PI}_{damping}(s) =$

$$\frac{J_m\, B_{ref}\, K_f\, s^2 + \alpha\, B_{ref}\, K_f\, s + B_{ref}\, I_m\, K_f}{J_m\, B_{ref}\, s^3 + \alpha\, B_{ref}\, s^2 + (B_{ref}\, \beta + G_m\, K_f)\, s + I_m\, K_f} \tag{4.15}$$

Proof.

1. $Z(s)$ has no poles in the right half plane: Using Lemma 3.3 gives following stability conditions,

   (i) $J_m B_{ref} \geq 0$

   (ii) $\alpha\, B_{ref} \geq 0$

   (iii) $I_m\, K_f \geq 0$

   (iv) $B_{ref} \geq \frac{K_f}{\beta} \frac{I_m\, J_m - G_m\, \alpha}{\alpha}$

2. $Re\{Z(j\omega)\} \geq 0$ for all $\omega \in (-\infty, \infty)$: Based on Eqn. (4.15), we derive the test polynomial as $R(j\omega) = a_0\omega^2 + a_1\omega^4$. This function can be interpreted as $R(j\omega) = (a_0 + a_1\omega^2) \cdot \omega^2$. Using Lemma 3.5, we obtain the conditions $a_0 = B_{ref}\, I_m^2\, K_f^2 \geq 0$ and $a_1 = B_{ref}\, K_f^2\, (G_m^2 + B_{ref}\, \alpha + B_m\, G_m - I_m\, J_m) \geq 0$. After simplification, removing B_{ref} and K_f as common factors since they are both positive, we have the following conditions:

   (v) $B_{ref}\, I_m^2 \geq 0$

   (vi) $I_m \leq \frac{\alpha\, (B_{ref} + G_m)}{J_m}$

3. Any poles of Z(s) on the imaginary axis are simple with positive and real residues: our system only has no root on the imaginary axis when the stability conditions given are satisfied.

□

Stability conditions (i) and (iii) constrain our controller gains to be positive. Thus, we cannot render negative damping with BAC to compensate for the damping apparent in the system. Stability condition (iv) is a relaxed version of the positive realness condition (vi), as $\frac{K_f}{\beta} \in (0, 1)$ for SEA and I_m is non-negative. It also encompasses the latter condition when $K_f \to \infty$. Introducing SEA to the system relaxes the stability conditions but does not affect the passivity conditions. The positive realness condition (vi) is more conservative, and satisfying it is necessary and sufficient to passively render pure damping with positive controller gains. Moreover, satisfying the condition makes stability conditions strictly greater than zero. According to Lemma 3.5, the system will not have any imaginary poles.

Moreover, this condition presents a trade-off between I_m and B_{ref}. One can select a more damped system to achieve better low-frequency behavior by increasing B_{ref} and relaxing the upper bound on I_m. However, increasing damping in the system will significantly increase energy dissipation.

Finally, damping rendering under BAC corresponds to null rendering with a P (torque) - PI (motion) controller under VSIC. Thus, when the substitution $G_t = 1/B_{ref}$ is made, our results match those presented in [32].

4.3.1 Passive Physical Equivalent

A passive physical equivalent of the system described in Eqn. (4.15) is presented in Table 4.2d. The parameters of this realization are provided below:

$$c_{1d}^{PI} = -\frac{B_{ref}\,(B_{ref} - B_m)}{B_{ref} + G_m} - \frac{B_{ref}\,I_m\,J_m}{(B_{ref} + G_m)^2}$$
$$b_{1d}^{PI} = -\frac{B_{ref}\,J_m}{B_{ref} + G_m} - \frac{B_{ref}\,(B_{ref} - B_m)}{I_m}$$

To ensure a feasible passive physical equivalent, all components need to be non-negative. Since K_f is a physical system parameter, it is always positive. Additionally, the virtual pure damping in the system is represented as B_{ref}, and it must be non-negative.

Ensuring that $B_{ref} \geq 0$ leaves us with the requirement that $B_{ref} + G_m > 0$ to make the inerter term positive. The other components, c_{1d}^{PI} and b_{1d}^{PI}, introduce more complex conditions for feasibility. Removing the common factor of B_{ref} gives the following Eqn. (4.16)-(4.17) for the inerter and damper, respectively.

$$I_m \left((B_{ref} - B_m) (B_{ref} + G_m) + I_m J_m \right) (B_{ref} + G_m) < 0 \tag{4.16}$$

$$\left((B_{ref} - B_m) (B_{ref} + G_m) + I_m J_m \right) (B_{ref} + G_m)^2 < 0 \tag{4.17}$$

Eqn. (4.17) introduces the upper bound on I_m and it is required to have a feasible damper component in the realization. This term also appears in Eqn. (4.16), and since $(B_{ref} + G_m) > 0$ is also required for feasibility of c_{1d}^{PI}, it implies $I_m > 0$ for the inerter component to be positive.

$$\frac{(B_m - B_{ref}) (B_{ref} + G_m)}{J_m} > I_m \tag{4.18}$$

4.3.2 Passivity vs. Feasibility of Physical Realization

Feasibility of the realization covers sufficient conditions for passive damping rendering. First of all, selecting B_{ref} as positive is a more conservative version of the passivity condition (i). Similarly, I_m must be positive for feasibility, which is a strict version of the passivity condition (iii). In addition, the realization provides another upper bound on I_m as given in Eqn. (4.18). Since it is evident that $\alpha \geq B_m - B_{ref}$, the inequality in Eqn. (4.19) always holds, and when Eqn. (4.18) is satisfied, and passivity condition (vi) is automatically met.

$$\frac{\alpha\left(B_{ref}+G_m\right)}{J_m} \geq \frac{\left(B_m-B_{ref}\right)\left(B_{ref}+G_m\right)}{J_m} > I_m \tag{4.19}$$

Lastly, $B_{ref}+G_m$ should be non-negative to have a non-negative upper bound on I_m in passivity condition (vi) since $\frac{\alpha}{J_m}$ is always positive. On the other hand, the realization requires this term to be positive for feasibility. Thus, ensuring $B_{ref}+G_m$ to be positive is necessary for this realization, and it is sufficient for passivity.

4.3.3 Haptic Rendering Performance

Pure damping rendering with PI motion controller acts like parallel mass-damper pair series to physical spring as it is shown in Table 4.2d. Right most branch will introduce parasitic inerter, b_{1d}^{PI}, at low frequencies and it will be added up with the term $\frac{B_{ref}\,J_m}{B_{ref}+G_m}$. This parasitic inerter does not affect damping rendering significantly at low frequencies since $B_{vir}=B_{ref}$ is dominant in that region. Passivity condition (vi) can be expressed in terms of B_{vir} as in Eqn. (4.22), since it clearly shows a lower bound on passively renderable damping. Integral controller gain, I_m, can be increased to further increase the performance of damping rendering by lowering the effects of parasitic inerter as seen in Eqn. (4.20). This relation also appears in passivity conditions as well. However, due to passivity I_m is limited by B_{ref}. Thus, haptic rendering performance can be compromised to achieve better low-frequency performance by increasing I_m. Moreover, B_{ref} can be set lower values than B_m even though negative environment reference is not allowed. It makes damping compensation possible. Simulated results can confirm this, Fig 4.4 shows the frequency response of the system described in Eqn. (4.15) and lower frequency response magnitude is significantly lower than the system's damping. In addition to system parameters, $B_{ref}=0.1$ [Nm s / rad], $G_m=0.05$ [Nm s / rad] and $I_m=2$ [Nm/rad] are set to controllers.

$$b_{total}=\frac{B_{ref}\left(B_m-B_{ref}\right)}{I_m} \tag{4.20}$$

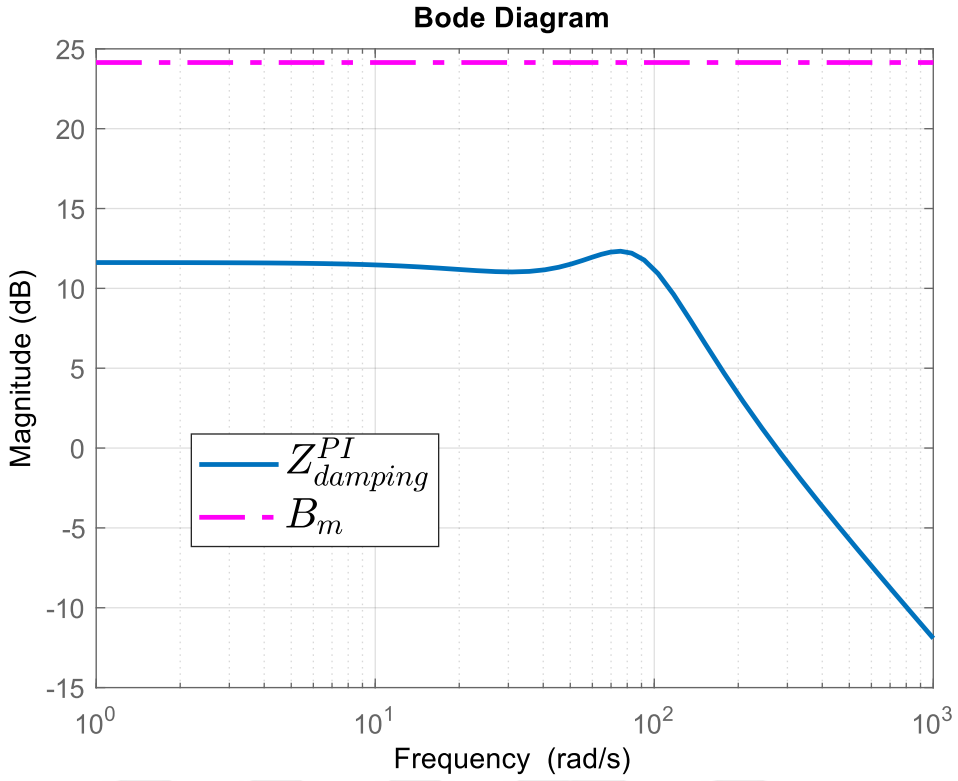

FIGURE 4.4: Damping compensation with PI motion controller

Passivity condition (vi) presents a trade-off between controller gains and system dynamics as in Eqn. (4.21). Similar to mass rendering, it requires the controller to be slower than the system. Notice that the proportional gain of the motion controller, G_m, can be further increased to relax upper-bound on I_m. However, it reduces the haptic rendering fidelity of pure damping as in Fig. 4.5 for $B_{ref} = 0.05$ [Nm s / rad] and $I_m = 1$ [Nm/rad].

$$\frac{J_m}{\alpha} \leq \frac{B_{ref} + G_m}{I_m} \tag{4.21}$$

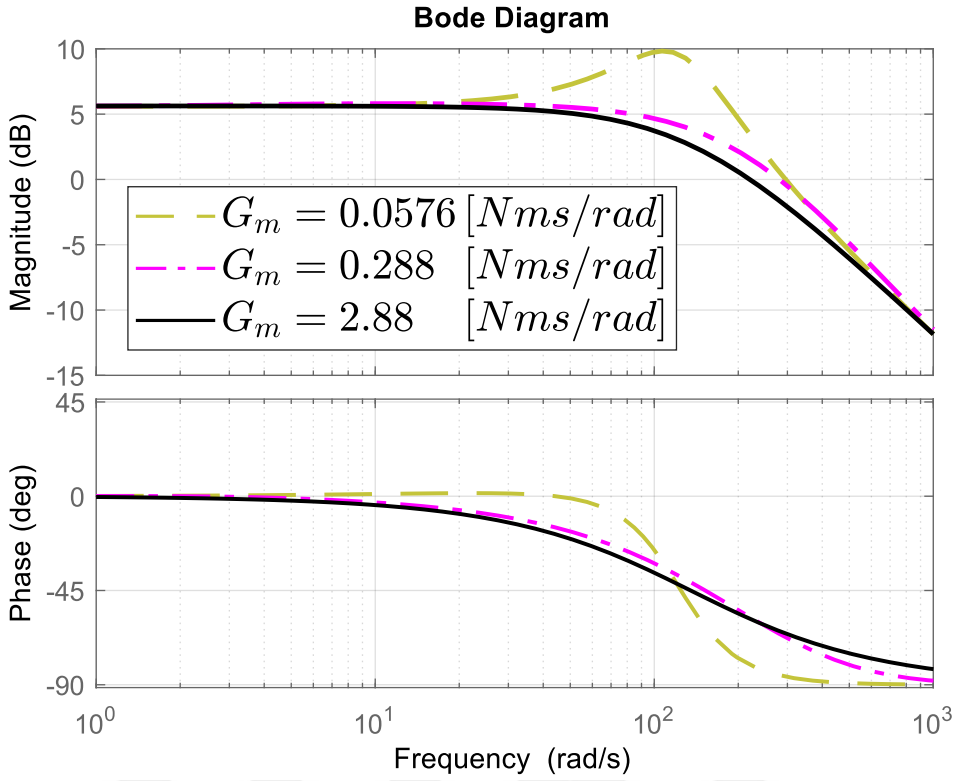

FIGURE 4.5: Proportional Motion Controller Effect on Haptic Rendering Fidelity of Damping Rendering with PI Motion Controller

$$\frac{J_m\, I_m}{\alpha} - G_m \leq B_{vir} \tag{4.22}$$

Finally, we present the passively renderable pure damping region according to Eqn. (4.22) with different integral motion controller gains in Fig. 4.6 where G_m is set to 0.0576 [Nm s / rad].

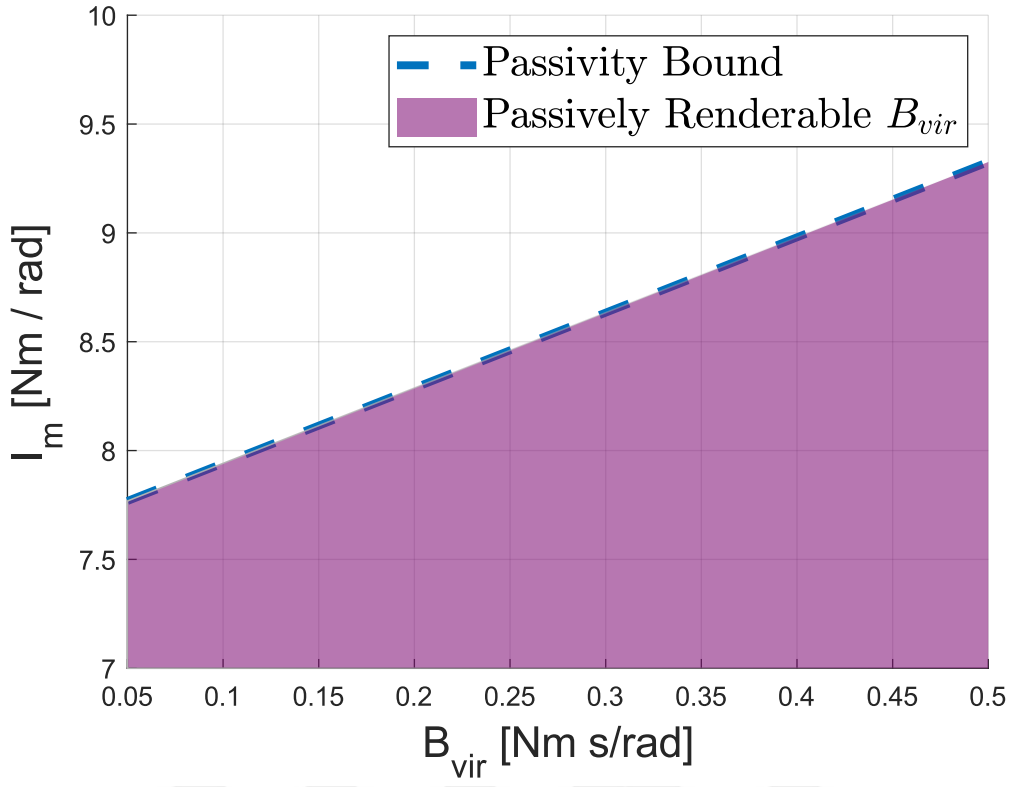

FIGURE 4.6: Passively Renderable Region for Damping Rendering with PI Motion Controller

4.4 Mass-Damping Rendering

In this section, we examine the combination of the previous two virtual elements and our desired virtual environment becomes $A_d = \frac{1}{M_{ref}\, s + B_{ref}}$ with PI motion controller, system's impedance transfer function derived as $Z^{PI}_{mass-damping}(s) =$

$$\frac{J_m\, K_f\, M_{ref}\, s^3 + n_2\, K_f\, s^2 + (B_{ref}\, \alpha + I_m\, M_{ref})\, K_f\, s + B_{ref}\, I_m\, K_f}{J_m\, M_{ref}\, s^4 + n_2\, s^3 + (B_{ref}\, \alpha + \beta\, M_{ref})\, s^2 + n_3\, s + I_m\, K_f} \tag{4.23}$$

where, $n_2 = (B_{ref}\, J_m + \alpha\, M_{ref})$ and, $n_3 = (B_{ref}\, \beta + G_m\, K_f)$.

Proof.

1. $Z(s)$ has no poles in the right half plane: Analytical conditions for stability of fourth-order system is given in [30]. Applying those solutions to our system yields the following conditions on stability,

   (i) $J_m M_{ref} \geq 0$

   (ii) $n_2 \geq 0$

   (iii) $I_m \geq 0$

   (iv) $\xi_{md} = n_3\, n_2\, (B_{ref}\, \alpha + M_{ref}\, \beta) - I_m\, K_f\, {n_2}^2 - J_m\, M_{ref}\, {n_3}^2 \geq 0$

2. $Re\{Z(jw)\} \geq 0$ for all ω: From Eqn. (4.1), test polynomial is derived as $R(jw) = a_0 + a_1\omega^2 + a_2\omega^4$. Using Lemma 3.5,

   (iv) $B_{ref}\, I_m^2\, K_f^2 \geq 0$

   (vi) $\frac{G_m\, J_m}{\alpha} \leq M_{ref}$

   (vii) $B_{ref}\, \alpha\, (B_{ref} + G_m) - I_m(J_m B_{ref} + B_m M_{ref}) \geq -2\, |I_m|\, \sqrt{\Delta}$

   where $\Delta = \sqrt{B_{ref}\, M_{ref}\, (\alpha\, M_{ref} - G_m\, J_m)}$.

3. Any poles of Z(s) on the imaginary axis are simple with positive and real residues: our system only has no root on the imaginary axis when the stability conditions given are satisfied.

□

Conditions (i), (iii), and (iv) dictate the non-negativeness of M_{ref}, I_m, and B_{ref}, respectively. Notice that the additional virtual damping (B_{ref}) to the system relaxes the condition on I_m, and it is not required to have $I_m \leq 0$ for passivity, in contrast to condition (vi) presented in Section 4.1.

In addition to these, knowing $\alpha \geq 0$ according to Remark 3.6, condition (ii) always holds. Another point to consider is that the lower bound on M_{ref} remains unchanged, and it is the same as in the previous mass rendering analysis presented in this article. Any addition of virtual elements does not change the lower bound on

M_{ref}. Furthermore, the same condition is discussed in Section 4.1 and it imposes positivity of G_m.

All parameters are required to be positive for passivity, as explained above. Selecting all parameters as positive is sufficient for stability, and condition (iv) will always be satisfied. Thus, there will be no roots on the imaginary axis.

Condition (vii) presents a trade-off between I_m and $B_{ref} - M_{ref}$ similar to the ones presented in Section 4.3 and 4.6. Since, condition (iii) requires non-negative I_m for stability we can remove the absolute value from I_m in condition (vii) and re-write the equation as follows,

$$\frac{B_{ref}\,\alpha\,(B_{ref} + G_m)}{J_m\,B_{ref} + B_m\,M_{ref} - 2\,\sqrt{\Delta}} \geq I_m \tag{4.24}$$

Eqn. (4.24) covers condition (vi) in Section 4.3 when M_{ref} is set to 0. Increasing B_{ref} gives a higher upper bound on I_m, as discussed in Section 4.3. However, it is not trivial to comment on the effect of M_{ref} directly from this equation.

Let's consider the case where $\alpha\,M_{ref} = G_m\,J_m$. In this scenario, $\Delta \to 0$, and Eqn. (4.24) becomes a sufficient condition given below:

$$\frac{\alpha\,B_{ref}\,(B_{ref} + G_m)}{J_m\,B_{ref} + M_{ref}\,B_m} \geq I_m \tag{4.25}$$

Based on Eqn. (4.25), increasing M_{ref} will lead to a lower upper bound on I_m. Therefore, while increasing B_{ref} improves the system's performance by relaxing the upper bound on I_m, higher values of M_{ref} result in the opposite effect.

4.4.1 Passive Physical Equivalent

The passive physical equivalent of mass-damping rendering, as defined by Eqn. (4.23), is presented in Table 4.2e. The physical filter appears as a series in the virtual rendered environment with parameters M_{ref} and B_{ref}. It is a requirement for the virtual environment parameters to be non-negative for the feasibility of the realization. The other components are listed below:

$$
\begin{aligned}
k_{1md}^{PI} &= \frac{B_{ref}\, I_m}{\gamma_1} \\
b_{1md}^{PI} &= \frac{J_m\, M_{ref}}{\gamma_2} \\
c_{1md}^{PI} &= \frac{B_{ref}\,(B_{ref}+G_m)+I_m\, M_{ref}}{\gamma_1} - B_{ref} + \frac{B_{ref}\, I_m - \gamma_2}{\gamma_1^2} \\
c_{2md}^{PI} &= \frac{B_m\, I_m \gamma_2 - (B_m\,\alpha + I_m\, J_m)\gamma_1}{\gamma_1^2} \\
&\quad - \frac{J_m^2(B_{ref}+\alpha) - J_m\, M_{ref}(B_m+\alpha)}{\gamma_2^2} \\
b_{2md}^{PI} &= \frac{J_m(B_m+\alpha)}{\gamma_1} - \frac{J_m^2}{\gamma_2} - \frac{\gamma_2(B_m\,\alpha + I_m\, J_m)}{\gamma_1^2} \\
&\quad + \frac{B_m\, I_m {\gamma_2}^2}{\gamma_1^3}
\end{aligned}
$$

where $\gamma_1 = B_{ref} - B_m$ and $\gamma_2 = M_{ref} - J_m$.

The first two components impose simple conditions for feasibility, which require the virtual mass and damper to be greater than the physical inertia and damping in the system, i.e., $M_{ref} > J_m$ and $B_{ref} > B_m$. Imposing constraints from the first two components on c_{1md}^{PI} results in the following upper bound on M_{ref}.

$$
M_{ref} < \frac{B_{ref}\, I_m\, J_m - B_{ref}\, {\gamma_1}^2 + B_{ref}\, \gamma_1 (B_{ref}+G_m)}{B_m\, I_m} \tag{4.26}
$$

The damping term, c_{2md}^{PI}, is feasible when Eqn. (4.27) is satisfied. Although it is not easy to interpret this condition analytically, numeric solutions can be utilized to find feasible samples.

$$\gamma_2{}^2\, d_1 - \gamma_1{}^2\, d_2 < 0 \tag{4.27}$$

where $d_1 = \gamma_1(B_m\,\alpha + I_m\,J_m) - B_m\,I_m\gamma_2$ and $d_2 = J_m(\alpha\gamma_2 - B_{ref}\,J_m + B_m\,M_{ref})$.

The last component gives the following equation for feasibility, and it is enough to satisfy the numerator using the fact that both $\gamma_{1,2}$ are positive from the first two constraints.

$$0 < \frac{(B_m\gamma_2 - J_m\gamma_1)(J_m\gamma_1^2 - \alpha\gamma_1\gamma_2 + I_m\gamma_2^2)}{\gamma_1^3\gamma_2} \tag{4.28}$$

4.4.2 Passivity vs. Feasibility of Physical Realization

First of all, non-negativity M_{ref} and B_{ref} a necessary and sufficient conditions for passivity and they are also required for the feasibility of the realization. Moreover, γ_1 and γ_2 give more conservative versions of passivity conditions (vi) and (vii). Even though passivity analysis does not give any upper bound on M_{ref}, the feasibility of the realization gives one a sufficient condition for passivity as given in the Eqn. (4.26).

4.4.3 Haptic Rendering Performance

Virtual environment change with the addition of virtual damping appears parallel to rendered mass series to physical spring in Table 4.2e. This change results in additional spring at lower branches compared to pure mass rendering realizations in Table 4.2a-c. The dominant term coming from branches below is the spring term, k_{md}^{PI}, in lower frequencies. The spring converges to I_m when $B_{ref} \gg B_m$. The main benefit of the addition of virtual damping to the environment is to have I_m in the motion controller and it appears as a parasitic spring series to the rendered impedances. It improves the low-frequency behaviour of the system since motion controllers without an integral term are subjected to drift. However, the low-frequency behaviour of our system changes from mass to damping with this

addition. Rendered mass becomes Eqn. (4.29) compared to pure mass rendering given in Eqn. (4.4) while rendered damping stayed the same compared to pure damping rendering Eqn. (4.30). Furthermore, Eqn. (4.29) tells us that if more damping is added than the systems', e.g. $B_{ref} \geq B_m$, mass compensation can be done since $M_{vir} \to 0$. On the contrary, if damping compensation is done, e.g. $B_{ref} < B_m$, more mass must be added to the system by increasing M_{ref} to satisfy $M_{vir} \geq 0$. Mass compensation is further strengthened by having SEA at the system since ${B_{ref}}^2/K_f$ term helps us to compensate for more mass at the expense of reducing haptic rendering fidelity.

$$M_{vir} = M_{ref} - \frac{{B_{ref}}^2}{K_f} - \frac{B_{ref}\left(B_{ref} - B_m\right)}{I_m} \tag{4.29}$$

$$B_{vir} = B_{ref} \tag{4.30}$$

We further examine a sufficient version of the passivity condition (vii) given in Eqn. (4.25) by re-writing as in Eqn. (4.31). The right-hand side of the inequality is the same as the previous analysis in the sections above and defines the time constant of the controlled plant. Now, the time constant of the damping controller in Eqn. (4.21) with additional terms coming from mass rendering. It presents a trade-off between damping rendering and mass rendering as we discussed above. The damping controller should be slower than a mass controller and the gap between them is increased when damping compensation is done due to a factor of B_m/B_{ref}.

$$\frac{B_{ref} + G_m}{I_m} - \frac{M_{ref}}{\alpha}\frac{B_m}{B_{ref}} \geq \frac{J_m}{\alpha} \tag{4.31}$$

Damping and mass compensation trade-off is visualized in Fig. when M_{ref} is set to the minimum value, $\frac{J_m G_m}{\alpha}$. For simplicity of the simulation, tranmission ratio is taken as 1, $G_m = 0.0864$ [Nm s / rad] and $I_m = 0.05$ [Nm/rad] are set to controllers.

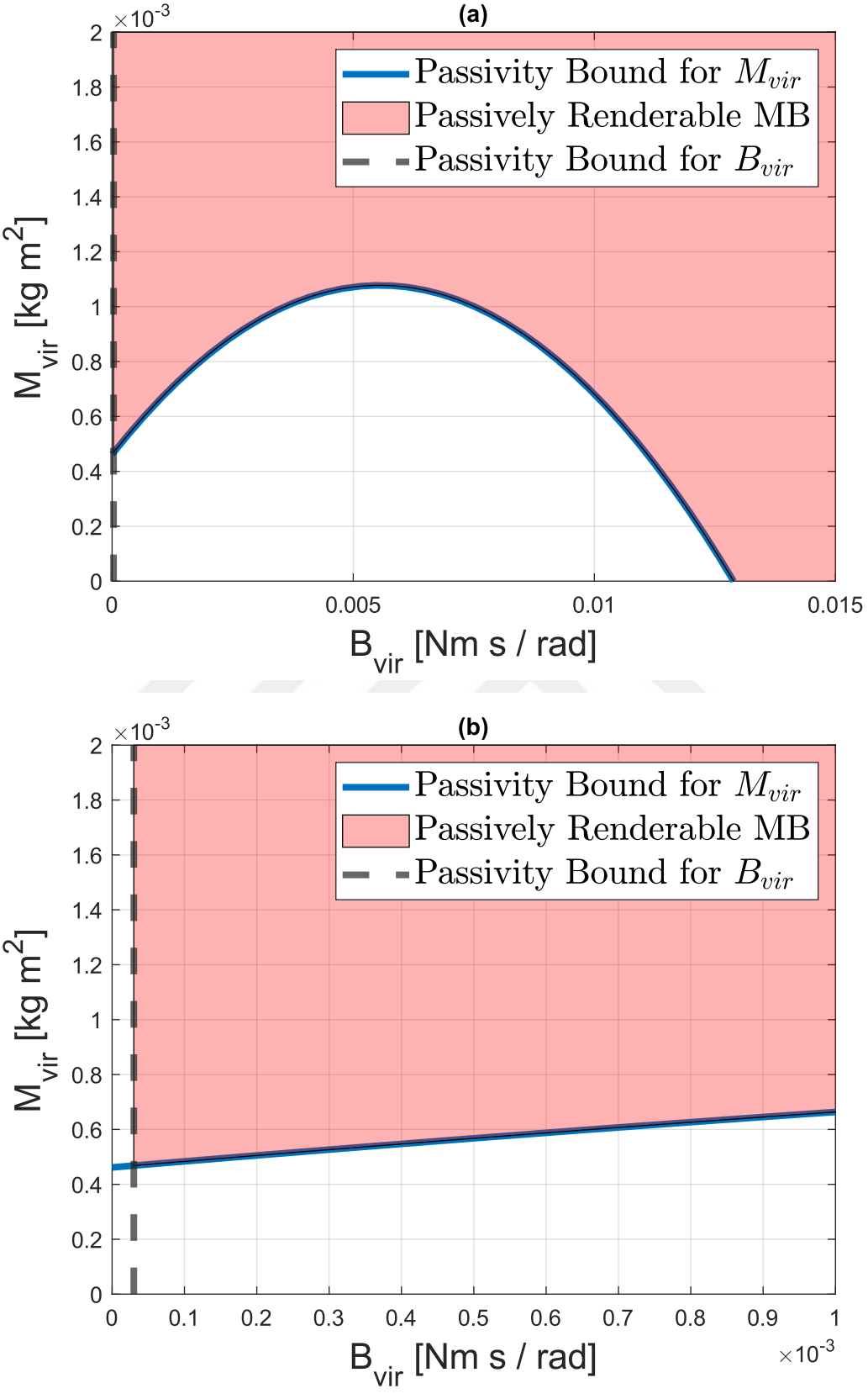

FIGURE 4.7: Passively Renderable Regions for Mass-Damping Rendering with PI Motion Controller

MB plot in Fig. 4.7a clearly shows that increasing B_{vir} results in lower rendered mass. In addition to this, passivity does not allow fully compensate for the damping as seen in Fig. 4.7b. Moreover, Eqn. (4.32) analytically shows the peak point of the curve. Hence, we can see that as $K_f \to 0$, the peak converges to lower levels of B_{ref}.

$$\frac{B_m\, K_f}{2\,(I_m + K_f)} \tag{4.32}$$

4.5 Pure Spring Rendering

When desired virtual environment changed to $A_d = s/K_{ref}$, impedance transfer function becomes $Z^{PI}_{spring}(s) =$

$$\frac{J_m\, K_{ref}\, K_f\, s^2 + \alpha\, K_{ref}\, K_f\, s + I_m\, K_{ref}\, K_f}{J_m\, K_{ref}\, s^3 + (\alpha\, K_{ref} + G_m\, K_f)\, s^2 + (\beta\, K_{ref} + I_m\, K_f)\, s} \tag{4.33}$$

Note that, for the causal implementation of spring rendering, velocity sensors can be utilized to calculate the time rate of change of end-effector forces since SEA acts like a force sensor.

Proof.

1. $Z(s)$ has no poles in the right half plane: Using Lemma 3.3 gives following stability conditions,

   (i) $J_m K_{ref} \geq 0$

   (ii) $a_{s_2} = \alpha\, K_{ref} + G_m\, K_f \geq 0$

   (iii) $a_{s_2}(I_m\, K_{ref} + I_m\, K_f + K_{ref}\, K_f) \geq 0$

2. $Re\{Z(j\omega)\} \geq 0$ for all $\omega \in (-\infty, \infty)$: The test polynomial is derived from Eqn. (4.33) as $R(j\omega) = a_0\omega^2 + a_1\omega^4$. This function can be interpreted as $R(j\omega) = (a_0 + a_1\omega^2) \cdot \omega^2$. According to Lemma 3.5, the condition is

satisfied if and only if $a_0 = K_{ref}\, K_f^2\, (B_m\, I_m + B_m\, K_{ref} + G_m\, K_{ref}) \geq 0$ and $a_1 = G_m\, J_m\, K_{ref}\, K_f^2 \geq 0$, given that the system parameters are positive, $I_m \geq 0$ as per Remark 3.6, and $K_{ref} \geq 0$. This reduces the conditions to the following:

(iv) $B_m\, (I_m + K_{ref}) + G_m\, K_{ref} \geq 0$

(v) $G_m \geq 0$

3. Any poles of Z(s) on the imaginary axis are simple with positive and real residues: our system only has one root on the imaginary axis where $s = 0$.

(vi) $Res\, Z(s) = \lim_{s \to 0} sZ(s) = \dfrac{I_m K_{ref} K_f}{I_m K_{ref} + K_f (I_m + K_{ref})} > 0$

□

Stability and positive realness dictate $K_{ref} \geq 0$ and $G_m \geq 0$, respectively. According to Remark 3.6, $I_m \geq 0$ for inner-motion loop stability. In addition to these, the residue condition of Theorem 3.1 for spring rendering is equivalent to the impedance of I_m, K_f and K_{ref} connected in series as springs. Stability conditions (ii) and (iii) show that the stability conditions in [24] for pure spring rendering are relaxed by additional positive terms introduced by K_f. The conditions listed above present necessary and sufficient conditions for the passivity of pure spring rendering. It is required to select all parameters as non-negative and it is enough to satisfy all the conditions.

4.5.1 Passive Physical Equivalent

The system described in Eqn. (4.33) is presented in Table 4.2f. It is evident to say that K_f, K_{ref} and I_m should be non-negative for feasibility. Parallel components to these springs are listed below,

$$
\begin{aligned}
k_{1s}^{PI} &= \frac{{K_f}^2 \left(I_m + K_{ref}\right)}{I_m K_{ref} + I_m K_f + K_{ref} K_f} \\
c_{1s}^{PI} &= \frac{{K_f}^2 \left(\alpha {K_{ref}}^2 + B_m I_m K_{ref}\right)}{\left(I_m K_{ref} + I_m K_f + K_{ref} K_f\right)^2} \\
c_{2s}^{PI} &= -\frac{K_{ref} {K_f}^2 \phi}{\left(I_m + K_{ref}\right)\left(I_m K_{ref} + I_m K_f + K_{ref} K_f\right)^2} \\
b_{1s}^{PI} &= -\frac{K_{ref} {K_f}^2 \phi}{G_m \left(I_m K_{ref} + I_m K_f + K_{ref} K_f\right)^2}
\end{aligned}
$$

where $\phi = G_m \left(G_m K_{ref} + B_m \left(I_m + K_{ref}\right)\right) - J_m \left(I_m + K_{ref}\right)^2$.

The first two components are always non-negative, since spring constants are required to be non-negative from parallel springs in the realization. The last two components impose the following conditions for feasibility,

$$\phi \leq 0 \tag{4.34}$$

$$\frac{\phi}{G_m} \leq 0 \tag{4.35}$$

To satisfy both of the Eqn. (4.34)-(4.35), ϕ should be non-positive and G_m should be non-negative. This realization is only feasible in the range of where ϕ is non-positive. It can be thought of as a second-order polynomial in terms of $I_m + K_{ref}$ and the feasible region is covered when the polynomial is non-positive.

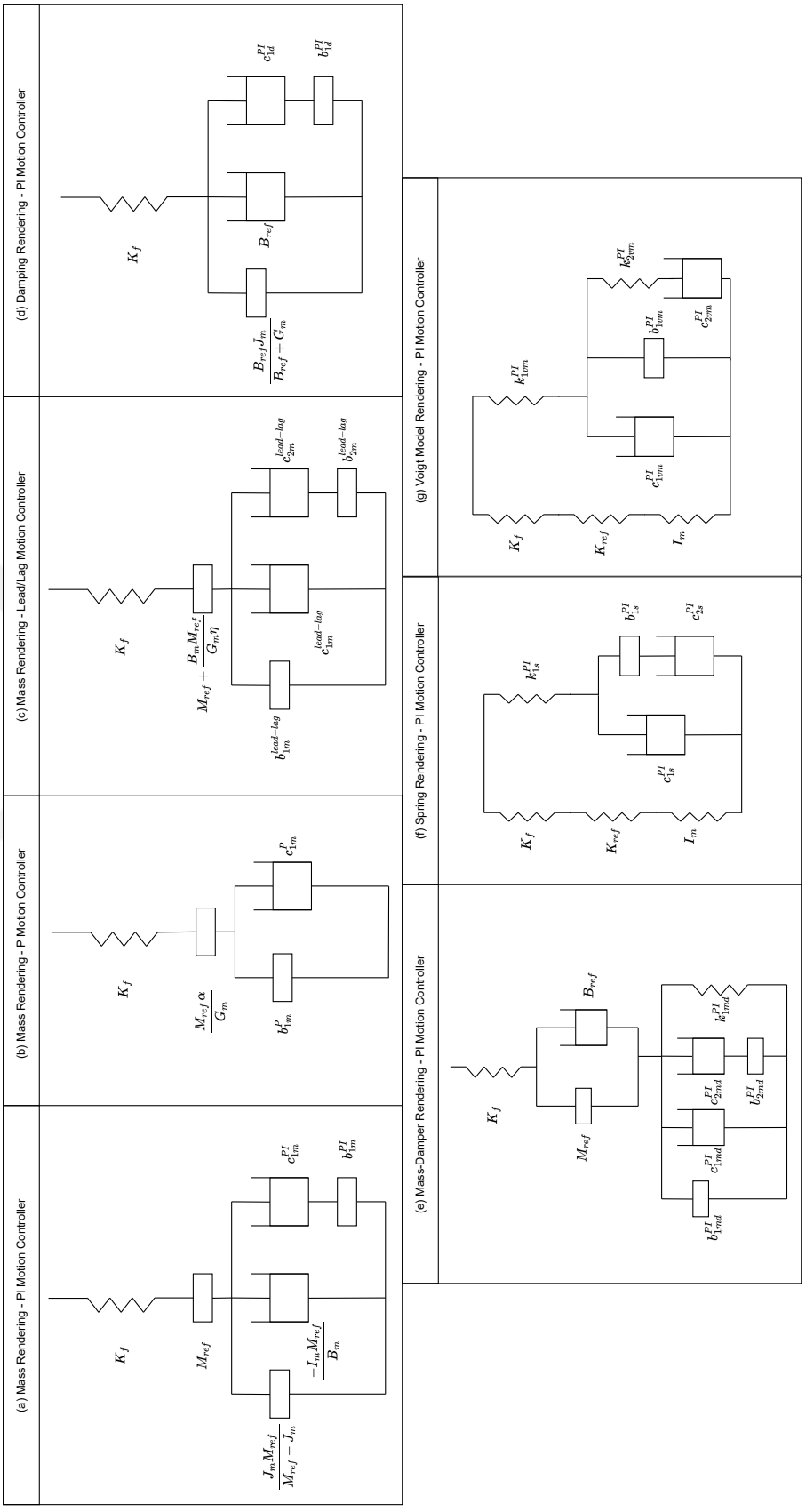

TABLE 4.2: Passive physical equivalents for SEA under BAC

4.5.2 Passivity vs. Feasibility of Physical Realization

First of all, the parallel spring introduces the requirement of non-negativeness for spring constants K_{ref}, K_f, and I_m. Physical system stiffness is inherently positive, while the stability condition of passivity requires K_{ref} and I_m to be non-negative. Additionally, in line with condition (v), the realization requires non-negativeness on G_m to satisfy Eqn. (4.35).

Eqn. (4.34) defines an upper bound on condition (iv), which can be expressed in the following form:

$$(B_m\,(I_m + K_{ref}) + G_m\,K_{ref}) \leq \frac{J_m\,(I_m + K_{ref})^2}{G_m} \tag{4.36}$$

Eqn. (4.36) introduces a sufficient condition for passivity, which must be satisfied for the feasibility of the realization.

4.5.3 Haptic Rendering Performance

Spring rendering with PI motion controller consists of two parallel branches of passive elements compared to other systems as seen in Table 4.2f. The first branch is the rendered virtual environment while the second branch introduces parasitic damping c_{1s}^{PI} in the low-frequency region. Rendered stiffness, K_{vir}, defined as in Eqn. (4.37) and, clearly shows series of connections of springs.

$$K_{vir} = \frac{I_m\,K_{ref}\,K_f}{(I_m\,K_{ref} + K_f\,I_m + K_f\,K_{ref})} \tag{4.37}$$

Even, we do not have any upper limits on controller gains this structure limits rendered stiffness at the end-effector. Increasing controller gains further does not change the rendered stiffness since it converges to the softest spring as seen in Fig. 4.8. For this case, it is limited by K_f to show that if stiff springs are desired to be rendered it is crucial to have a stiff SEA at the plant. Hence, compliant sensors will degrade performance in stiff virtual environments.

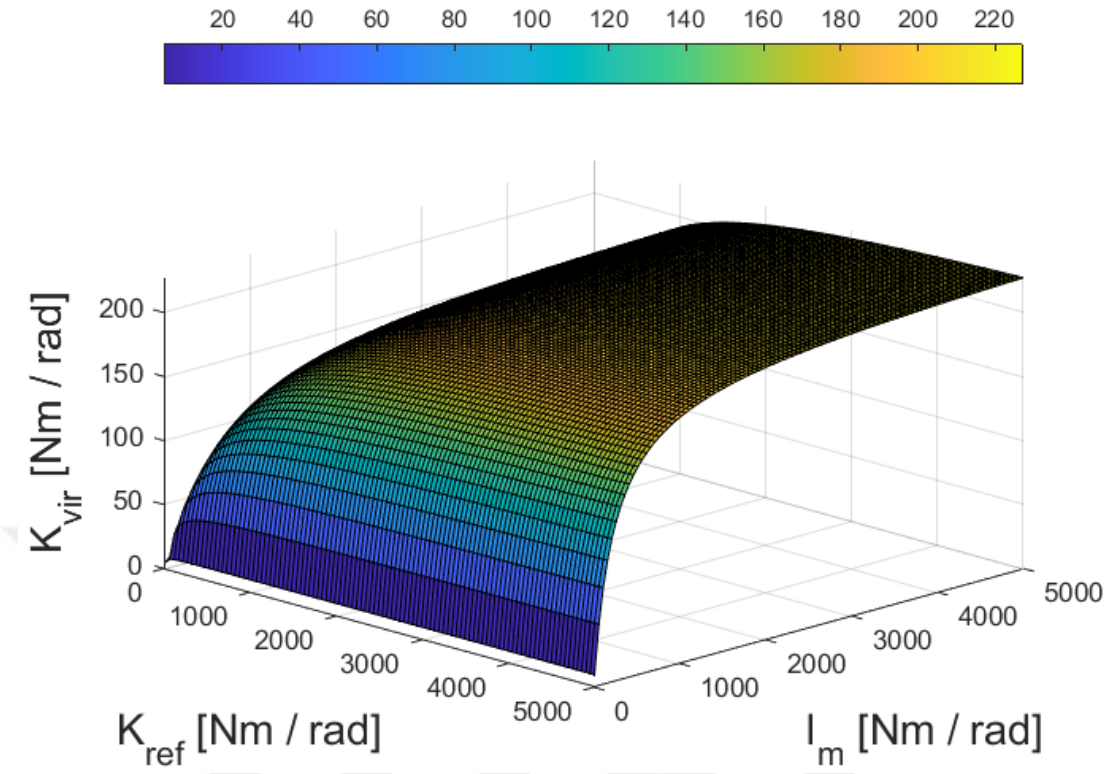

FIGURE 4.8: Effects of Controller Gains on Virtual Stifness

Furthermore, we set the reference virtual environment as pure spring but as seen in the realization parasitic damping, c_{1s}^{PI}, appears parallel to rendered stiffness, K_{vir}, in the low frequencies. The effect of this damping is detailed in Section 5.3. However, it is evident to see c_{1s}^{PI} increases with stiffer SEA since ${K_f}^2$ is a factor in the term. It results in a trade-off since stiff environment rendering requires a stiff force sensor which adds more damping to the system. Integral gain on motion controller can compensate for this effect. In the limit as $I_m \to \infty$, c_{1s}^{PI} converges to 0. Since high integral gains cause wind-up problems it is not feasible to have very large I_m. Moreover, the system will act like a pure spring for large I_m but it is prone to unwanted oscillations for such cases.

Since parasitic damping appears parallel to K_{vir}, the system actually renders a Voigt-Model. Moreover, to preserve causality desired admittance should be selected as $A_d = \frac{s\,\omega_f}{K_{ref}\,s + K_{ref}\,\omega_f}$. Furthermore, this actually represents the same desired admittance as Voigt-Model. Filtered spring to Voigt-Model mapping can be

done as in Eqn. (4.38), while $B_{ref} = K_{ref}/\omega_f$ and reference stiffness stays as it is.

$$\frac{s\,\omega_f}{K_{ref}\,s + K_{ref}\,\omega_f} = \frac{s}{(K_{ref}/\omega_f)\,s + K_{ref}} := \frac{s}{B_{ref}\,s + K_{ref}} \tag{4.38}$$

4.6 Voigt-Model Rendering

Adding virtual damping to the virtual environment changes desired admittance to $A_d = \frac{s}{B_{ref}\,s + K_{ref}}$. Impedance transfer function becomes $Z_{vm}^{PI}(s) =$

$$\frac{B_{ref}\,J_m\,K_f\,s^3 + (B_{ref}\,K_f\,\alpha + J_m\,K_{ref}\,K_f)\,s^2 + n_4\,s + I_m\,K_{ref}\,K_f}{B_{ref}\,J_m\,s^4 + (B_{ref}\,\alpha + J_m\,K_{ref})\,s^3 + n_5\,s^2 + (I_m K_{ref} + K_f(I_m + K_{ref}))\,s} \tag{4.39}$$

where $n_4 = B_{ref}\,I_m\,K_f + \alpha\,K_{ref}\,K_f$ and $n_5 = B_{ref}\,\beta + K_{ref}\,\alpha + G_m\,K_f$.

Proof.

1. $Z(s)$ has no poles in the right half plane: Using Lemma 3.2 gives following stability conditions,

   (i) $J_m B_{ref} \geq 0$

   (ii) $a_{vm_2} = \alpha\,B_{ref} + J_m\,K_{ref} \geq 0$

   (iii) $\xi_{vm} = a_{vm_2}\,(B_{ref}\,\beta + \alpha\,K_{ref} + G_m\,K_f) - B_{ref}\,J_m\,(I_m\,K_{ref} + I_m\,K_f + K_{ref}\,K_f) \geq 0$

2. $Re\{Z(j\omega)\} \geq 0$ for all $\omega \in (-\infty, \infty)$: The test polynomial is derived from Eqn. (4.39) as $R(j\omega) = a_0\omega^2 + a_1\omega^4$. This function can be interpreted as $R(j\omega) = (a_0 + a_1\omega^2)\cdot\omega^2$. According to Lemma 3.5, the condition is satisfied if and only if $a_0 = K_f^2\left(I_m\,(B_{ref}\,I_m + B_m\,K_{ref}) + {K_{ref}}^2\,\alpha\right) \geq 0$ and $a_1 = K_f^2\,(B_{ref}\,(B_{ref} + G_m)\,\alpha - I_m\,J_m\,B_{ref} + J_m\,K_{ref}\,G_m)$. Dividing both sides by K_f^2 gives the following conditions:

   (iv) $B_{ref}\,I_m\,J_m \leq G_m\,J_m\,K_{ref} + B_{ref}\,(B_{ref} + G_m)\,\alpha$

(v) $I_m\,(B_{ref}\,I_m + B_m\,K_{ref}) + {K_{ref}}^2\,\alpha \geq 0$

3. Any poles of Z(s) on the imaginary axis are simple with positive and real residues: our system only has one root on the imaginary axis where $s = 0$.

(vi) $Res\,Z(s) = \lim_{s\to 0} sZ(s) = \dfrac{I_m K_{ref} K_f}{I_m K_{ref} + K_f(I_m + K_{ref})} > 0$

□

Conditions (i) and (vi) are identical to those presented in the first section, as detailed in Section 4.3, and the sixth condition, outlined in Section 4.5, also requires that the controller gains be positive. Consequently, conditions (ii) and (v) are automatically satisfied.

You can expand the terms in condition (iii) and express them as a polynomial involving the system parameter K_f, which is known to be positive. The condition then takes the form $\xi_{vm}(K_f) = c_{vm_1}, K_f + c_{vm_2} \geq 0$, where $c_{vm_1} = (B_{ref} + G_m)(B_{ref}, \alpha + J_m K_{ref}) - B_{ref} J_m (I_m + K_{ref})$ and $c_{vm_2} = (\alpha, B_{ref} + J_m K_{ref})(B_{ref} I_m + \alpha, K_{ref})$.

The first coefficient, c_{vm_1}, can be further simplified to $-B_{ref} I_m J_m + G_m J_m K_{ref} + B_{ref}(B_{ref} + G_m)\,\alpha$, and the second coefficient, c_{vm_2}, can be simplified to $\alpha, ({B_{ref}}^2 I_m + J_m {K_{ref}}^2 + B_{ref} K_{ref}, \alpha)$. It's important to note that c_{vm_2} is always positive, as all the parameters involved are positive. Additionally, c_{vm_1} is equivalent to condition (iv), which must be positive to ensure passivity. When both coefficients are positive, $\xi_{vm}(K_f)$ is always positive, thus satisfying condition (iv) guarantees $\xi_{vm} \geq 0$. Moreover, condition (iv) is a relaxed version of condition (vi) presented in Section 4.3. This becomes evident when K_{ref} is set to 0 in condition (iv) during VM rendering. This condition implies that adding a virtual spring to the system relaxes the upper bound on I_m and enhances the low-frequency performance of the system. In Table 2 of [24], the VM passivity condition is given as $c_{vm} = c_b + c_k$, where $c_b = I_m \leq \frac{(G_m + B_{ref}), \alpha}{J_m}$ and $c_k = K_{ref} \geq 0$. This contradicts our analysis, as condition (iv) includes a factor of J_m, G_m in its expression for K_{ref}.

4.6.1 Passive Physical Equivalent

The passive physical equivalent of VM rendering, as defined by Eqn. (4.39), is presented in Table 4.2g. Similar to the spring rendering realization in Table 4.2e, controllers appear as a series spring to the physical spring. The other components are listed below:

$$
\begin{aligned}
k_{1vm}^{PI} &= \frac{{K_f}^2\,\gamma_3}{I_m\,K_{ref} + I_m\,K_f + K_{ref}\,K_f} \\
k_{2vm}^{PI} &= \frac{{K_f}^2\,d_3\,\gamma_3}{(B_{ref}+G_m)^3\,(I_m\,K_{ref} + I_m\,K_f + K_{ref}\,K_f)^2} \\
c_{1vm}^{PI} &= \frac{K_f^2\,\gamma_3^2(\alpha\,B_{ref}\,(B_{ref}+G_m) - J_m(I_m\,B_{ref} - K_{ref}\,G_m))}{(B_{ref}+G_m)^2(I_mK_{ref} + I_mK_f + K_{ref}K_f)^2} \\
c_{2vm}^{PI} &= \frac{{K_f}^2\,d_3}{(B_{ref}+G_m)^2\,(I_m\,K_{ref} + I_m\,K_f + K_{ref}\,K_f)^2} \\
b_{1vm}^{PI} &= \frac{B_{ref}\,J_m\,{K_f}^2\,{\gamma_3}^2}{(B_{ref}+G_m)\,(K_{ref}\,\beta + I_m\,K_f)^2}
\end{aligned}
$$

where $\gamma_3 = I_m + K_{ref}$, $d_3 = (B_{ref}\,I_m - G_m\,K_{ref})\,(J_m\,{\gamma_3}^2 - K_{ref}\ (B_{ref}+G_m)\ \alpha + I_m\ (B_{ref}-B_m)\ (B_{ref}+G_m))$.

Since all the spring constants are required to be non-negative for feasibility, this also implies that k_{1vm}^{PI} and γ_3 will be non-negative. Every term in c_{2vm}^{PI} is squared, leaving $d_3 \geq 0$ to ensure the entire term is non-negative. The term d_3 is non-negative when two of the multipliers have the same sign and the following conditions must be met:

$$(B_{ref}\,I_m - G_m\,K_{ref}) \lesseqgtr 0 \tag{4.40}$$

$$(J_m\,{\gamma_3}^2 - (B_{ref}+G_m)\ (K_{ref}\,\alpha + I_m\ (B_m - B_{ref})) \lesseqgtr 0 \tag{4.41}$$

Similarly, given that d_3 and γ_3 must be non-negative by requirement, k_{2vm}^{PI} will be positive when $(B_{ref} + G_m)^3 \rightarrow (B_{ref} + G_m) > 0$. The inerter term in the realization, b_{2vm}^{PI}, requires $\frac{B_{ref}}{B_{ref}+G_m}$ to be non-negative for feasibility. Since positivity of $B_{ref} + G_m$ is imposed by other components, this term only introduces a new condition which requires B_{ref} to be non-negative. Finally, c_{1vm}^{PI} is non-negative when the following equation is satisfied:

$$B_{ref}\,(B_{ref} + G_m)\,\alpha - J_m\,(I_m\,B_{ref} - K_{ref}\,G_m) \geq 0 \tag{4.42}$$

Notice that this equation can be rewritten in the form of a passivity condition (iv).

4.6.2 Passivity vs. Feasibility of Physical Realization

Similar to the passive physical equivalent of pure spring rendering, the realization of VM rendering has the same spring structure which covers non-negativeness of K_{ref}, I_m and K_f as necessary and sufficient condition of passivity. Non-negativeness of b_{2vm}^{PI} covers condition (i) which is $B_{ref} \geq 0$. Moreover, c_{1vm}^{PI} is guaranteed to be non-negative when passivity condition (iv) is satisfied.

In addition to these necessary and sufficient conditions, Eqn. (4.40)-(4.41) and $B_{ref} + G_m > 0$ introduce sufficient conditions for passivity where they must be met to have feasible realization.

4.6.3 Haptic Rendering Performance

Addition of virtual damping parallel to pure spring does not change rendered stiffness at the end-effector as seen in Table 4.2g and K_{vir} stays the same as in Eqn. (4.37). Moreover, rendered damping appears in the sub-branches series to k_{1vm}^{PI}. Rendered damping, B_{vir}, defined in Eqn. (4.43) is equivalent to combination of c_{1vm}^{PI} and c_{2vm}^{PI}. Since the damping term is dominant when the spring-damping

pair is connected in series. Hence, right most branch will introduce only c_{2vm}^{PI} in the low frequencies. One other thing, B_{vir} has two parts one part is directly affected by reference virtual damping, B_{ref}, and there is an independent part consisting of system parameters and controller gains. The second part appears in pure spring rendering as well and it is the same term as c_{1s}^{PI} given in Table 4.2f. This limits minimum passively rendered damping for us since negative reference is not allowed to compensate for this parasitic offset. These additional terms are due to the force sensor as discussed in Section 4.5.

$$B_{vir} = \frac{{I_m}^2 {K_f}^2}{\left(I_m K_{ref} + I_m K_f + K_{ref} K_f\right)^2} B_{ref} + \frac{{K_f}^2 \left(\alpha {K_{ref}}^2 + B_m I_m K_{ref}\right)}{\left(I_m K_{ref} + I_m K_f + K_{ref} K_f\right)^2} \tag{4.43}$$

The change in the virtual environment from pure spring to Voigt-model introduces advantages over haptic performance by compromising the passivity of the system. Passivity condition (iv) of Voigt-model rendering, puts a lower bound on K_{ref} and an upper bound on I_m. These bounds limits rendered stiffness, K_{vir}, at the end-effector since these terms are springs connected in series. One will limit how soft your reference admittance must be while the other limits how stiff your motion controller can be. The advantage is that it have control over damping in the system through B_{ref}. Thus, unwanted oscillations while rendering soft springs can be compensated by adding more damping to the system virtually. This presents a trade-off between performance and spring rendering performance in the Voigt-model rendering.

On the other side, same passivity condition is relaxed by having a virtual spring compared to pure damping rendering. Relaxed upper bound on I_m can be used to improve the performance of the system without adding more damping to the system. Similarly, it also relaxes condition on B_{ref} as lower virtual damping references are allowed due to the addition of this virtual spring. However, now the virtual damping is only felt at mid-band and

We can express passivity condition (iv) as given in the Eqn. (4.44). Notice that,

now the mechanical time constant of the controlled plant is multiplied by a factor of $(1 - \frac{K_{ref}/B_{ref}}{I_m/G_m})$ and compared with the time constant of the damping controller. The factor can be interpreted as a distance between the stiffness of the virtual environment and versus stiffness of the motion controller. As we render similar or more stiffer environments than the motion controller, the passivity condition is satisfied. Hence, if we render softer environments we have to compromise from the performance by selecting slower controllers.

$$\frac{B_{ref} + G_m}{I_m} \geq \frac{J_m}{\alpha}\left(1 - \frac{K_{ref}/B_{ref}}{I_m/G_m}\right) \tag{4.44}$$

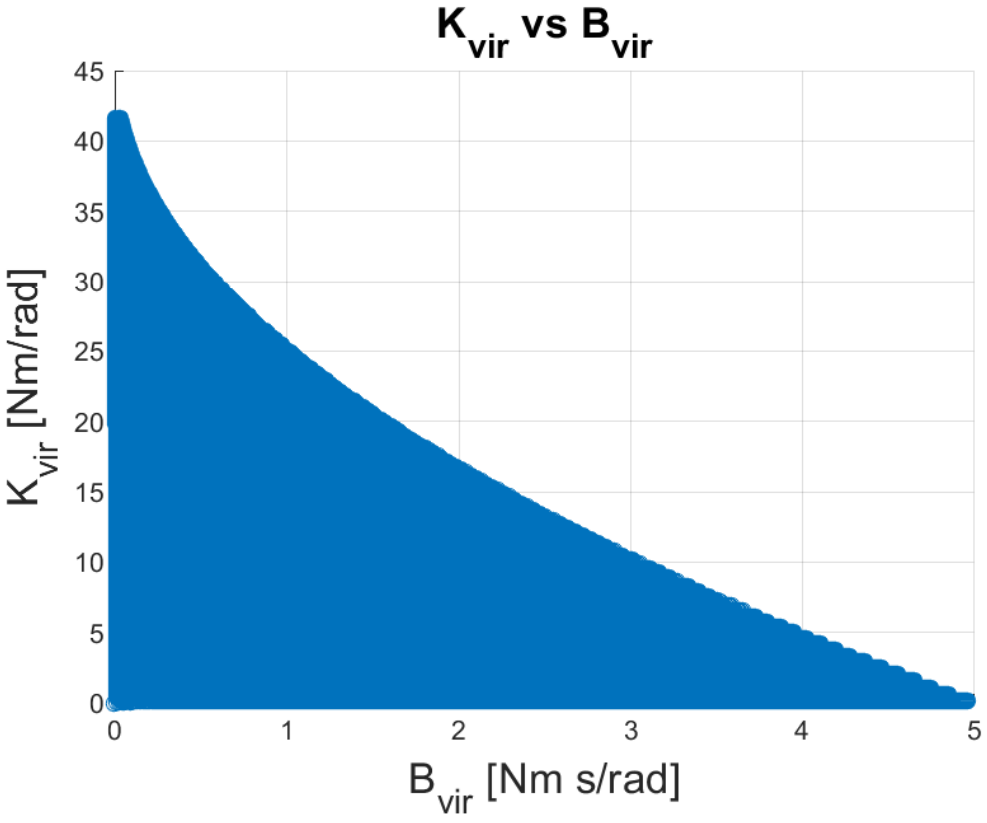

FIGURE 4.9: K/B Plot for VM Rendering with SEA under BAC

Lastly, we analyze K_{vir} and B_{vir} with respect to each other where passivity condition (iv) is imposed to those to show passively renderable K/B range. We search a parameter space where both I_m and K_{ref} swept through 0 to 500 [Nm/rad] and B_{ref} from 0 to 5 [Nm s/rad] which satisfy passivity condition (iv) as it would give

valid solutions for our K/B plot. G_m is set as 0.0576 [Nm s/rad] and the transmission ratio is taken as 1 and K_f as 50 [Nm/rad] for simplicity. Other parameters are used as given in Table 4.1. As it is seen in Fig. 4.9 K_{vir} will saturate around the softest spring and stiff springs cannot be rendered passively as B_{vir} increases. Thus, stiff springs require less or no damping in the system.

Chapter 5

Effective Impedance Analysis

5.1 Pure Mass Rendering

G_m introduces additional damping into the system, evident in the representation as c_{1m}^P in Table 4.2b, and substantiated by the effective damping analysis presented in Fig. 5.1.

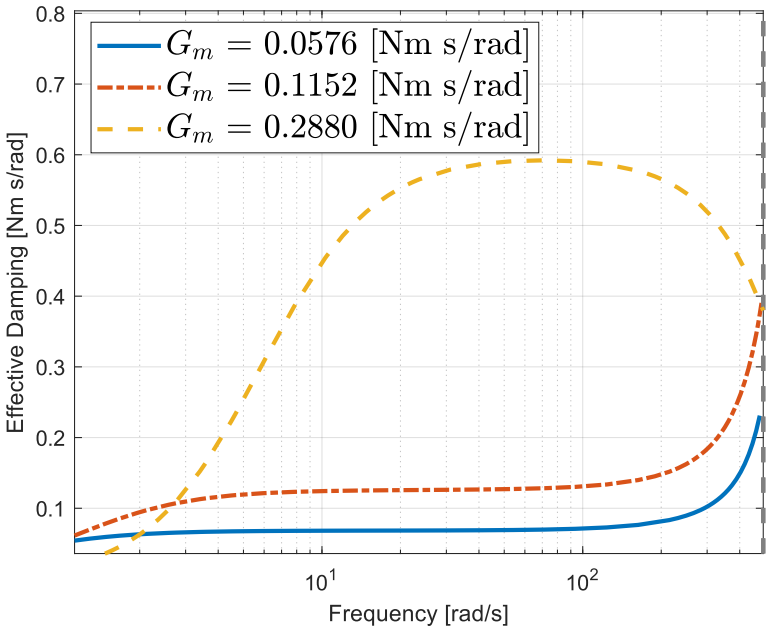

FIGURE 5.1: Proportional Motion Controller Gain Effect on Effective Damping while Pure Mass Rendering

5.2 Pure Damping Rendering

The passivity region is constrained by the integral motion gain, necessitating larger values of B_{ref} with increasing levels of I_m, as evidenced in Eqn. (4.22). Furthermore, increasing I_m proves beneficial for system performance, as it diminishes the impact of parasitic inertia that appears parallel to rendered damping in Table 4.2d, as defined in Eqn. (4.20). The influence of I_m on effective inertia is depicted in Fig. 5.2.

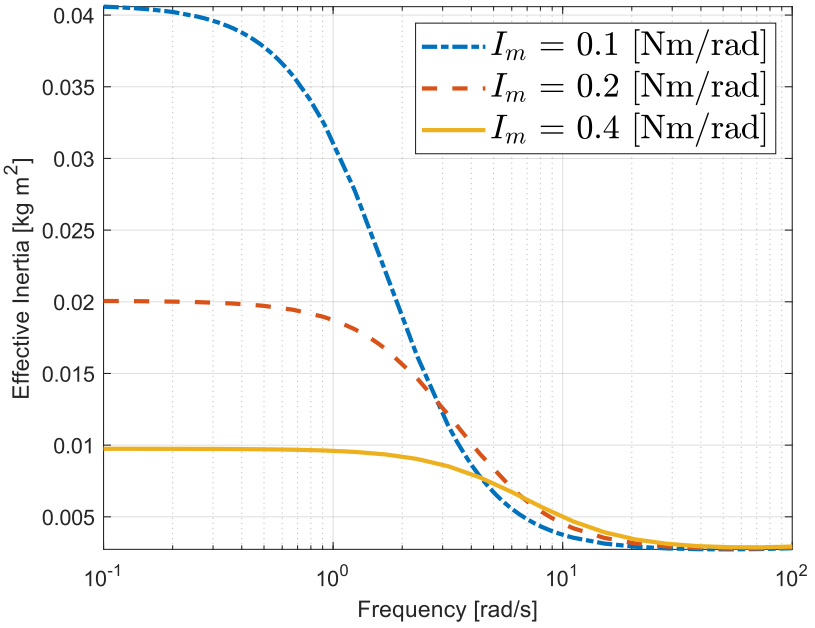

FIGURE 5.2: Integral Motion Controller Gain Effect on Effective Inertia while Pure Damping Rendering

5.3 Pure Spring Rendering

The analysis of effective impedance has revealed the effects of parasitic damping in the low-frequency range, attributed to force sensor compliance, as illustrated in Fig. (5.3). This parasitic damping is also evident in the form of c_{1s}^{PI} and runs in parallel with $Kvir$ in Table 4.2f. It is evident that the impact intensifies with increased sensor compliance, thereby imposing constraints on achieving stiff spring rendering.

Furthermore, this analysis substantiates our earlier discussion that achieving Pure Spring Rendering is unattainable. Instead, the Voigt-Model gives as a more accurate representation in haptic rendering analysis, as defined in the mapping given in Eqn. (4.38).

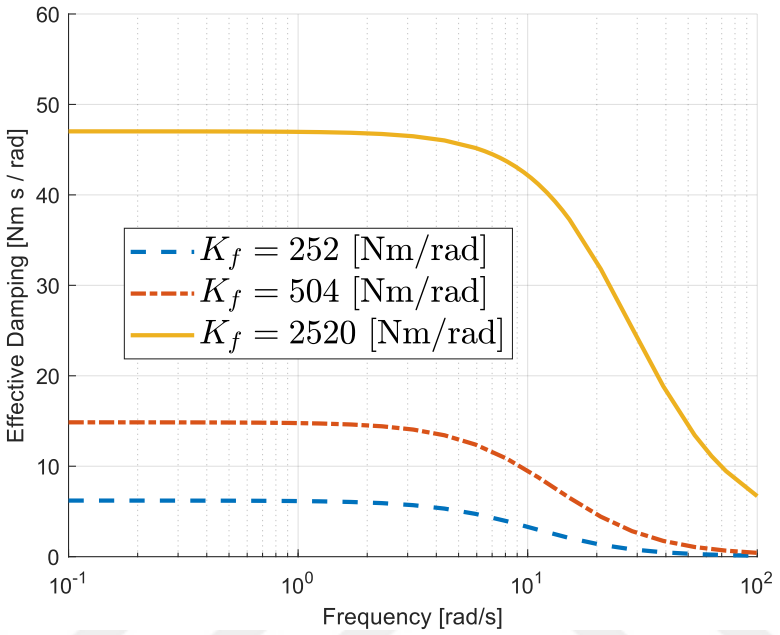

FIGURE 5.3: Force Sensor Stiffness Effect on Effective Damping while Pure Spring Rendering

5.4 Voigt-Model Rendering

Eqn. (4.43) illustrates the rendered damping at low frequencies, as previously discussed. Additionally, the terms c_{1vn}^{PI} and c_{2vm}^{PI} collectively contribute to the rendered damping, denoted as B_{vir}. The parasitic component of damping within B_{vir} can be compensated by increasing I_m, as visualized in Fig. 5.4. However, it is important to note that an increase in I_m leads to reduced passivity regions concerning B_{vir} and limits the passively renderable of K/B pairs to those resembling stiff springs with minimal virtual damping as in Fig. 4.9.

This limitation on passivity can be improved by raising the reference stiffness K_d, although this comes at the expense of compromising the quality of damping

rendering. Opting for stiffer spring references causes the desired admittance to converge more towards a pure spring response, thereby allowing parasitic damping to persist.

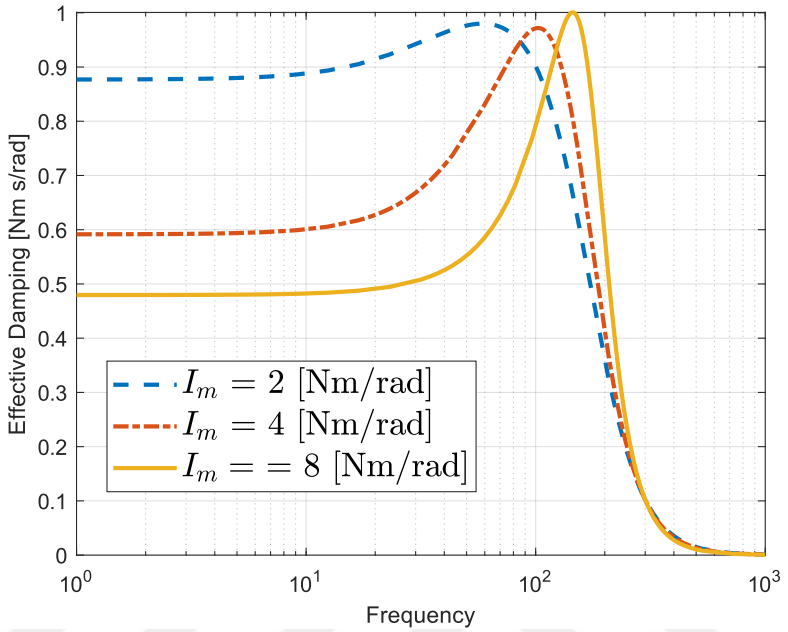

FIGURE 5.4: Integral Motion Controller Gain Effect on Effective Damping while Voigt-Model Rendering

Chapter 6

Experimental Validation

In this section, we present the experimental validation of our theoretical analysis, focusing on both the passivity bounds and haptic rendering fidelity within various virtual environments for a Series Elastic Actuation (SEA) under the Basic Admittance Controller (BAC). For our experiments, we utilize a single degree of freedom SEA brake pedal based on the design proposed in [37], with certain modifications.

The system is actuated by a brushless DC motor equipped with a Hall-effect sensor, operating at 1 kHz and controlled using the EPOS/Beckhoff framework via EtherCAT channels. To enhance the power output of the motor, we introduce a gearbox and capstan transmission with transmission ratios of 1:10 and 1:3.95, respectively. Compliance at the end-effector is achieved through cross-flexures implemented after the transmission unit. This cross-flexure is instrumented with a linear encoder to measure deflections at the spring, enabling the estimation of interaction forces and torques at the end-effector.

Table 6.1: Parameter Mapping for Experiments

Parameters	**Effective Parameter**
J_m	$J_{\text{eff}} = J_m \cdot n^2$
B_m	$B_{\text{eff}} = B_m \cdot n^2$
K_f	$K_{\text{eff}} = K_f$
G_m	$G_{\text{eff}} = G_m \cdot n^2$
I_m	$I_{\text{eff}} = I_m \cdot n^2$
A_d	$A_{\text{eff}} = A_d \cdot n$

6.1 Identification of System Parameters

The SEA brake pedal system is initially configured following the specifications outlined in [37]. However, to ensure the precision of our experiments, we employ system identification methods to accurately determine plant parameters. Utilizing a PI motion controller, as illustrated in Fig. 3.4, with predefined motion controller gains ($G_m = 0.0576$ [Nm s/rad] and $I_m = 1$ [Nm /rad]), enables us to leverage the System Identification Toolbox in MATLAB. Given the known closed-loop transfer function described in Eqn. (3.10) and the motion controller gains, we employ grey-box modeling methods to deduce system parameters.

In our initial experiment, a chirp signal with unit magnitude and a frequency range of 0.01 to 10 Hz is applied as a reference to capture both the low and high-level dynamics of the plant. The resulting output data is recorded and fitted using transfer function identification methods. The identified plant parameters are presented in Table 6.2 with an R^2 value of 95%.

For stiffness characterization, predetermined torques/forces are applied at the end-effector when $\omega_m = 0$, and deflections are measured by a linear encoder and recorded. The linear spring stiffness is determined to be 252 [Nm/rad] with an R^2 value of 99%.

It is essential to note that, for both system identification and experimental validation, the parameter mapping given in 6.1 must be applied through the transmission ratio.

Table 6.2: Identified System Parameters

Parameters	**Value**	**Unit**
J_m	5.21 x 10^{-4}	kg·m^2
B_m	1.11 x 10^{-2}	N·m·s/rad
K_f	252	N·m/rad
Gear Ratio	1:38.1	

6.2 Validation of Passivity Bounds

We conduct a series of experiments to validate the passivity bounds outlined in Section 4 via coupled stability experiments. The passivity bounds are verified by assessing coupled stability within the system following externally applied impacts to excite the system across various frequency ranges. Each haptic rendering scenario is associated with its most challenging environment, specifically the most destabilizing conditions, as proposed in [12]. This approach is adopted to demonstrate that the system remains passive even under the most adverse circumstances. In mass rendering, the end-effector is coupled to a highly stiff spring to replicate the worst-case environment, while in spring rendering, the addition of physical mass to the end-effector is necessary. Coupled stability is considered violated when indicators such as chatter, escalating oscillations, or unbounded outputs are observed. Conversely, the absence of movement, the presence of decaying oscillations, or the fading out of chatter during a series of impacts indicates that coupled stability is not violated.

6.2.1 Pure Mass Rendering - P Motion Controller

Initially, a series of experiments are conducted to validate the passivity bounds presented in Section 4.1 for the system defined in Eqn. (4.2), denoted as $Z^{P}_{mass}(s)$. Given that the system is reduced to a P motion controller, the necessary and sufficient condition for the passivity of pure mass rendering with SEA under BAC is governed by condition (vii). As discussed previously, this condition entails a trade-off between the passivity region and bandwidth. As depicted in Fig. 6.1b, an increase in the motion controller gain (G_m) results of a higher passivity bound on M_{ref}, thereby reducing the region for passivity. The dashed curve represents the passivity bound on M_{ref}, with empty circles denoting instances where coupled stability is observed, and crosses representing points where coupled stability is not observed. In Fig. 6.1a, the same set of experiments is presented using a different definition. By defining the rendered mass in Eqn. (4.4), we illustrate

that, even with an improved controller, we cannot change the passively renderable minimum mass, which corresponds to the system's inertia, J_m. The experiments exhibit errors of 8% and 6.8% for instances where coupled stability is observed and not observed, respectively. These errors arise from unmodeled effects within the system, including non-linearities, compliance of rigid bodies, and dissipation due to friction. However, our experimental results align with the theoretical analysis conducted, affirming the agreement between theory and practical observations.

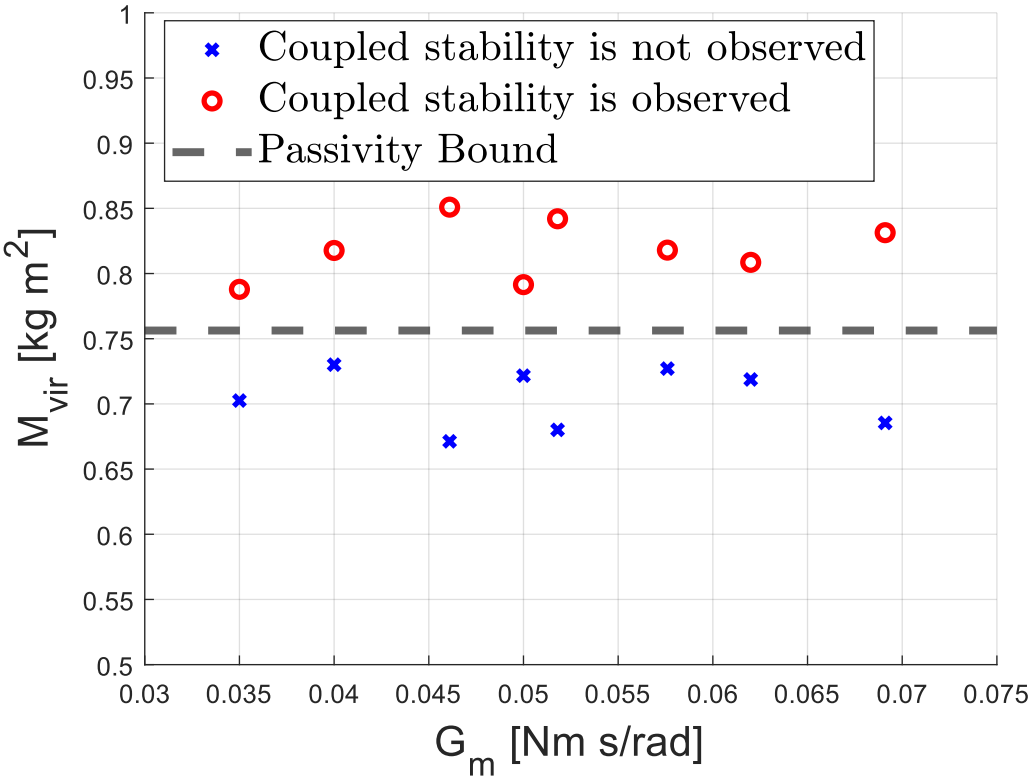

(a) Passivity Bound on M_{vir}

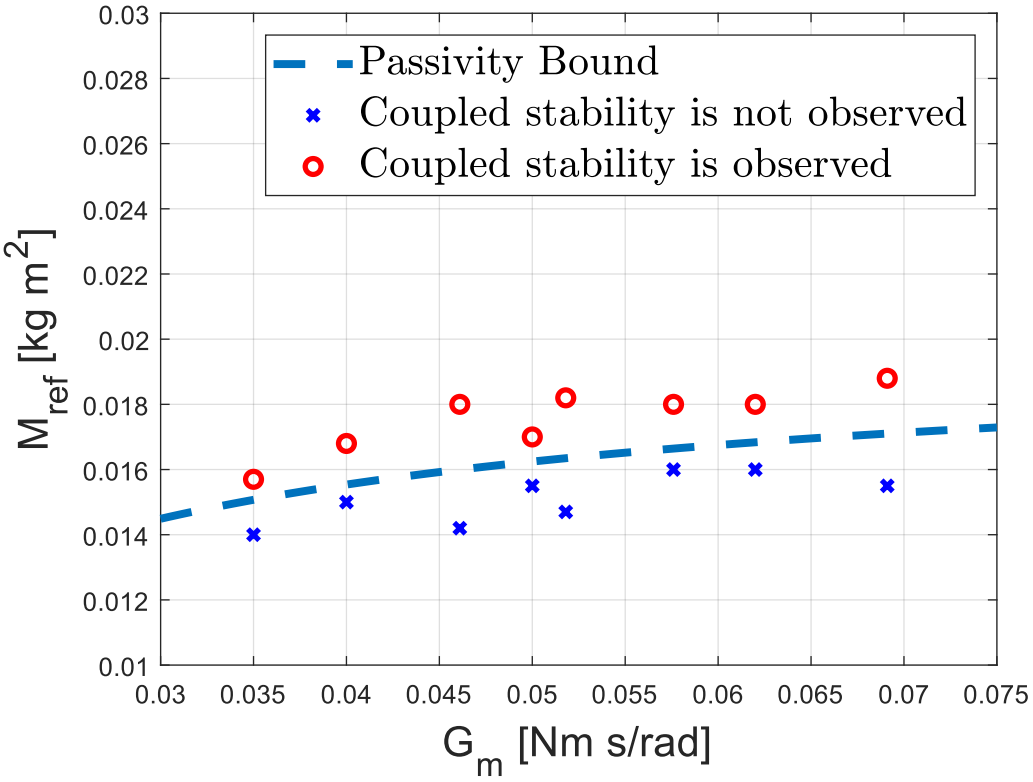

(b) Passivity Bound on M_{ref}

FIGURE 6.1: Coupled Stability Experiments for Pure Mass Rendering with P Motion Controller

6.2.2 Pure Damping Rendering - PI Motion Controller

The discussion in Section 4.3 for the system defined with $Z^{PI}_{damping}(s)$ in Eqn. (4.15) concludes that passivity condition (vi) is the only necessary and sufficient condition, besides selecting I_m as non-negative due to condition (iii). As mentioned earlier, this presents a trade-off between the performance of the system at lower frequencies and haptic rendering fidelity. Since B_{ref} is equivalent to the rendered damping, B_{vir}, it is necessary to add more damping to the virtual environment to improve performance. This establishes a linear relationship between two parameters, as evident in the condition. A set of experiments is conducted to verify this relationship between motion controller gain and the desired virtual environment.

The experimental verification of this relationship yields an average error of 5.4% for instances where coupled stability is observed and 1.6% for instances where it is not observed. Fig. 6.2 illustrates the experiment instances where G_m is set to 0.025 [Nm s/rad]. The dashed curve represents the passivity bound on I_m, with empty circles denoting instances where coupled stability is not violated, and crosses representing points where coupled stability is violated. The reason for setting motion controller gain so low is to maintain a high bandwidth of damping rendering, as demonstrated by their inversely proportional relationship in Fig. 4.5. After the transmission effective parameters are still high due to mapping in Table 6.1. Once more, our results confirm the theoretical analysis done in Section 4.3.

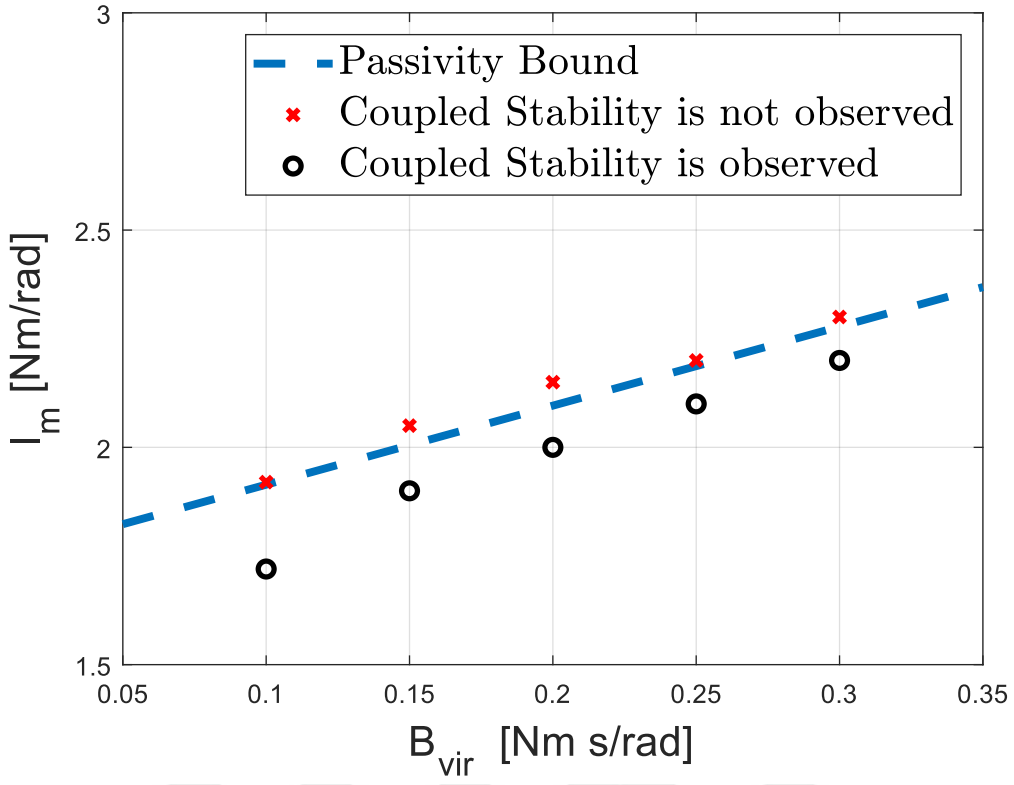

FIGURE 6.2: Coupled Stability Experiments for Pure Damping Rendering with PI Motion Controller

6.2.3 Pure Spring Rendering - PI Motion Controller

As discussed in Section 4.5, it is necessary and sufficient to have positive controller gains to ensure the passivity of pure spring rendering. Thus, we do not provide any experiments to verify this. The reason is that negative controller gains may harm the physical system we have. We provide performance experiments for pure spring rendering such as stiffness characterization and haptic rendering fidelity.

6.2.4 Mass-Damping Rendering - PI Motion Controller

In this series of experiments, we demonstrate the effectiveness of adding virtual damping to the desired admittance, enabling us to use of integral gain in the motion controller. Passivity condition (vii) is experimentally verified for two different parameters, as depicted in 6.4a-b. The experiments are conducted under

the worst-case scenario, where the minimum mass reference for the system is given by $M_d^{min} = \frac{J_m G_m}{\alpha}$, with G_m set to 0.0864 [Nm s/rad]. It's important to note that, for experimental purposes, one can adjust this reference within a 10% range of the bound, as rendering minimum mass proves to be challenging for admittance controllers.

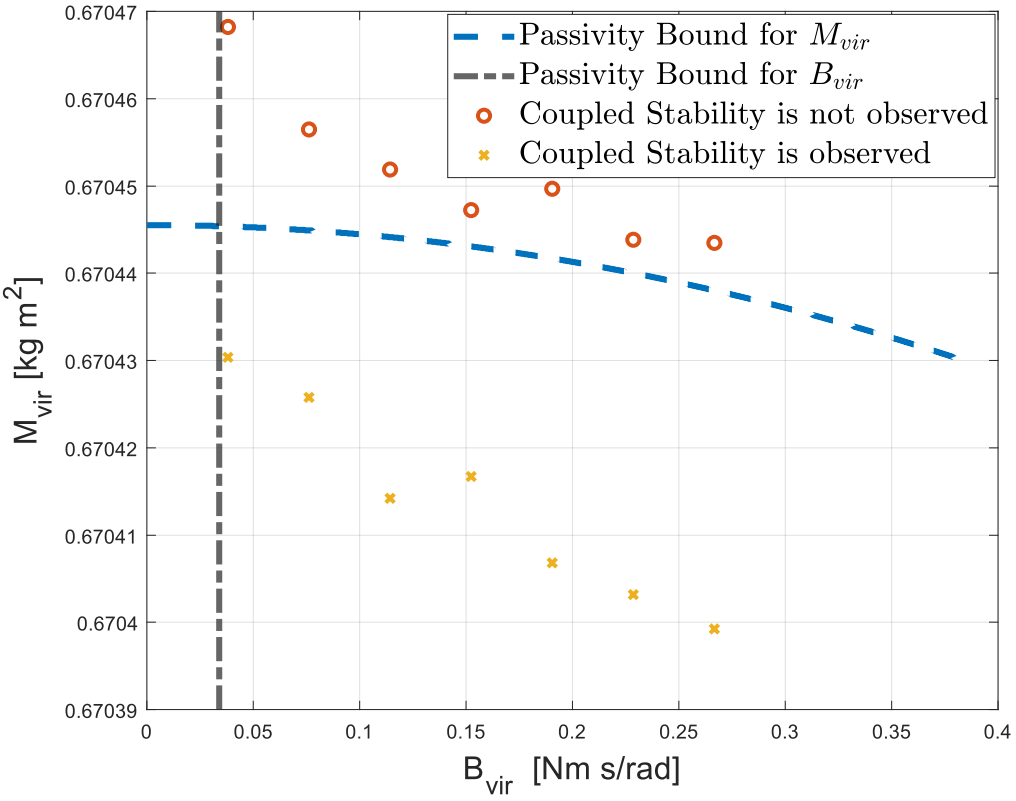

FIGURE 6.3: Experimental Verification of M/B Plot

As illustrated in Fig. 6.4a, a nearly linear relationship exists between I_m and B_{ref}, as expressed in Eqn. (4.24), given that B_{ref} has a relative order of 1 in the inequality. For this relation, the experiments show a 7.38% error when coupled stability is observed and a 6.58% error when coupled stability is not observed. Another set of experiments validates the quadratic relationship between G_m and I_m, as described in Eqn. (4.24). Similarly, experiments for this relation exhibit a 6.8% error when coupled stability is observed and an 8.2% error when coupled stability is not observed.

As a final note, we map the data obtained from the initial set of experiments (depicted in Fig. 6.4a) to Eqn. (4.29)-(4.30) to generate the M/B plot, as shown in Fig. 6.3. It's crucial to highlight that the violation of passivity bound (vii) specified in Eqn. (4.24) is also reflected in the rendered inertia. Thus, without the need for additional experiments, we demonstrate that compensating for more mass inevitably leads to a violation of passivity.

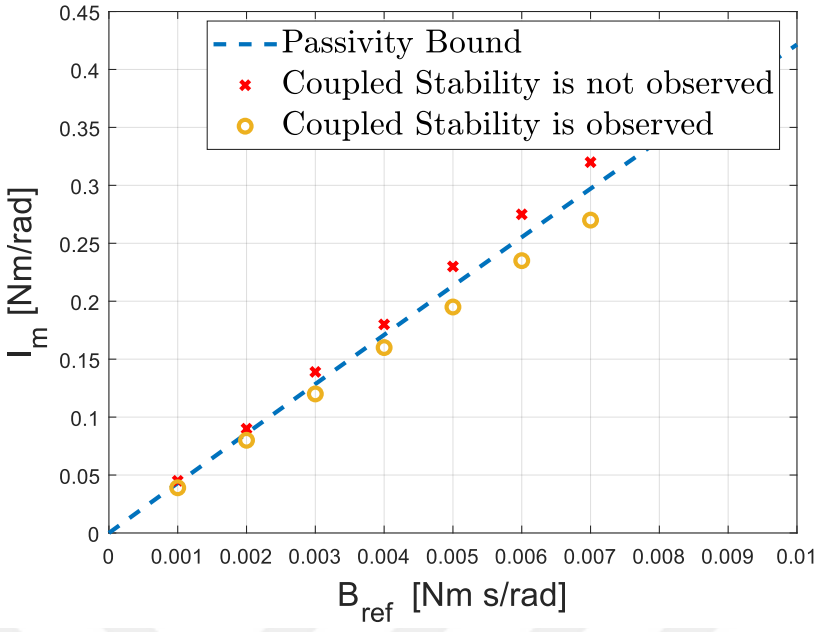

(a)

Experimental Verification of Passivity Condition (vii) (B_{ref} vs. I_m), Eqn. (4.24)

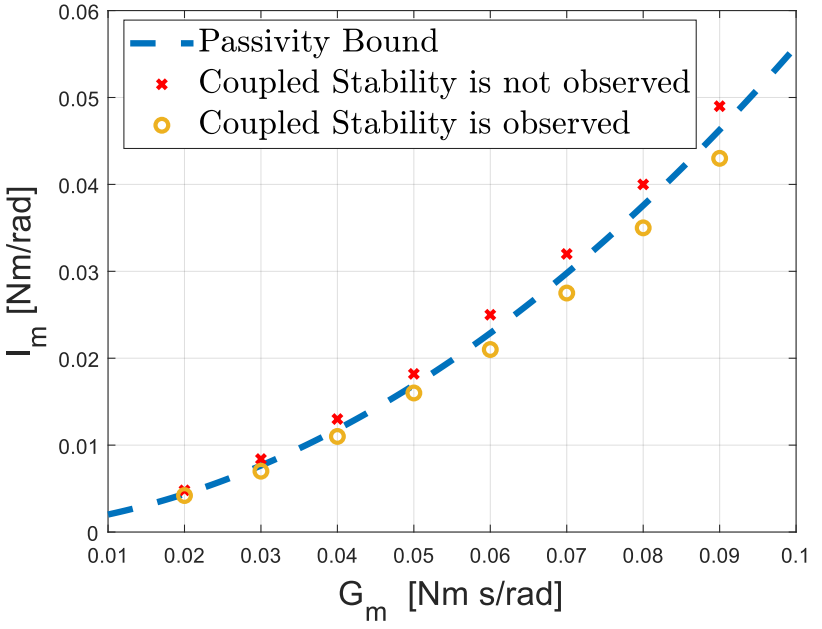

(b)

Experimental Verification of Passivity Condition (vii) (G_m vs. I_m), Eqn. (4.24)

FIGURE 6.4: Coupled Stability Experiments for Mass-Damping Rendering with PI Motion Controller

6.2.5 Voigt-model Rendering - PI Motion Controller

In this section, we present a series of experiments to validate the passivity conditions for the Voigt-model rendering with a PI motion controller. The Voigt-model, defined by $Z^{PI}_{Voigt}(s)$ in Eqn. (4.39), introduces a relaxation of passivity condition (iv) compared to the condition for pure damping rendering, as given in Eqn. (4.21). This relaxation occurs through the addition of a virtual spring to the virtual environment, resulting in a higher upper bound on the integral motion gain.

As depicted in Fig. 6.5, we set B_{ref} to 0.05 [Nm s/rad] in the experiments. The results show an average error of 3.2% when coupled stability is observed and 7.2% when coupled stability is not observed. These errors provide insights into the system's behavior under different conditions and highlight the practical challenges associated with maintaining coupled stability. It is important to note that the introduced virtual spring in the Voigt-model rendering allows for a more flexible adjustment of integral motion gain, offering a higher upper bound for optimal system performance.

These experiments not only validate the theoretical relaxation of passivity conditions but also affirm the trade-off between stability and performance in Voigt-model rendering.

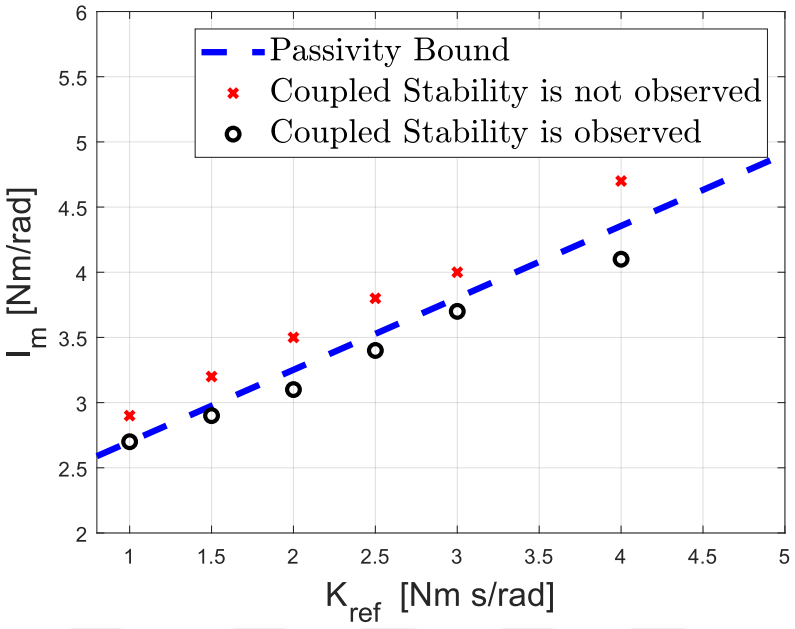

FIGURE 6.5: Coupled Stability Experiments for Voigt-model Rendering with PI Motion Controller

6.3 Validation of Haptic Rendering Fidelity

In this set of experiments, we have demonstrated the capability to render desired virtual environments within specific frequency ranges, particularly for lower frequencies. The bandwidth limitations observed are inherent to the physical dynamics of the system and may vary from one system to another. However, it is important to note that these variations do not alter the highlighted results presented in the analysis section.

Experiments assessing haptic rendering fidelity involve coupling the system to another brushless DC motor. The controllers of the second motor are fine-tuned when it is linked to the SEA brake pedal through the EPOS framework. No high-level controllers are implemented beyond the tuned low-level motion controllers of the system. This decision is made to avoid introducing additional dynamics through high-level controllers, aiming to mimic an ideal motion source input for the interaction port of the SEA brake pedal.

6.3.1 Pure Damping Rendering - PI Motion Controller

We validate the haptic rendering fidelity of Pure Damping Rendering with a SEA under BAC, as illustrated in Fig. 6.6. Samples are collected within the frequency range [1.5 26] rad/s for nine different instances, yielding an average error of 3.7%. For the experimentation, we render $B_{vir} = 3.81$ [Nm s/rad], equivalent to 11.61 in dB scale. The figure also indicates that this rendered damping is significantly lower than the system's inherent damping, $B_m = 16.11$ [Nm s/rad], which is 24.15 in dB. Hence, we experimentally verify the damping compensation discussed in Section 4.3 and illustrated in Fig. 4.4. Controller gains are set to $G_m = 0.05$ [Nm s/rad] and $I_m = 2$ [Nm/rad] during the experiment.

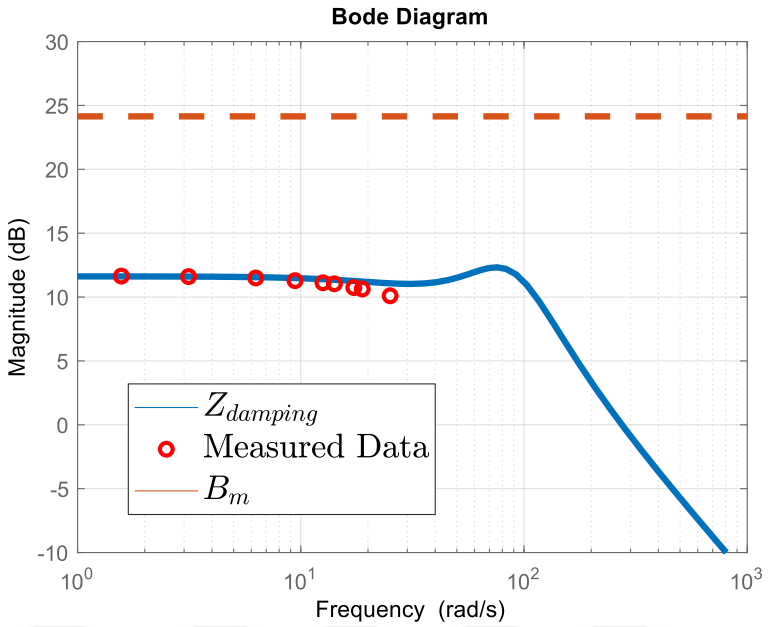

FIGURE 6.6: Haptic Rendering Experiments for Pure Damping Rendering PI Motion Controller

6.3.2 Mass-Damping Rendering - PI Motion Controller

We verify the haptic rendering fidelity of Mass-Damping Rendering with a SEA under BAC, as depicted in Fig. 6.7. The objective is to illustrate that at low frequencies, damping is rendered, and there is a midband transition to mass rendering. We sample the system at eight different frequencies ranging from [0.1 6] rad/s, achieving an average error of 8.6%. The rendered virtual mass and damping values during the experiment are $M_{vir} = 0.77$ [kg m^2] and $B_{vir} = 0.381$ [Nm s/rad], respectively, while the controllers are set to $G_m = 0.0864$ [Nm s/rad] and $I_m = 0.05$ [Nm / rad]. Due to the inherent dynamics of the system, we could not experiment at higher frequencies due to the transition to the physical dynamics of the system from the virtual environment. At these frequencies, the system resonates at its natural frequency.

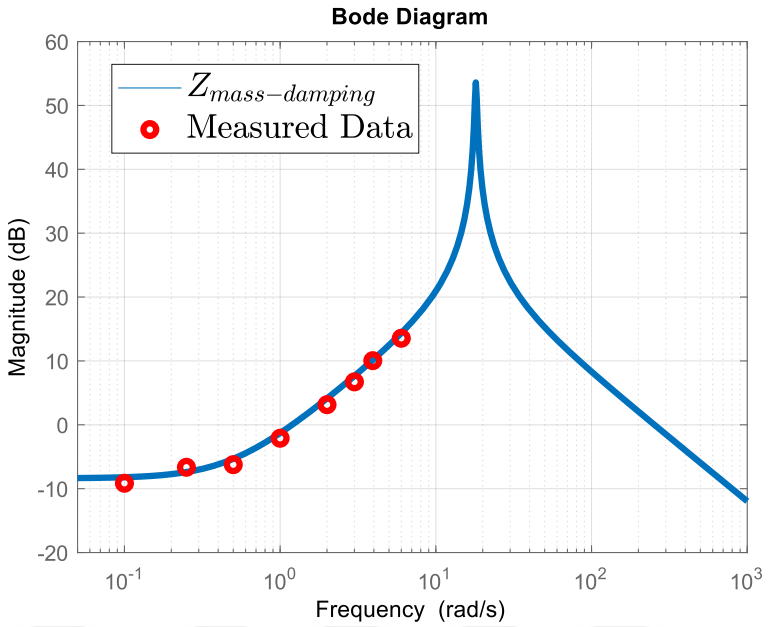

FIGURE 6.7: Haptic Rendering Experiments for Mass-Damping Rendering PI Motion Controller

6.3.3 Pure Spring Rendering - P Position Controller

In this set of experiments, we conduct stiffness characterization experiments for Pure Spring Rendering with a position-level controller for a SEA under BAC. Initially, due to the causality violation introduced by $A_d = s/K_{ref}$ for Pure Spring Rendering, a position-level controller is implemented at the inner loop. However, with the end-effector equipped with a velocity sensor, the time rate of change of torques/forces becomes available, allowing the implementation of $A_d = 1/K_{ref}$. The free s term is transferred to the previous signal τ_{sea} in Fig. 3.2 and is converted to $\dot{\tau}_{sea}$. It's worth noting that the proportional gain in the position level is equivalent to the integral gain in the motion level, and for consistency, we maintain the notation as implemented in the motion level.

Predetermined forces and torques are applied to the end-effector, and the deflections in the SEA element are measured. These measurements, combined with the position change in the motor, result in scattered points fitted into lines, as shown in Fig. 6.8. Two different springs, $K_{vir} = 142.8$ [Nm/rad] and $K_{vir} = 53.15$

[Nm/rad], are rendered (solid and dashed lines, respectively). The system is sampled for seven different forces, and the results yield an R^2 value of 0.95. This experiment confirms our ability to render the stiffness values proposed in Section 4.5.

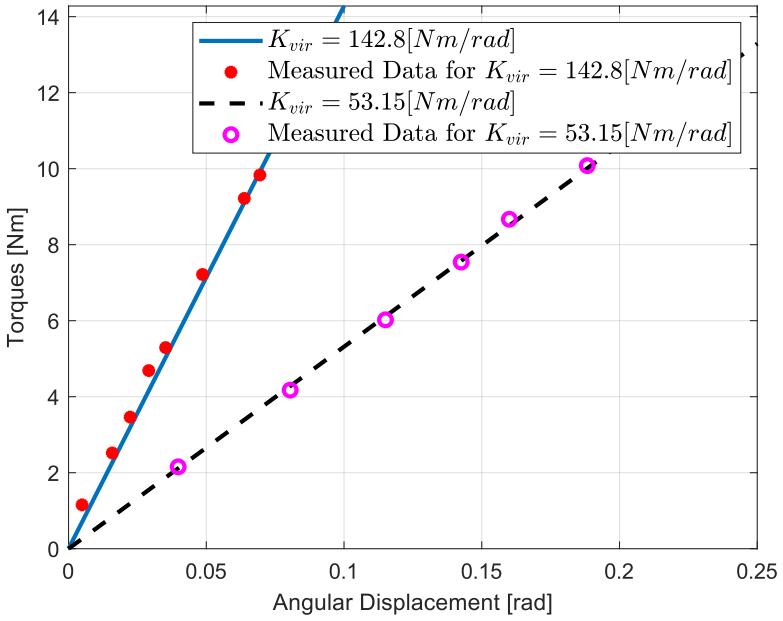

FIGURE 6.8: Stiffness Characterization Experiments for Pure Spring Rendering P Position Controller

6.3.4 Voigt-model Rendering - PI Motion Controller

Finally, we present haptic rendering fidelity experiments for Voigt-model with a PI Motion Controller for a SEA under BAC. This aims to showcase both the damping and spring rendering performance of the system. As anticipated, the system behaves like a pure spring at low frequencies and converges to rendered damping at the mid-band.

Fig. 6.9 illustrates our results, where the system is sampled at fourteen different frequencies ranging from [1 32] rad/s, resulting in a 6.2% average error for these points. We render $K_{vir} = 26.7$ [Nm/rad] and $B_{vir} = 3.2$ [Nm s/rad]. The controller gains are set to $B_{ref} = 0.1$ [Nm s/rad], $K_{ref} = 0.8$ [Nm /rad], $G_m = 0.0576$ [Nm s/rad], and $I_m = 1$ [Nm /rad].

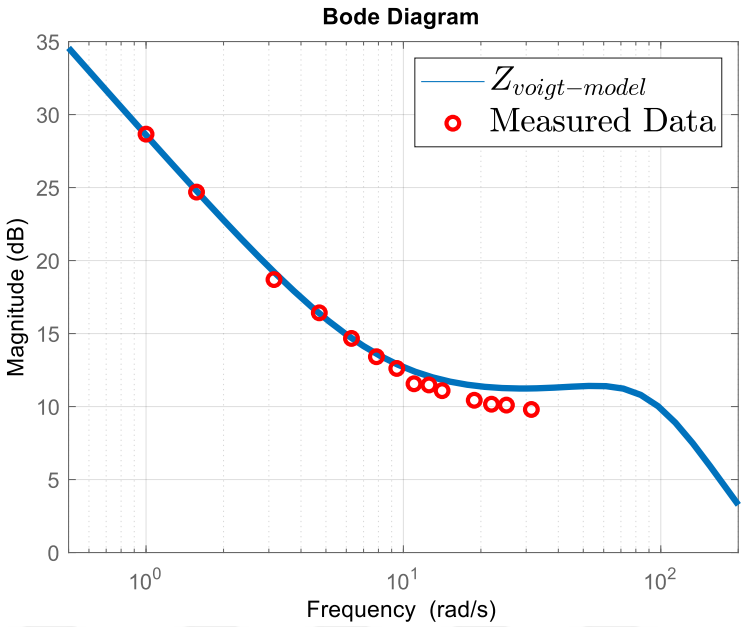

FIGURE 6.9: Haptic Rendering Experiments for Voigt-model Rendering PI Motion Controller

Chapter 7

Inertia Compensation with Feed-Forward Control Action

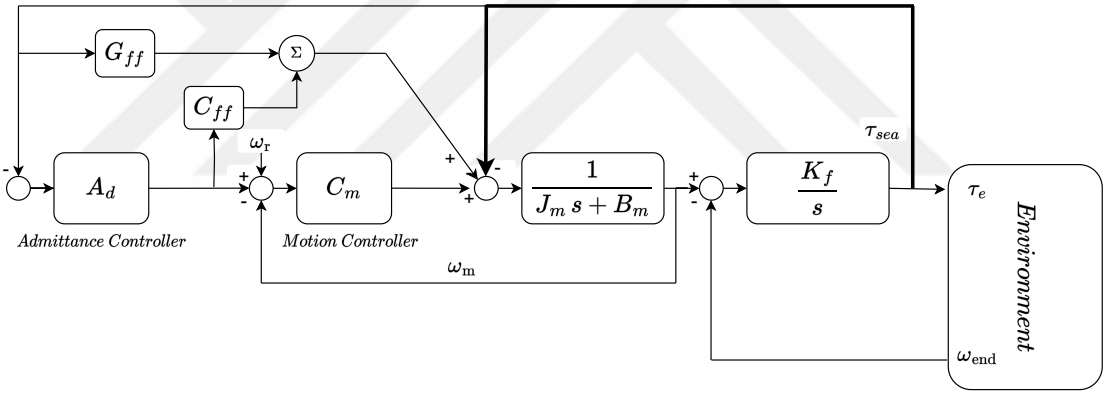

FIGURE 7.1: BAC block diagram with feed-forward controllers

In this section, we examine the effects of feed-forward controllers on the passivity and performance of mass rendering. Hart and Niemeyer [17] have proven that no causal controllers can compensate for the mass present in the system. Keemink *et al.* have presented that the system's inertia can be compensated for when controllers are selected as $G_{ff} > 0$ and $C_{ff} = \mu_{ff}\, s + \beta_{ff}$ [24]. Here, G_{ff} is a positive proportional gain on force feedback, while μ_{ff} and β_{ff} represent mass and damping compensation factors. However, it's important to note that this implementation is not causal and does not contradict the results in [17]. We

extend their analysis by addressing causality and the bandwidth limitations of controllers.

First, we look at the case where causal differentiator is used in C_{ff} and the controller becomes:

$$C_{ff} = \mu_{ff} \frac{s\,\omega_f}{s + \omega_f} + \beta_{ff} \tag{7.1}$$

7.1 Causality of Differentiation

Desired admittance, A_d, is kept as $\frac{1}{M_{ref}\,s}$ and for simplicity we take motion controller, $C_m = G_m$, as proportional controller. Impedance transfer function seen from the end-effector becomes $Z^P_{mass-ff}(s) =$

$$\frac{J_m\,K_f\,M_{ref}\,s^3 + (\alpha + J_m\,\omega_f)\,K_f\,M_{ref}\,s^2 + \alpha\,K_f\,M_{ref}\,\omega_f\,s}{J_m\,M_{ref}\,s^4 + (\alpha + J_m\,\omega_f)\;M_{ref}\,s^3 + n_6\,s^2 + n_7\,s + (G_m + \beta_{ff})\,K_f\,\omega_f} \tag{7.2}$$

where

$n_6 = (K_f(1 + G_{ff}) + \alpha\,\omega_f)\;M_{ref}$ and $n_7 = K_f\;(\beta_{ff} + G_m + \mu_{ff}\,\omega_f + M_{ref}\,\omega_f\,(1 + G_{ff}))$.

The rendered mass at the end-effector is derived as follows, from the low-frequency behavior of the system in Eqn. (7.2):

$$M_{vir} = \frac{M_{ref}\,\alpha}{G_m + \beta_{ff}} \tag{7.3}$$

Necessary and sufficient conditions for the system described in Eqn. (7.2) are derived according to Theorem 3.1. The conditions regarding the rendered mass, M_{vir}, are argued and presented. Theorem 3.1.2 yields the following conditions on M_{vir}:

$$\frac{J_m}{G_{ff}+1} - \frac{\mu_{ff}\,\alpha}{(G_m+\beta_{ff})\,(G_{ff}+1)} \leq M_{vir} \tag{7.4}$$

$$\frac{J_m}{G_{ff}+1} + \frac{\mu_{ff}\,\omega_f}{(G_m+\beta_{ff})\,(G_{ff}+1)} \leq M_{vir} \tag{7.5}$$

Eqn. (7.4) imposes a smaller lower condition on M_{vir} compared to Eqn. (7.5). Thus, it is not possible to passively render mass according to Eqn. (7.4). Notice that the more conservative condition appears as opposed to the other one due to the modelled cut-off frequency of the causal differentiator. Hence, it is not possible to capture this effect when non-causal controllers are used to compensate for Pure Mass Rendering with SEA under BAC.

However, as the equation shows, for large values of G_{ff}, the rendered mass at the end-effector is allowed to be lower than J_m, as opposed to Eqn. (4.4) in Pure Mass Rendering with a P Motion Controller. To achieve a smaller lower bound on M_{vir} than J_m, G_{ff} should satisfy Eqn. (7.6):

$$\frac{\mu_{ff}\,\omega_f}{J_m\,(G_m+\beta_{ff})} \leq G_{ff} \tag{7.6}$$

The equation also shows that when the causal differentiator cut-off frequency is large, the feedforward cancellation term should be increased as well. Since we have shown that mass and damping compensation terms do not help to compensate for the mass, we solely examine the effects of the feedforward force cancellation term G_{ff} when bandwidth limitation is imposed in the following section.

7.2 Feed-Forward Force Cancellation under Bandwidth Limitations

Now, we set $C_{ff} = 0$ and examine the effects of G_{ff} when it is band-limited. Equation (7.7) defines the band-limited version of G_{ff}:

$$G_{ff}^{lpf} = G_{ff} \frac{\omega_f}{s + \omega_f} \tag{7.7}$$

Impedance transfer function seen from the end-effector now becomes $Z_{force-ff}^{P}(s) =$

$$\frac{J_m K_f M_{ref} s^3 + K_f M_{ref} (\alpha + J_m \omega_f) s^2 + K_f M_{ref} \alpha \omega_f s}{J_m M_{ref} s^4 + M_{ref} (\alpha + J_m \omega_f) s^3 + M_{ref} (K_f + \alpha \omega_f) s^2 + n_8 s + G_m K_f \omega_f} \tag{7.8}$$

where $n_8 = K_f (G_m + M_{ref} \omega_f (G_{ff} + 1))$.

Rendered mass, M_{vir}, becomes Eqn. (7.9).

$$M_{vir} = \frac{M_{ref} \alpha}{G_m} \tag{7.9}$$

As in the previous section, we derive necessary and sufficient conditions for the system defined in Equation (7.8) according to Theorem 3.1. The second condition of passivity imposes the following conditions on the rendered mass, M_{vir}:

$$\frac{J_m}{G_{ff} + 1} \leq M_{vir} \tag{7.10}$$

$$J_m \alpha \leq M_{vir} (\alpha - G_{ff} J_m \omega_f) \tag{7.11}$$

$$\alpha - G_{ff} J_m \omega_f \lesseqgtr 0 \tag{7.12}$$

First, we examine the second condition given in Equation (7.11). There are two possible cases based on the factor of M_{vir} in the Eqn. (7.12). Let the factor in Eqn. (7.12) be positive; then Eqn. (7.11) can be rewritten as follows:

$$\frac{J_m \alpha}{\alpha - G_{ff} J_m \omega_f} \leq M_{\text{vir}} \tag{7.13}$$

The lower bound derived in Eqn. (7.13) presents a more conservative bound than Eqn. 7.10 and it is higher than J_m. Thus, in this case, mass compensation with G_{ff} is not possible. The other case, when the factor is negative and the bound in Eqn. (7.11) becomes a higher bound as given in Eqn. (7.14).

$$\frac{J_m \alpha}{\alpha - G_{ff} J_m \omega_f} \geq M_{\text{vir}} \tag{7.14}$$

Note that now the term given in Eqn. (7.12) is negative for the sake of analysis and due to this, the higher bound of M_{vir} is negative. However, negative mass rendering is not possible since there is no such thing as negative mass. Hence, our analysis concludes that when G_{ff} is modeled with bandwidth limitations, it is not possible to compensate for the system inertia.

Several studies have demonstrated that non-causal implementations of feed-forward controllers can effectively achieve inertia compensation [24, 38]. However, our analysis extends these findings by incorporating considerations of causality and bandwidth limitations into the controller. Our study reveals that, with the realistic constraints of causality and bandwidth limitations, passive compensation for inertia while rendering pure mass is unattainable.

Chapter 8

Guidelines for High-Fidelity Haptic Rendering

8.1 Combinations of Virtual Elements

In this section, we discuss our results in terms of combinations of virtual elements to achieve better performance while preserving passivity.

Mass Rendering:

- **Mass-Damping:** The introduction of virtual damping to the mass enables the implementation of a PI controller, in contrast to Pure Mass Rendering where a PI motion controller is unsuitable for passive rendering of pure mass. This change results in improved lower-frequency behavior of the system. Furthermore, the analysis of Pure Mass Rendering has revealed that the minimum renderable mass is constrained by J_m. With the addition of virtual damping, mass compensation becomes feasible. As discussed in Section 4.4, introducing more damping to the system compensates for additional mass, albeit at the cost of increased system damping and greater energy dissipation. Additionally, an increase in added damping imposes limits on mass rendering fidelity.

- **Mass-Spring:** This study does not present Mass-Spring rendering. It is important to note that rendering Mass-Spring (in parallel) passively with SEA under BAC is not achievable.

Damping Rendering:

- **Mass-Damping:** Introducing virtual mass to damping does not alter the rendered damping, B_{vir}. The damping behavior of the system is felt primarily at low frequencies, transitioning to mass during the midband before converging to the high-frequency dynamics inherent in the physical properties of the system, namely SEA. It's crucial to note that even with the minimum mass added to the system, it establishes a more conservative bound on I_m compared to pure damping rendering, as illustrated in Equation (4.25). From this perspective, we can similarly assert that damping compensation is constrained by the addition of mass, compared to the bound in Equation (4.22), since the same equation provides a lower bound on B_{vir}.
- **Voigt-model:** Another option is to introduce a virtual spring to pure damping, as outlined in Section 4.6. This modification shifts the system's low-frequency behavior to that of a spring, transitioning to damping in the midband before converging to SEA at high frequencies. This alteration may lead to unwanted oscillations due to the spring-like behavior, necessitating high damping rendering for compensation. Additionally, controlling the rendered damping becomes challenging due to additional terms in B_{vir} (Equation (4.43)) originating from controllers that act like springs, such as I_m and K_{ref}. One advantage of having a virtual spring is the relaxed passivity condition on I_m, resulting in improved low-frequency behavior. However, achieving this requires higher K_{ref} values, resulting in stiffer rendered springs. While a stiff spring is rendered with the Voigt-model, it restricts rendering high values of B_{vir}, as depicted in Figure 4.9. On the other hand, rendering low

amounts of damping (i.e., damping compensation) necessitates rendering stiff springs, limiting the damping rendering fidelity of the system. Therefore, if the goal is to render lower ranges of damping, one should prefer Pure Damping Rendering. Similarly, if higher ranges of damping are desired Voigt-model is a better option with improved performance.

Spring Rendering:

– **Voigt-model:** Finally, let's consider the addition of virtual damping to pure spring rendering. When we compare the passivity conditions with Pure Spring, we observe that both I_m and K_{ref} are now bounded due to this modification as in Eqn. (4.44). Specifically, I_m limits the rendering of stiff springs, while K_{ref} restricts the rendering of soft springs, each having an upper and lower bound, respectively (note that these bounds do not apply in pure spring rendering). Additionally, the fidelity of rendering soft springs is constrained by the introduction of virtual damping because it necessitates a higher amount of damping to maintain passivity, thus limiting the fidelity of spring rendering. The Voigt-model effectively compensates for unwanted oscillations arising from rendered compliance. Therefore, introducing a slight amount of virtual damping is beneficial when rendering stiff springs. Conversely, Pure Spring Rendering is preferred when the desired stiffness is low, as the addition of high amounts of virtual damping limits the fidelity of spring rendering to preserve passivity.

8.2 Force Sensor Stiffness

In this section, we consider the SEA as a model of a force sensor instrumented at the end-effector, with K_f denoting the sensor stiffness. We explore how sensor compliance influences the passivity and performance of the system under different haptic rendering environments. Stability conditions under passivity analysis for pure elements indicate that sensor compliance relaxes stability. However, positive realness conditions are more conservative and remain unchanged due to SEA. Thus, we conclude that sensor compliance relaxes stability conditions without affecting passivity. Furthermore, the force sensor functions as a mechanical low-pass filter at the end-effector. The stiffness of the sensor directly influences the filtering capabilities of the spring. It is advisable to opt for softer force sensors to ensure a robust interaction in the presence of high-frequency noise.

Mass Rendering: The force sensor model allows us to examine its effects on haptic rendering fidelity. As depicted in Fig. 4.1, it significantly limits the bandwidth when softer sensors are preferred. Rendering mass with compliant sensors is not reasonable. To achieve the best performance in terms of fidelity, one should instrument the system with stiff springs, i.e., traditional force sensors.

Damping Rendering: Softer force sensors increase the stable region for Pure Damping Rendering. However, softer sensors inherently limit the bandwidth of the system due to the addition of compliance at the end-effector. In terms of damping rendering fidelity, it is not directly limited by sensor stiffness, K_f, introducing design challenges to the physical system.

Mass-Damping Rendering: In addition to the two previous discussions, one significant advantage of a softer force sensor is to allow more compensation of mass with the same amount of added virtual damping. As seen in M_{vir}, Eqn. (4.29), as $K_f \rightarrow 0$, the compensation due to B_{ref} increases. However, as the sensor gets softer, it limits the bandwidth, as discussed in the Mass Rendering section.

Spring Rendering: The force sensor appears in series with virtual springs in K_{vir} as seen in the realization Table 4.2f and limits the passively renderable region. Even though there is no upper bound on rendered stiffness according to passivity, the series of springs limits $K_{vir} = K_f$ even with the stiffest controllers. To achieve stiff environments in Spring Rendering, it is crucial to have a stiff force sensor, albeit at the cost of added damping due to sensor stiffness. As shown in effective impedance analysis, Pure Spring Rendering has damping felt at the end-effector, which is proportional to sensor stiffness. The trade-off between a damped system due to a stiff force sensor allows users to render stiff environments.

Voigt-model Rendering: Similar to spring rendering, force sensor compliance adds damping to Voigt-model Rendering, appearing in B_{vir} as seen in Eqn. (4.43). On the other hand, softer sensors allow us to render lower levels of damping compared to Pure Damping rendering, since $K_f \to 0$ makes $B_{vir} \to 0$ as well. To compensate for the system's damping while rendering Voigt-model, one should instrument the system with a compliant force sensor. However, the system will be subjected to bandwidth limitations and unwanted oscillations due to compliance at the end-effector.

8.3 Impedance versus Admittance Control

Implementing non-causal controllers in real-time applications poses feasibility challenges. To maintain causality, it is essential to employ filters or causal versions of differentiators during the implementation process. However, the incorporation of filters introduces time delays to the system, subsequently compromising the quality of interaction with human users. Additionally, depending on the controller type, be it admittance or impedance, certain virtual environments necessitate the use of filters to preserve causality.

In the context of spring rendering with admittance control, achieving causality becomes complex since the desired admittance is expressed as $A_d = \frac{s}{K_{ref}}$. Filtering the desired admittance for causality transforms it into a Voigt model, as depicted in Eqn. (4.38). Consequently, achieving pure spring rendering under admittance control with causal controllers becomes unattainable based on this analysis.

Similarly, mass rendering with impedance control demands a causal differentiator, given that the desired impedance is expressed as $Z_d = M_{ref}, s$. Furthermore, in impedance-based approaches, the velocity signal at the end-effector needs to be measured. Even in cases where it is not explicitly modeled, this measurement introduces a filter to the system, further complicating the implementation.

First, we can directly say that the need of a filter in impedance control for mass rendering (causality) and damping rendering (filter to measure velocity of the end-effector) degrades performance compared to admittance control. Moreover, these constraints impose upper-bounds on passively renderable M_{vir} and B_{vir} which do not apply to admittance control. Thus, it is beneficial to use admittance control to render high impedances.

On the other hand, pure spring rendering is not possible due to causality issues in admittance control. And, it converges to Voigt-model as a filter modeled in the analysis. Thus, it makes impedance control a more preferable choice for spring rendering.

Lastly, null-space rendering requires $Z_d = 0$ and $A_d = \infty$. Hence, it is not feasible to render null space with an admittance control in real-time applications.

Overall, admittance control is recommended for high impedances while impedance control is better suited for low impedances.

8.4 Generalization to Other Controller Architectures

In our study, we analyzed the admittance control structure with SEA. However, our results not only establish the capabilities and limitations of SEA under admittance control but also cover regular admittance-controlled devices when the force sensor stiffness is high.

It is important to note that as the force sensor stiffness increases, the validity of the rigid robot model diminishes since non-collocation effects will be observed. As Eppinger [29] has shown, unmodeled dynamics between the actuator and the sensor introduce challenges to preserving the stability of the system under force control. Moreover, this non-collocation imposes limits on force controller gains, in our case, on the reference admittances. This limitation can be discussed for all the haptic rendering analyzed in Chapter 4. As reference admittances are force controller gains in our analyzed system, all the reference admittances will now have upper limits. Since reference admittances are mapped directly to desired admittances, namely Z_{vir} as derived in Chapter 4, will also be limited.

Firstly, it is important to note that mass rendering is constrained by a minimum value for M_{ref}, dictated by the passivity considerations, whether in the case of pure mass rendering or when combined with virtual damping. Conversely, there is not an upper limit imposed on the reference admittance theoretically (under the assumption of collocated control), allowing for the rendering of high impedances by scaling up the reference to achieve the desired admittance. However, if the model features non-collocation, M_{ref} will have an upper limit as Eppinger [29] discusses. This constraint will limit passively renderable M_{width} as M_{ref} is directly mapped to M_{vir} as in Eqn. (4.4), (4.13) and (4.29). Same discussion applies to B_{ref} and B_{vir}.

Stiffness rendering presents a different scenario compared to mass and damping rendering. Even if K_{ref} does not have an upper limit, K_{vir} has an upper limit

imposed by the softest spring in the system due to its inherent structure given in Eqn. (4.37). We do not see such a limitation for M_{vir} and/or B_{vir}.

Non-collocation introduces a limitation on K_{ref} by imposing an upper bound due to the internal compliance of the robot, influencing both the rendered stiffness and the passivity bounds on the controller gains. This limitation is not observed in our analysis, since SEA introduces high compliance that dominates the first vibration mode of the system.

TABLE 8.1: Admittance Control and VSIC Mapping

VSIC (Null)	**Admittance Control Equivalent**	**Parameter Mapping**
P_t - P_m I_m	Pure Damping - P_m I_m	$P_t \rightarrow \frac{1}{B_{ref}}$
I_t - P_m I_m	Pure Mass - P_m I_m	$I_t \rightarrow \frac{1}{M_{ref}}$
D_t - P_m I_m	Pure Spring - P_m I_m	$D_t \rightarrow \frac{1}{K_{ref}}$

Admittance-controlled SEA is a special case of SEA under VSIC. Free space rendering with SEA under VSIC has the identical structure with the controller presented in Fig. 3.2. While the inner motion loop acts exactly same in the both structures, it is important to note the parameter mapping between these two is as in Table 8.1. In this table, the first column illustrates the controller structure of VSIC force controller and motion controller, respectively, while the second column corresponds to the haptic rendering with the admittance controller. Notably, the force/torque controller of VSIC shapes the virtual environment that is rendered in admittance control. Consequently, our study holds significant implications for the analysis of SEA under VSIC.

Chapter 9

Conclusion

We have presented a comprehensive analysis of the stability robustness and trade-offs in haptic rendering fidelity of Series Elastic Actuation (SEAs) under Basic Admittance Controller (BAC). Our results involves other kinesthetic haptic interfaces operating under admittance control, particularly as a special case when the sensor stiffness is set to high. We derived necessary and sufficient conditions for SEA passivity when rendering various virtual environments, analyzing the haptic rendering performance of closed-loop systems through passive physical equivalents and effective impedance analysis. Our study presents parasitic effects, examines low-high frequency behaviors, and compares the rendering performance of different closed-loop systems using passive physical equivalents, building upon existing literature [19, 25, 30, 32].

Our findings highlight that reducing force sensor stiffness increases stability robustness in haptic rendering. However, passivity is not compromised by this adjustment. Softer force sensors enhance inertia compensation but limit bandwidth during mass rendering. Conversely, stiff force sensors relax the upper bound on rendered stiffness while introducing parasitic damping. We demonstrate the feasibility of damping compensation with SEA under BAC, even without a negative reference and with a lower bound on rendered damping due to passivity constraints. Introducing a virtual spring to pure damping (Voigt-model) relaxes passivity conditions on controller gains while enhancing performance, though it

constrains passively renderable damping. Similarly, the Voigt-model provides a more accurate representation while rendering stiffness with BAC, as pure spring rendering is unattainable. Combining an appropriate amount of virtual damping with inertia allows better inertia compensation while limiting mass rendering bandwidth.

In passivity analysis, we emphasize that the controlled plant time constant imposes constraints on passivity, highlighting the importance of precise control for optimal performance and a larger passivity region.

Lastly, we demonstrate that achieving passive inertia compensation via feedforward controller terms is impractical under realistic bandwidth limitations. However, these terms can enhance rendering performance at low frequencies.

Our theoretical findings are rigorously validated through systematic simulations and experiments, confirming passivity bounds through coupled stability experiments in relevant destabilizing environments. Rendering performance is characterized by exciting closed-loop systems with an ideal motion source.

In summary, our study provides a thorough analysis of stability robustness and rendering fidelity trade-offs in kinesthetic haptic interfaces, particularly under admittance control, including SEA. Furthermore, our results have broader implications for more complex control approaches, such as VSIC, as admittance control forms a fundamental component in such architectures. Our guidelines offer valuable insights for researchers aiming to implement passive virtual environment renderings with high fidelity, design advanced haptic interfaces for admittance control, and gain a deeper understanding of the limitations of their interaction controllers.

For future studies, the non-collocation and transmission ratio between the actuator and the end-effector can be modeled to examine their effects on both passivity and haptic rendering performance. Moreover, we ignore the bandwidth limitations that we have on controllers and actuators. These non-modeled dynamics might have significant effects on both passivity and haptic rendering performance of admittance controlled devices.

Bibliography

[1] J. E. Colgate, *The control of dynamically interacting systems.* PhD thesis, Massachusetts Institute of Technology, 1988.

[2] W. S. Newman, "Stability and Performance Limits of Interaction Controllers," *Journal of Dynamic Systems, Measurement, and Control*, vol. 114, pp. 563–570, 12 1992.

[3] R. Unal, G. Kiziltas, and V. Patoglu, "A multi-criteria design optimization framework for haptic interfaces," pp. 231 – 238, 04 2008.

[4] S. D. Eppinger and W. P. Seering, "Understanding bandwidth limitations in robot force control," *Proceedings. 1987 IEEE International Conference on Robotics and Automation*, vol. 4, pp. 904–909, 1987.

[5] R. D. Howard, *Joint and actuator design for enhanced stability in robotic force control.* PhD thesis, MIT, 1990.

[6] G. A. Pratt and M. M. Williamson, "Series elastic actuators," in *IEEE Int. Conf. on Intelligent Robots and Systems*, vol. 1, pp. 399–406, 1995.

[7] N. Hogan, "Impedance control: An approach to manipulation: Part ii—implementation," *Journal of Dynamic Systems Measurement and Control-transactions of The Asme*, vol. 107, pp. 8–16, 1985.

[8] D. E. Whitney, "Force Feedback Control of Manipulator Fine Motions," *Journal of Dynamic Systems, Measurement, and Control*, vol. 99, pp. 91–97, 06 1977.

[9] R. Adams and B. Hannaford, "Stable haptic interaction with virtual environments," *IEEE Transactions on Robotics and Automation*, vol. 15, no. 3, pp. 465–474, 1999.

[10] V. Q, P. Lammertse, E. Frederiksen, and B. Ruiter, "The hapticmaster, a new high-performance haptic interface," 07 2002.

[11] E. Faulring, J. Colgate, and M. Peshkin, "A high performance 6-dof haptic cobot," vol. 2, pp. 1980–1985, 01 2004.

[12] J. E. Colgate and N. Hogan, "Robust control of dynamically interacting systems," *International Journal of Control*, vol. 48, no. 1, pp. 65—-88, 1988.

[13] S. Haykin, *Active network theory*. Addison-Wesley Pub. Co., 1970.

[14] F. F. Kuo, *Network Analysis and Synthesis*. John Wiley & Sons, 1962.

[15] E. Colgate and N. Hogan, "An analysis of contact instability in terms of passive physical equivalents," *Proceedings, 1989 International Conference on Robotics and Automation*, pp. 404–409 vol.1, 1989.

[16] N. Colonnese, A. F. Siu, C. M. Abbott, and A. M. Okamura, "Rendered and characterized closed-loop accuracy of impedance-type haptic displays," *IEEE Transactions on Haptics*, vol. 8, no. 4, pp. 434–446, 2015.

[17] J. S. Hart and G. Niemeyer, "Absolutely stable model-based 2-port force controller for telerobotic applications," *The International Journal of Robotics Research*, vol. 33, no. 6, pp. 847–865, 2014.

[18] J. M. Schimmels and M. A. Peshkin, "The robustness of an admittance control law designed for force guided assembly to the disturbance of contact friction," in *Proceedings 1992 IEEE International Conference on Robotics and Automation*, pp. 2361–2362, IEEE Computer Society, 1992.

[19] M. Dohring and W. Newman, "The passivity of natural admittance control implementations," in *2003 IEEE International Conference on Robotics and Automation (Cat. No. 03CH37422)*, vol. 3, pp. 3710–3715, IEEE, 2003.

[20] M. Ueberle, "Control of kinesthetic haptic interfaces," in *IROS, Proc of the IEEE/RSJ Int Conf on, Workshop on Touch and Haptics: 2004*, 2004.

[21] R. J. Adams and B. Hannaford, "Control law design for haptic interfaces to virtual reality," *IEEE Transactions on control systems technology*, vol. 10, no. 1, pp. 3–13, 2002.

[22] A. Fortin-Côté, P. Cardou, and C. Gosselin, "An admittance control scheme for haptic interfaces based on cable-driven parallel mechanisms," in *2014 IEEE International Conference on Robotics and Automation (ICRA)*, pp. 819–825, IEEE, 2014.

[23] H. Wang, F. Patota, G. Buondonno, M. Haendl, A. De Luca, and K. Kosuge, "Stability and variable admittance control in the physical interaction with a mobile robot," *International Journal of Advanced Robotic Systems*, vol. 12, no. 12, p. 173, 2015.

[24] A. Q. Keemink, H. van der Kooij, and A. H. Stienen, "Admittance control for physical human–robot interaction," *The International Journal of Robotics Research*, vol. 37, no. 11, pp. 1421–1444, 2018.

[25] A. Calanca, R. Muradore, and P. Fiorini, "Impedance control of series elastic actuators: Passivity and acceleration-based control," *Mechatronics*, vol. 47, pp. 37–48, 2017.

[26] T. Horibe, E. Treadway, and R. B. Gillespie, "Comparing series elasticity and admittance control for haptic rendering," in *Haptics: Perception, Devices, Control, and Applications - 10th International Conference, EuroHaptics 2016, London, UK, July 4-7, 2016, Proceedings, Part I* (F. Bello, H. Kajimoto, and Y. Visell, eds.), vol. 9774 of *Lecture Notes in Computer Science*, pp. 240–250, Springer, 2016.

[27] D. A. Lawrence, "Impedance control stability properties in common implementations," *Proceedings. 1988 IEEE International Conference on Robotics and Automation*, pp. 1185–1190 vol.2, 1988.

[28] A. Calanca, R. Muradore, and P. Fiorini, "A review of algorithms for compliant control of stiff and fixed-compliance robots," *IEEE/ASME Transactions on Mechatronics*, vol. 21, no. 2, pp. 613–624, 2016.

[29] S. Eppinger and W. Seering, "On dynamic models of robot force control," in *Proceedings. 1986 IEEE International Conference on Robotics and Automation*, vol. 3, pp. 29–34, 1986.

[30] F. Tosun and V. Patoglu, "Necessary and sufficient conditions for the passivity of impedance rendering with velocity-sourced series elastic actuation," *IEEE Transactions on Robotics*, vol. PP, pp. 1–16, 01 2020.

[31] O. T. Kenanoglu, C. U. Kenanoglu, and V. Patoglu, "Effect of low-pass filtering on passivity and rendering performance of series elastic actuation," *IEEE Transactions on Haptics*, 2023.

[32] C. Kenanoglu and V. Patoglu, "Passive realizations of series elastic actuation: Passivity and effects of plant and controller dynamics on haptic rendering performance," 09 2022.

[33] M. C. Smith, "Synthesis of mechanical networks: the inerter," *IEEE Transactions on automatic control*, vol. 47, no. 10, pp. 1648–1662, 2002.

[34] M. Z. Chen, C. Papageorgiou, F. Scheibe, F.-C. Wang, and M. C. Smith, "The missing mechanical circuit element," *IEEE Circuits and Systems Magazine*, vol. 9, no. 1, pp. 10–26, 2009.

[35] R. M. Foster, "A reactance theorem," *Bell System technical journal*, vol. 3, no. 2, pp. 259–267, 1924.

[36] O. Brune, *Synthesis of a finite two-terminal network whose driving-point impedance is a prescribed function of frequency.* PhD thesis, Massachusetts Institute of Technology, 1931.

[37] U. Caliskan, A. Apaydin, A. Otaran, and V. Patoglu, "A series elastic brake pedal to preserve conventional pedal feel under regenerative braking,"

2018 IEEE/RSJ International Conference on Intelligent Robots and Systems (IROS), pp. 1367–1373, 2018.

[38] D. Ko, D. Lee, W. K. Chung, and K. Kim, "On the performance and passivity of admittance control with feed-forward input," in *2022 IEEE/RSJ International Conference on Intelligent Robots and Systems (IROS)*, pp. 11209–11215, 2022.